The Chemistry of Copernicium: Superheavy Element and Homolog Studies

Inauguraldissertation der Philosophisch-naturwissenschaftlichen Fakultät der Universität Bern

vorgelegt von

Paul Ionescu

aus Berlin, Deutschland

Leiter der Arbeit:

Prof. Dr. Andreas Türler

Department für Chemie und Biochemie (Universität Bern)

Co-Leiter der Arbeit:

Dr. Robert Eichler

Labor für Radiochemie (Paul Scherrer Institut)

The Chemistry of Copernicium: Superheavy Element and Homolog Studies

Inauguraldissertation der Philosophisch-naturwissenschaftlichen Fakultät der Universität Bern

vorgelegt von

Paul Ionescu

aus Berlin, Deutschland

Leiter der Arbeit:

Prof. Dr. Andreas Türler

Department für Chemie und Biochemie (Universität Bern)

Co-Leiter der Arbeit:

Dr. Robert Eichler

Labor für Radiochemie (Paul Scherrer Institut)

Von der Philosophisch-naturwissenschaftlichen Fakultät angenommen.

Bern, 25.10.2021

Der Dekan,

Prof. Dr. Zoltan Balogh

CC BY-NC-ND 4.0 DEED

Attribution-NonCommercial-NoDerivs 4.0 International

You are free to:

Share — copy and redistribute the material in any medium or format

The licensor cannot revoke these freedoms as long as you follow the license terms.

Under the following terms:

Attribution - You must give appropriate credit , provide a link to the license, and indicate if changes were made . You may do so in any reasonable manner, but not in any way that suggests the licensor endorses you or your use.

NonCommercial - You may not use the material for commercial purposes .

NoDerivatives - If you remix, transform, or build upon the material, you may not distribute the modified material.

No additional restrictions - You may not apply legal terms or technological measures that legally restrict others from doing anything the license permits.

Notices:

You do not have to comply with the license for elements of the material in the public domain or where your use is permitted by an applicable exception or limitation .

No warranties are given. The license may not give you all of the permissions necessary for your intended use. For example, other rights such as publicity, privacy, or moral rights may limit how you use the material.

«Halt, Stopp, Stopp! Das Messsystem brennt!»
-R. Dressler, Dubna 2018

Glossary

AFM Atomic Force Microscopy. 78, 86

CN Compound Nucleus. 13, 16–19, 21, 23

COLD Cryo On-Line Detector. 29, 35, 43, 45, 51, 110, 112, 113, 115–119, 121, 122, 126, 127, 129, 130, 133, 134, 147, 151

ER Evaporation Residues. 17–20, 22, 28, 29, 35, 38, 141, 142

FLNR Flerov Laboratory of Nuclear Reactions. 113, 133

GC Gas Chromatography. 35, 38, 42, 44, 49, 51, 76, 79, 80, 93, 100, 104, 106, 116, 119, 121, 139–141, 145, 146, 148, 150, 151

GSI Gesellschaft für Schwerionenforschung. 28–30

IT Isothermal Chromatography. 38

IUPAC International Union of Pure and Applied Chemistry. 8, 9

IUPAP International Union of Pure and Applied Physics. 9

IVO In-situ Volatilization Oven. 113

JAEA Japanese Atomic Energy Agency. 144

LDM Liquid Drop Model. 11–13

MCS Monte-Carlo Simulation. 40, 42–44, 46–48, 51, 72, 78–80, 84, 86, 94, 97, 98, 101, 103, 104, 111, 116–118, 125–130

PICVD Photo-Induced Chemical Vapor Deposition. 71, 74, 85, 86

PIN Positive Implanted N-type. 26, 28, 45, 51, 71, 78, 113–119, 122, 123, 133, 134, 142

PVD Physical Vapor Deposition. 71, 75–79, 82, 86, 99

SEM Scanning Electron Microscopy. 81

SF Spontaneous Fission. 11, 13, 17, 24–28, 114, 115, 123, 124

SHE Superheavy Element. 8, 10, 13, 15, 17, 19, 20, 22, 24, 27, 28, 30, 37, 38, 40, 43, 44, 47, 87, 93, 110, 111, 122, 123, 125, 133, 139, 141, 144, 150, 151

SHEs Superheavy Elements. 7, 9, 10, 13, 26, 30, 38, 93, 105, 110, 122, 133, 139, 141, 151

SINQ Swiss Spallation Neutron Source. 98

STP Standard Temperature and Pressure. 94

TC Thermochromatography. 38, 39, 44, 48, 93, 94, 97, 99, 100, 103, 110–112

TRACY Trace-gas Reaction Analyzer for Chemistry. 134, 141, 145–147, 150, 151

XRD X-Ray Diffraction. 82, 86

Summary

In this work, chemical experiments on mercury are described which serve as a foundation for the ongoing research on the transactinide copernicium (Cn, element 112). A first indication of a Cn reaction is reported. The reactivity is higher than expected, as Cn until now has been shown to behave as an inert element resembling a noble gas.

The Periodic Table serves chemists as a fundamental reference tool, providing an accessible framework that reveals information about the elements. Even the chemical behaviour of unfamiliar elements can be deduced and approximated well from the periodicity of elements in a common group due to the same number of valence electrons. On this basis, the chemistry of Cn as a member of group 12 is related to its homolog Hg. However, the relativistic effects on electron structure increase with the nuclear charge and it follows that the chemistry of Cn is more affected by relativity than that of its lighter homologs. Predictions, as well as the first series of chemical experiments on Cn both pointed towards an increasingly inert nature of the transactinide largely owing to the influence of relativistic effects and therefore deviating from its homologs. The experimental method of gas chromatography is central to the investigation of short-lived transactinides and used extensively throughout this work. A second generation gas chromatographic experiment was designed to investigate the reactivity of Cn towards the chalcogen Se in comparison to Hg, but preliminary results were inconclusive. This work continues by building on the preliminary findings.

First, a uniform and stable trigonal selenium stationary phase was developed for use in chromatography. As a chalcogen, Se forms a number of allotropes. Some of these allotropes are unstable and change properties over time. To ensure long-term stability, the thermodynamically most stable state at standard temperature and pressure was chosen, the trigonal allotrope of selenium, *t*-Se. An additional condition for the chromatographic *t*-Se surface was producing a uniform, thin film, as the Se covered α-particle and spontaneous fission fragment detectors. A thinner, uniform film minimizes interference with the energy resolution of the spectrometry. Multiple methods for the production of such *t*-Se films were explored and have been

characterized and assessed for the feasibility in use for transactinide gas chromatographic investigation. A novel selenium casting method, photo-induced chemical vapour deposition and physical vapour deposition were the techniques explored here. Allotropy of the Se films and the conversion to the stable *t*-Se form is documented. For the purpose of α- and spontaneous fission detector manufacturing, physical vapour deposition was ultimately chosen. Isothermal gas chromatography with carrier-free $^{197m,\ 203}$Hg radioisotopes was used to evaluate the long-term stability and degree of conversion of various selenium surfaces. It was discovered that despite complete conversion to the *t*-Se allotrope, reactive sites in the Se were present. It was found that due to crystallization, approximately 1% of the selenium atoms on the surface are monovalent and provide sites with increased reactivity for the Hg tracer. These findings are to be submitted for publication to Thin Solid Films.

A first use of the technique of inverse thermochromatography is presented here, where the stable *t*-Se stationary phase was placed in a chromatographic column with positive temperature gradient to increase the reaction rate for the carrier-free $^{197m,\ 203}$Hg tracer gradually. The Eyring-Polanyi equation was used in a microscopic Monte-Carlo simulation to describe the forward reaction rate of the HgSe formation, and a first report of the Gibbs free energy of activation was obtained at $\Delta G^{\ddagger}(\mathrm{HgSe}) = 95 \pm 12$ kJ/mol. Additionally, using the Arrhenius equation, a first report of the activation energy for the HgSe formation of $E_a(\mathrm{HgSe}) = 100 \pm 10$ kJ/mol with pre-exponential factor of $A = 4.3 \cdot 10^{13} \pm 2.6 \cdot 10^{13}$ was made. The activation energy of group 12 elements was used to make an extrapolation to the value of Cn, which was predicted at $E_a(\mathrm{CnSe}) = 106 \pm 22$ kJ/mol, higher than all of the group 12 metals, and therefore supporting the postulate that Cn is more inert than its lighter homologs. The novel method of inverse chromatography and the thermochemical data is to be submitted for publication to the Journal of Radioanalytical and Nuclear Chemistry.

The discoveries made based on the reactivity of Hg toward *t*-Se and the optimized *t*-Se chromatographic surface culminated in a new experimental campaign in 2018 at Flerov Laboratory for Nuclear Reactions in Dubna, Russian Federation, with the transactinide Cn to expand on earlier preliminary findings. Contrary to expectation, it became evident from the 8 atoms

observed that the superheavy element Cn shows much greater affinity toward *t*-Se than anticipated. The adsorption enthalpy was determined to be -ΔH_{ads}^{t-Se}(Cn) = 62 ±5 kJ/mol, greater than that of Hg at -ΔH_{ads}^{t-Se}(Hg) = 60 kJ/mol. Such a strong value points toward chemisorption, where the Cn atom not only adsorbs to the *t*-Se surface, but forms a chemical bond. Given the experimental results, an upper limit of the activation energy of E_a(CnSe) < 90 kJ/mol was deduced, significantly lower than that of Hg at E_a(HgSe) = 100 ± 10 kJ/mol. As a result the surprising conclusion was reached that Cn exhibits increased reactivity toward *t*-Se than its lighter homolog Hg. Therefore a reversal of the established adsorption trend on gold of -ΔH_{ads}^{Au}(Hg) > -ΔH_{ads}^{Au}(Cn) > -ΔH_{ads}^{Au}(Rn) is presented here, with -ΔH_{ads}^{t-Se}(Cn) > -ΔH_{ads}^{t-Se}(Hg) > -ΔH_{ads}^{t-Se}(Rn). These findings contradict the previous assumptions that Cn resembles a noble gas and suggest a first observed reaction of the transactinide.

The ambient conditions of the gas chromatographic investigation of Cn were closely monitored and two contaminations interfering with experimental results were identified. One was attributed to the presence of oxygen in the system when Ta getters were operating below temperatures of 900°C. The oxygen presence was shown to influence the radionuclide transport yield of Hg by a factor of 3. Additionally, an unknown contamination was observed to interfere with Au-covered detectors in the array as temperatures decreased below room temperature level. Se detectors were unaffected. The most likely source was identified to be left-over organic materials from the plutonium oxide target production evaporating during irradiation of the target.

To investigate the effects of contaminant gases such as the yield fluctuation by the presence of oxygen in the gas chromatography, a new experiment was designed, built and calibrated with the possibility of purposely functionalizing the chromatographic carrier gas. The Trace-gas Reaction Analyzer for Chemistry (TRACY) is a compact modular gas chromatography easily adapted for a variety of experiments both on- and off-line.

Contents

1 Introduction

1.1 A Brief History on the Periodic Table

The periodic table is the culmination of man's combined knowledge of the elements. 118 elements have been discovered up to date and still the search for more continues [1]. This work deals with the heaviest elements at the most extreme limits of stability. Before venturing to these outermost extremes, a history of the fundamentals will be considered. Dmitri Mendeleev is commonly thought of as the father of the modern periodic table having arranged elements according to their atomic mass while considering analogous chemical properties [2]. A structured compilation of elements had been attempted multiple times earlier, including Newland's 1865 $law\ of\ octaves$, or Lothar Meyer's work, who as Mendeleev's rival created his own periodic system based on chemical and physical properties increasing with atomic weights [3, 4]. The most notable feature of Mendeleev's table was the incorporation of gaps at atomic masses where no suitable candidate was yet known. Mendeleev used this most notably to predict the properties of elements that had not been discovered at the time (Figure 1).

Tabelle II.

Reihen	Gruppe I. — R^2O	Gruppe II. — RO	Gruppe III. — R^2O^3	Gruppe IV. RH^4 RO^2	Gruppe V. RH^3 R^2O^5	Gruppe VI. RH^2 RO^3	Gruppe VII. RH R^2O^7	Gruppe VIII. — RO^4
1	H=1							
2	Li=7	Be=9,4	B=11	C=12	N=14	O=16	F=19	
3	Na=23	Mg=24	Al=27,3	Si=28	P=31	S=32	Cl=35,5	
4	K=39	Ca=40	—=44	Ti=48	V=51	Cr=52	Mn=55	Fe=56, Co=59, Ni=59, Cu=63.
5	(Cu=63)	Zn=65	—=68	—=72	As=75	Se=78	Br=80	
6	Rb=85	Sr=87	?Yt=88	Zr=90	Nb=94	Mo=96	—=100	Ru=104, Rh=104, Pd=106, Ag=108.
7	(Ag=108)	Cd=112	In=113	Sn=118	Sb=122	Te=125	J=127	
8	Cs=133	Ba=137	?Di=138	?Ce=140	—	—	—	— — — —
9	(—)	—	—	—	—	—	—	
10	—	—	?Er=178	?La=180	Ta=182	W=184	—	Os=195, Ir=197, Pt=198, Au=199.
11	(Au=199)	Hg=200	Tl=204	Pb=207	Bi=208	—	—	
12	—	—	—	Th=231	—	U=240	—	— — — —

der chemischen Elemente. 151

11 *

Figure 1: Mendeleev's 1871periodic table, note the dashes with assigned masses representing postulated elements. The Sanskrit prefix "eka-"[1] naming convention emerged later [5].

Mendeleev's systematic arrangement of the elements helped accurately predict eka-aluminium, eka-boron and eka-silicon[1] with their potential physical properties. These would later be discovered and named gallium, scandium and germanium [5, 6]. The metal gallium for example, discovered only four years later than Mendeleev's prediction by the French chemist Paul Émile Leqoc de Boudain had properties similar to those postulated (Table 1).

The periodic table continued to evolve, but it wasn't until the discovery of the concept of an atomic number Z by Henry Mosley using X-ray spectrometry in 1914 and the discovery of the proton by Ernest Rutherford in 1917 that would provide a more complete view of the atom and a definite method of classifying elements free from the ambiguity stemming from isotopic mass [7–9]. Not only do these advancements provide chemists today with one of their most fundamental tools - they ignited an era of systematic search for the elements in a drive to understand chemistry at a fundamental level. This more structured periodic table thus

[1]The Sanskrit *eka−* (meaning *one−*) prefix is a common naming convention for the next homolog in a group.

Table 1: Comparison between Mendeleev's predicted element eka-aluminium (1871) and shortly later discovered gallium (1875). "Low" melting point refers to a *relatively* low temperature for a metal.

	eka-aluminium	gallium
Molecular Mass (g/mol)	68	69.72
Relative density (kg/cm^3)	5.9	5.94
Melting point (°C)	low	30.15
Metal oxide formation	M_2O_3	Ga_2O_3
Discovery by	Spectroscopy	Spectroscopy

provided a framework to search systematically for unknown elements by atomic number rather than mass. Such an example is the elusive technetium, discovered almost 100 years after its neighbours in the periodic table, in 1937 [10, 11]. There was a certainty that an element with atomic number $Z = 43$ should exist. Despite several erroneous identifications it was finally synthesized in a nuclear reaction, as it was not known that the unstable technetium only exists evanescent in nature [11, 12].

The dawn of the nuclear age saw elements undergo transmutation. Radioactivity was discovered by the French chemist Henri Becquerel in 1896 while working with uranium salts [13, 14]. While it was initially thought that this radioactivity was solely due to X-rays, it became apparent that the observed phenomena involved a much more complicated process.

The development of particle accelerators and the discovery of the neutron for the first time allowed the production of elements heavier than uranium ($Z = 92$)[15–17]. Enrico Fermi first began systematically irradiating samples of elements with neutrons in the 1930's. After observing transmutations, it was considered for the first time that elements with higher Z could be produced when he suggested having isolated element 93 (neptunium) [18]. Fermi however did not make the claim to discovery, and neptunium was discovered conclusively by McMillan and Abelson in 1940 [19, 20]. McMillan entered a collaboration with Glenn T. Seaborg and

together they received the 1951 Nobel Prize in chemistry "for their discoveries in the chemistry of transuranium elements" [21]. Later, Fermi proposed the addition of transuranium elements to the periodic table which led to a further expansion up to the "fermium gap" ($Z = 100$), the known natural limit of heavy element production using slow neutron capture processes [18, 22]. Since no known fermium isotopes undergo β^- decay, no elements with higher Z can be produced by the means of slow neutron capture [22]. All elements with $Z > 100$ so far have been produced in heavy-ion-induced nuclear fusion evaporation reactions and not been found in nature, even though their occurrence has not been ruled out [23–26]. One of the earliest suspected discoveries of heavier elements in nature was done by German scientist Richard von Swinne, who believed to have discovered element 108 using X-ray spectroscopy in Greenlandic ice in 1914, but was unable to verify his observation [27]. However, due to the short half-lives now known, the search for heavy elements is focused on meteorite samples and stars in space, as endemic Earth deposits in the crust from the Hadean eon[2] would have likely decayed [28].

The transactinide elements, also known as Superheavy Elements (SHEs) begin with the end of the actinide series at $Z \geq 104$ (Figure 2).

IUPAC Periodic Table of the Elements

1																	18
1 H hydrogen [1.0078, 1.0082]	2											13	14	15	16	17	2 He helium 4.0026
3 Li lithium 6.94 [6.938, 6.997]	4 Be beryllium 9.0122											5 B boron 10.81 [10.806, 10.821]	6 C carbon 12.011 [12.009, 12.012]	7 N nitrogen 14.007 [14.006, 14.008]	8 O oxygen 15.999 [15.999, 16.000]	9 F fluorine 18.998	10 Ne neon 20.180
11 Na sodium 22.990	12 Mg magnesium 24.306 [24.304, 24.307]	3	4	5	6	7	8	9	10	11	12	13 Al aluminium 26.982	14 Si silicon 28.085 [28.084, 28.086]	15 P phosphorus 30.974	16 S sulfur 32.06 [32.059, 32.076]	17 Cl chlorine 35.45 [35.446, 35.457]	18 Ar argon 39.95 [39.792, 39.963]
19 K potassium 39.098	20 Ca calcium 40.078(4)	21 Sc scandium 44.956	22 Ti titanium 47.867	23 V vanadium 50.942	24 Cr chromium 51.996	25 Mn manganese 54.938	26 Fe iron 55.845(2)	27 Co cobalt 58.933	28 Ni nickel 58.693	29 Cu copper 63.546(3)	30 Zn zinc 65.38(2)	31 Ga gallium 69.723	32 Ge germanium 72.630(8)	33 As arsenic 74.922	34 Se selenium 78.971(8)	35 Br bromine 79.904 [79.901, 79.907]	36 Kr krypton 83.798(2)
37 Rb rubidium 85.468	38 Sr strontium 87.62	39 Y yttrium 88.906	40 Zr zirconium 91.224(2)	41 Nb niobium 92.906	42 Mo molybdenum 95.95	43 Tc technetium	44 Ru ruthenium 101.07(2)	45 Rh rhodium 102.91	46 Pd palladium 106.42	47 Ag silver 107.87	48 Cd cadmium 112.41	49 In indium 114.82	50 Sn tin 118.71	51 Sb antimony 121.76	52 Te tellurium 127.60(3)	53 I iodine 126.90	54 Xe xenon 131.29
55 Cs caesium 132.91	56 Ba barium 137.33	57-71 lanthanoids	72 Hf hafnium 178.49(2)	73 Ta tantalum 180.95	74 W tungsten 183.84	75 Re rhenium 186.21	76 Os osmium 190.23(3)	77 Ir iridium 192.22	78 Pt platinum 195.08	79 Au gold 196.97	80 Hg mercury 200.59	81 Tl thallium 204.38 [204.38, 204.39]	82 Pb lead 207.2	83 Bi bismuth 208.98	84 Po polonium	85 At astatine	86 Rn radon
87 Fr francium	88 Ra radium	89-103 actinoids	104 Rf rutherfordium	105 Db dubnium	106 Sg seaborgium	107 Bh bohrium	108 Hs hassium	109 Mt meitnerium	110 Ds darmstadtium	111 Rg roentgenium	112 Cn copernicium	113 Nh nihonium	114 Fl flerovium	115 Mc moscovium	116 Lv livermorium	117 Ts tennessine	118 Og oganesson

57 La lanthanum 138.91	58 Ce cerium 140.12	59 Pr praseodymium 140.91	60 Nd neodymium 144.24	61 Pm promethium	62 Sm samarium 150.36(2)	63 Eu europium 151.96	64 Gd gadolinium 157.25(3)	65 Tb terbium 158.93	66 Dy dysprosium 162.50	67 Ho holmium 164.93	68 Er erbium 167.26	69 Tm thulium 168.93	70 Yb ytterbium 173.05	71 Lu lutetium 174.97
89 Ac actinium	90 Th thorium 232.04	91 Pa protactinium 231.04	92 U uranium 238.03	93 Np neptunium	94 Pu plutonium	95 Am americium	96 Cm curium	97 Bk berkelium	98 Cf californium	99 Es einsteinium	100 Fm fermium	101 Md mendelevium	102 No nobelium	103 Lr lawrencium

[2]The Hadean eon ended $> 4 \cdot 10^9$ years ago.

Figure 2: The modern periodic table of the elements (2018) with completed 7th row. Adapted version from the International Union of Pure and Applied Chemistry (IUPAC) [29]

The study of SHEs is particularly challenging and rewarding in that current technology is pushed to the extremes in the quest for their research while discovering fundamental properties of highly unstable atoms. The effect of the high nuclear core charge of a SHE on chemical behaviour has long been a point of debate. The periodicity of the periodic table could be perturbed due to uncharacteristic properties of elements within a group emerging [30, 31]. These properties are a direct consequence of the increasing influence of relativistic effects on the electron shells affecting the chemistry. Relativistic effects are known to increase for valence shells with the order of $(\alpha Z)^2$ and can be summarized with three main effects[3] [32–34]:

I. Contraction and stabilisation of s- and $p_{1/2}$-orbitals

II. Emergence of spin-orbit coupling

III. Expansion and energetic destabilisation of valence $p_{3/2}$-, d- and f-orbitals

Relativistic effects already define properties in lighter commonly known elements. It is only such that the inert nature and color of the precious metal gold, or the sole liquid metal at room temperature, mercury, can be adequately described [33–37]. Even for the simple hydrogen molecule H_2 relativistic energy contributions must be considered for most precise calculations in quantum electrodynamics. The study of SHEs explores atoms where relativistic effects are most pronounced and anomalous behaviour becomes more likely; already in 1975 Kenneth S. Pitzer speculated that elements 112, 114 and 118 were volatile and chemically inert owing to their closed shell character [31]. In copernicium, the relativistic $7s^2$ contraction leads to a smaller atomic radius than both of its closest lighter homologs mercury and cadmium [38] (see also Figure 13). Therefore SHEs provide an excellent basis for the study of relativity in atoms, while expanding the periodic table and observing the implications on the chemical behaviour.

[3] α is the fine-structure constant.

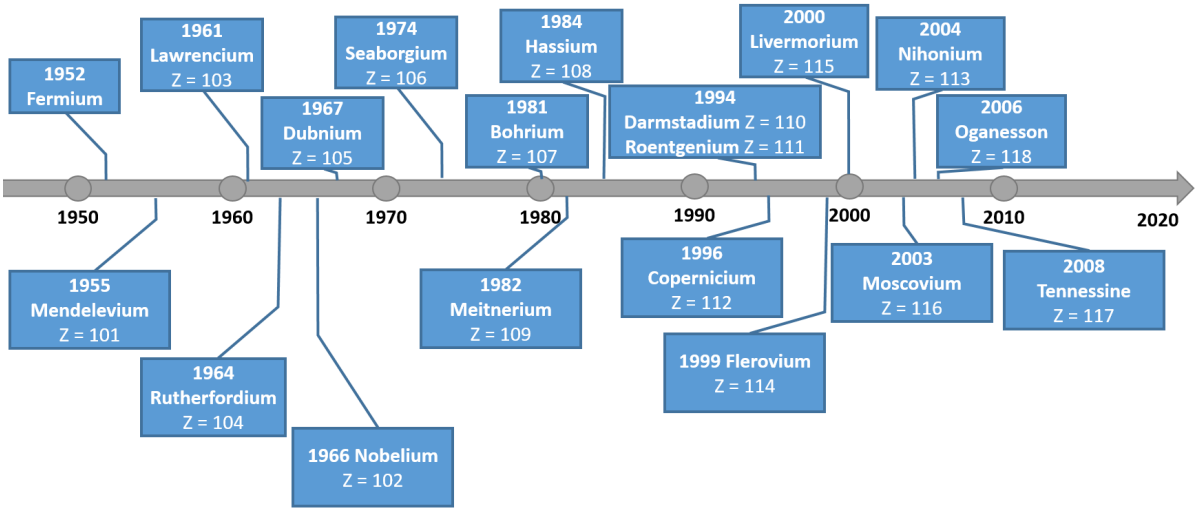

Figure 3: A timeline showing the discovery of all $Z \geq 100$ up to date. Note that some variations in discovery dates and nomenclature exist due to historic disagreements and disputed discovery claims (not shown here) [39].

A timeline of the discovery of SHEs is shown in Figure 3, with the latest discovery of tennessine ($Z = 117$) in 2008 completing the 7th period of the periodic table [40].

The discovery of SHEs has rarely been straightforward. Not just the experimental difficulties played a role historically, but also the political aspect of naming procedure, as well as the independent confirmation of experimental results. In the past there has been much twilight, even resulting in what was known as the "transfermium wars". Ambiguous claims to new elements, as well as the rushing to name them can even now cause considerable confusion when encountering literature with names such as *kurchatovium* (now rutherfordium) or *hahnium* (now dubnium) - names which were not officially accepted and have fallen out of use. The history of SHEs is even stained with false claims of discovery based on fabricated data [41]. The International Union of Pure and Applied Chemistry (IUPAC) finally settled naming disputes and set out defined guidelines for what constitutes a new element in the early 1990's [42, 43]. This is now additionally regulated by the International Union of Pure and Applied Physics (IUPAP).

1.2 Synthesis of Superheavy Elements

The present day study of SHEs relies on two stages; the successful synthesis of an element using nuclear fusion and the use of that SHE in a chemical interaction which discloses information about its properties, all within the typically short half-life of $t_{1/2} \approx 0.5$ s to 30 s. Examples given in this work will, when appropriate, be explained with the most relevant isotopes of ^{283}Cn and ^{287}Fl. These were chosen due to their half-lives being appropriate for chemistry experiments, at 3.8 and 0.48 s respectively [44].

Synthesis attempts of SHEs began in the 1960s. This arduous task was not done blindly, but rested on theories, models and knowledge of the nucleus established at the time; Advances in mass spectrometry in 1927 allowed for such fine resolution, it became apparent that the mass of a nucleus is lower than the sum of the masses of its building blocks (protons and neutrons) [45, 46]. This is known as the mass defect (Equation 1).

$$\Delta m = Z m_p + N m_n - m_{nuc} \tag{1}$$

where Δm represents the mass defect, Z the number of protons of the nucleus, $m_{p,n}$ the rest mass of a proton or neutron respectively, N the number of neutrons in the nucleus and m_{nuc} the nuclear rest mass. This discrepancy in the mass between individual nucleons and elements is represented in the binding energy of a nucleus.

1.2.1 The Liquid Drop Model

When combining the mass defect with Einstein's mass-energy equivalence, the expression for the binding energy E_b of a nucleus (Equation 2) is obtained which can be equated to the semi-empirical Bethe-Weizsäcker formula (Equation 3) [47–49]:

$$E_b = Zm_p c^2 + Nm_n c^2 - m_{nuc} c^2 \tag{2}$$

$$= a_V A - a_S A^{2/3} - a_C \frac{Z(Z-1)}{A^{1/3}} - a_A \frac{(N-Z)^2}{A} \begin{cases} +\delta(N,Z) & \text{for even } N, Z \\ +0 & \\ -\delta(N,Z) & \text{for odd } N, Z \end{cases} \tag{3}$$

where c is the speed of light in vacuum, a_V is the volume term, a_S the surface term, a_C the Coulomb term, a_A the asymmetry term, A the atomic weight and $\pm\delta(N, Z)$ the pairing term. This formula represents George Gamov's Liquid Drop Model (LDM) proposed in 1930 in which a nucleus is treated as a drop of in-compressible fluid of high density, held together by the nuclear force. A nucleus can thus be considered analogous to a weightless drop of water kept spherical due to surface-tension [50]. The binding energy is fairly constant for most stable nuclei, and when plotted over Z shows a trend of increase up to around mass number 60, followed by a decrease. Therefore, nuclei with mass numbers in that region (e.g. Fe) are the most stable.

The LDM can also be used to estimate the fissility of an isotope. The fissility parameter, f_p is given by:

$$f_p = \frac{Z^2}{A} \tag{4}$$

The calculations by Myers and Swiatecki predict that for values above $f_p \approx 16$, Spontaneous Fission (SF) becomes energetically favorable [51]. As the ratio increases, the fission barrier is decreased, thereby dramatically shortening the SF half-life. For a chemical element to exist, its half-live should be no less than $10^{-14}s$, as this is the time required for a nucleus to obtain an electron shell [39].

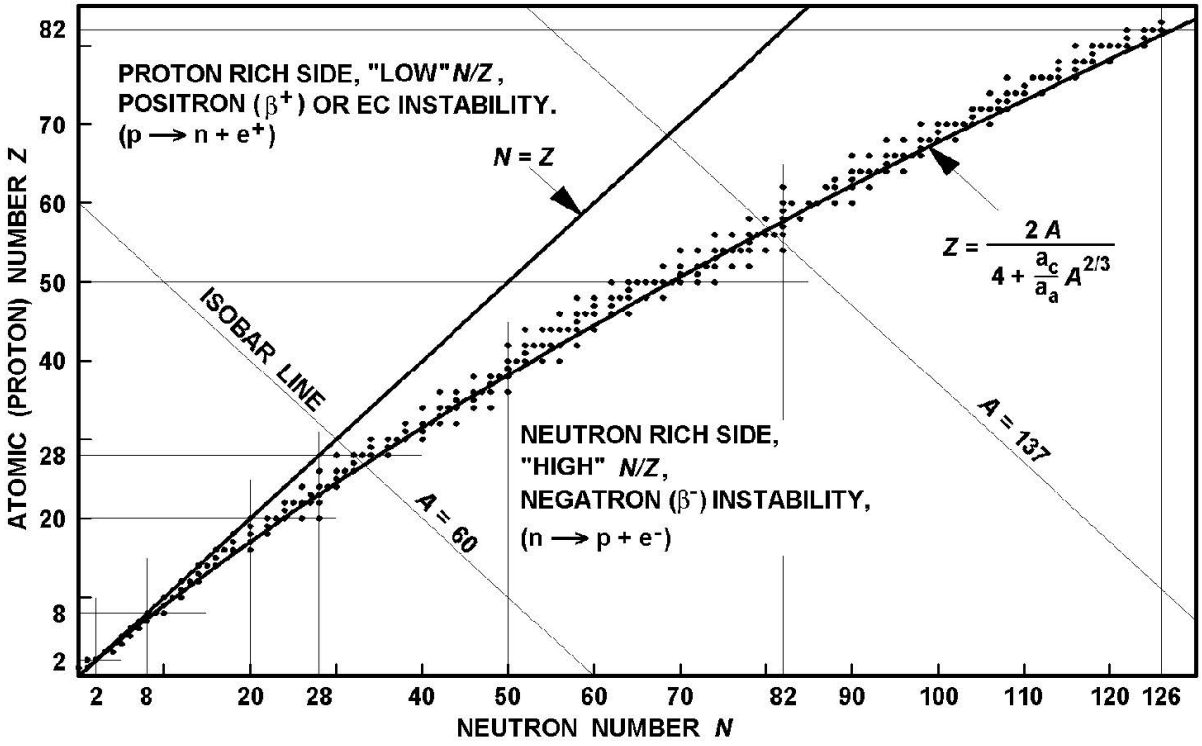

Figure 4: Stable nuclides as a function of Z and N. Note the deviation from the $N = Z$ line toward neutron rich regions. Magic numbers are indicated by $N = Z$ intersecting straight lines (see also Table 2). Image taken from [52].

Using the LDM, E_b can be maximized for each element with respect to Z for a given atomic weight A, yielding the most stable configuration of neutrons. This results in good agreement with experimental values over a large range of Z. For light nuclei $Z \simeq N$. As elements get heavier, more and more neutrons are needed to increase the binding energy without contributing to coulomb repulsion of protons. This is why looking at a nuclide chart, there is a distinct slant away from the line $N = Z$ toward the neutron-rich region (Figure 4).

1.2.2 A Nuclear Shell Model: The Island of Stability

The LDM still provides a good model for the relation of nuclear masses and respective binding energies, however falls short in the explanation of increased stability for certain proton and

neutron "magic number" configurations. Furthermore, it predicts a limit of nuclear stability at $Z \approx 104$ due to a reduced fission barrier resulting in extremely short half-lives (below the $\approx 10^{-14}s$ threshold) [53]. The LDM was succeeded by a closed nuclear shell model, in which nucleons occupy energy levels similar to electrons in different shells and earned the 1963 Nobel prize in physics shared between Eugene P. Wigner, Maria Goeppert-Mayer and J. Hans D. Jensen for their contributions [54–56].

Table 2: The currently known magic numbers for atomic number Z and neutron number N [39].

Z	2	8	20	28	50	82	
N	2	8	20	28	50	82	126

When nuclear shells are closed, additional stabilisation effects occur which represent the magic numbers (Table 2). This stabilisation effect is enhanced, when a nucleus is "doubly magic", meaning it has a closed neutron and proton shell. Several naturally occurring doubly magic nuclei exist such as ^{208}Pb and ^{48}Ca which made these two isotopes both highly sought-for and particularly successful in the synthesis of SHEs [57].

Already in the early days of searching for SHEs, the ambitious goal was proposed based on predictions of magic number regions for $Z = 114 - 126$ and $N = 164 - 184$, with the aim to increase element survivability [54, 59–62]. The region of increased nuclear stability has become known as the "Island of Stability" (Figure 5). At the Island of Stability, shell effects lead to a lower excitation energy of the Compound Nucleus (CN). This lower energy will likely increase survivability of fusion-evaporation products sufficiently for chemistry experiments and allow them to resist SF long enough to undergo de-excitation. There are a number of models in place to calculate shell stabilization effects [63]. Doubly magic nuclei tend to have a spherical shape, and for a time superheavy nuclei were thought to be mostly spherical [51, 64, 65]. While superheavy nuclei also experience deformation, the most stable doubly magic isotopes searched for at the "peak" of the Island are still idealized as near-spherical [66]. Taking flerovium as an example, currently synthesized isotopes are quite neutron-deficient compared

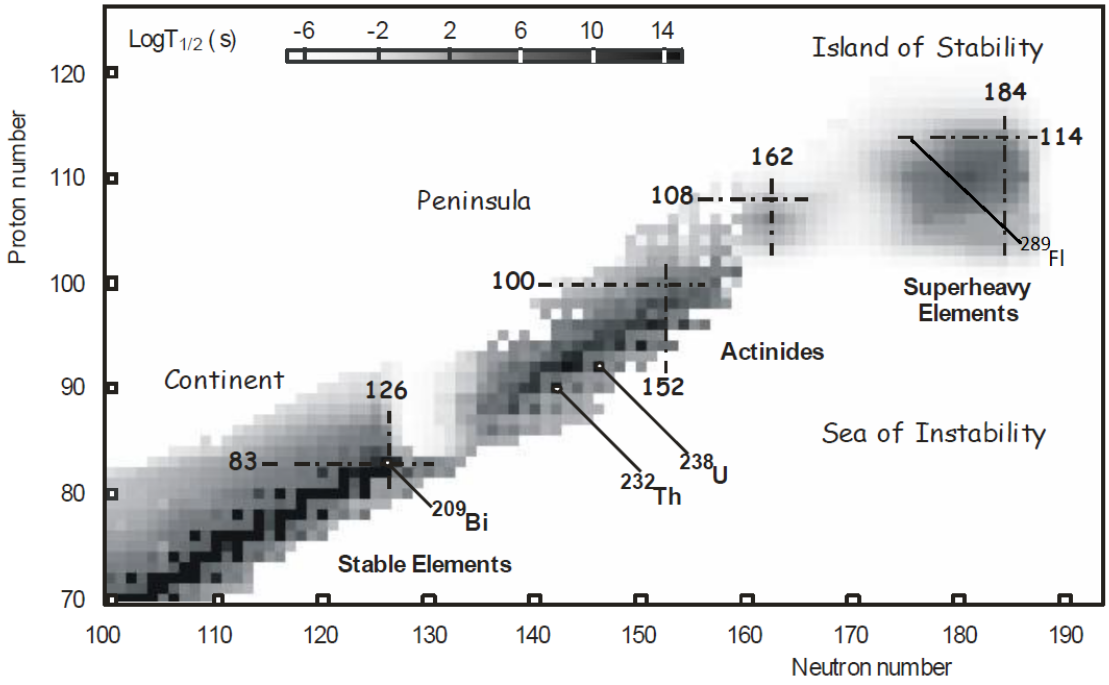

Figure 5: The heavy region of the nuclide chart illustrating the metaphor of the island of stability. Black squares represent stable isotopes, with the lightening shades of grey indicating shortening half-lives. The 'continent' of stable elements represents the familiar homeland from which voyages across the sea of instability to the promised Island of Stability around $Z = 114$, $N = 184$ can be undertaken. The heaviest confirmed isotope of element 114 shown to indicate the distance of currently synthesized isotopes from the island. Image taken from [58].

to the predicted $N = 184$. Experimental values show an increasing half-life trend toward heavier isotopes (Figure 6).

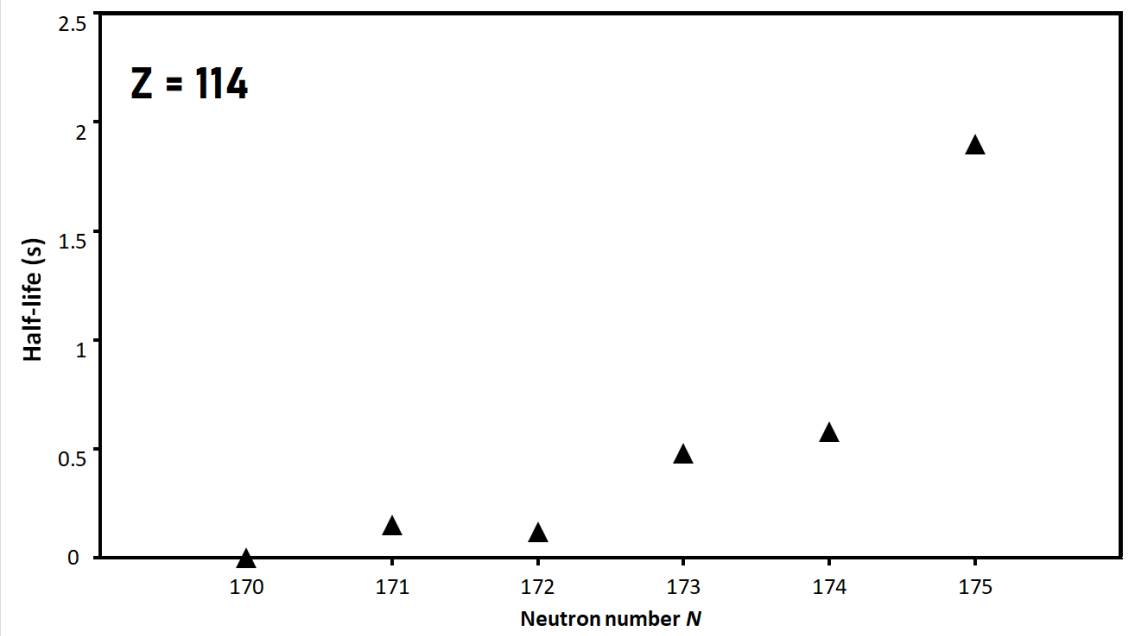

Figure 6: Isotopes of flerovium (Fl, $Z = 114$) with corresponding half-lives. Toward the predicted $N = 184$, the half-life increases. Data from [44].

1.2.3 Nuclear Fusion

Due to the aforementioned fermium gap, it became necessary to rely on nuclear fusion evaporation reactions for SHE production. In nuclear fusion, a projectile is accelerated using a suitable accelerator to high speeds overcoming the electrostatic repulsion (Coulomb barrier, E_{cb}) between two nuclei (Figure 7) given by [67, 68]:

$$E_{cb} = k\frac{Z_1 Z_2}{A_1^{1/3} + A_2^{1/3}} \tag{5}$$

where k is Coulomb's constant, $Z_{1,2}$ the projectile and target proton number, and $A_{1,2}$ the mass number. However, this energy alone is not sufficient to result in a compound nucleus. Energies at the coulomb barrier will merely cause nuclei to exchange some nucleons, but nevertheless result in fission (in a process deemed quasi-fission) [69, 70]. Therefore an additional amount of energy, which sums to E^*_{min} is required to allow the projectile to penetrate the target nucleus and allow nucleons to rearrange into a compound nucleus [71] given by Equation 6:

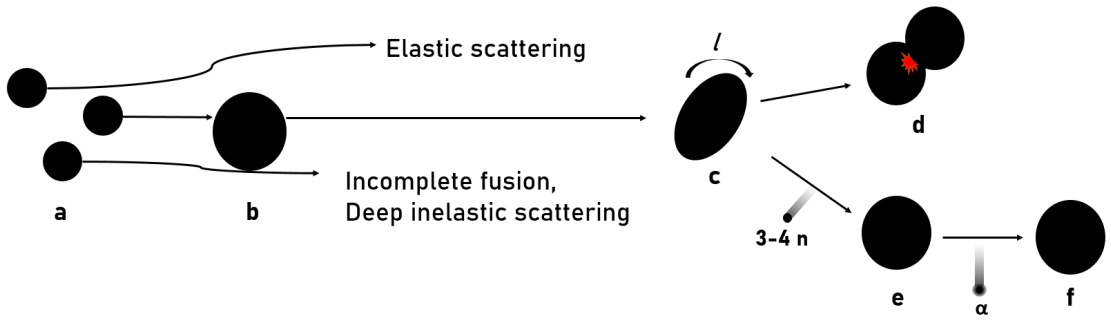

Figure 7: Schematic representation of SHE nuclear fusion evaporation reactions and the possible fates of the target nucleus. (a) heavy ion beam, in this case ^{48}Ca. (b) stationary target, in this case ^{242}Pu. Projectiles far from a target nucleus experience elastic scattering, while projectiles "grazing" the target nucleus result in nuclear transfer reactions, spallation and other unwanted side products. (c) excited compound nucleus from on-target projectiles with angular momentum l which can either (d) undergo spontaneous fission or (e) dissipate the excess energy through 3 n release to the desired product below neutron separation energy, evaporation residue ^{287}Fl. Given the angular momentum l is not above a critical value, the nuclear fusion evaporation product (e) can then undergo α emission to decay to its daughter ^{283}Cn.

$$E^*_{min} = E_{cb} + Q \tag{6}$$

where the Q-value represents the change in energy stored or lost in the form of matter, according to the difference in mass defects between the reactants and products. E^* is known as the excitation energy. If the Coulomb barrier is overcome, successful fusion will result in a CN, an excited nucleus which carries the excess energy of the nuclear reaction in it. Even with fusions at the minimum kinetic energy possible a CN will inevitably carry several MeVs excitation energy, as more energy is required to overcome the Coulomb barrier than energy is consumed in the fusion process [72]. The excitation energy for a particular nuclear fusion evaporation reaction can be calculated using:

$$E^* = E_{cm} + Q \tag{7}$$

where E_{cm} is the center-of-mass collision energy. With larger E^*, SF becomes more likely. The magnitude of E^* is used to categorize the fusion as "hot" or "cold". Cold fusion reactions generally are done near E^*_{min} and result in the de-excitation with less neutrons and photons (see Figure 8). Hot fusion reactions on the other hand use much greater projectile energies, resulting in a higher E^*. It is however no longer the preferred method for SHE synthesis due to lower survival probabilities. Both approaches are inefficiently used for elements with $Z \geq 112$ at present. The most successful approach up to date for the very heaviest nuclei has been the use of the doubly magic ^{48}Ca projectile using a "warm" fusion approach, an intermediate energy region between hot and cold ($\approx$ 40 MeV) usually resulting in the evaporation of 3-4 neutrons. Due to the enhanced stability of closed nucleon shells, survivability of compound nuclei increased making doubly-magic ^{48}Ca projectiles, as well as doubly-magic ^{208}Pb targets the most successful approach at SHE production to date.

1.2.4 The Cross Section

The newly formed CN must release its excitation energy which often results in SF. Only few of the successfully formed CN live long enough to undergo a more lengthy de-excitation process; the evaporation of multiple neutrons and photons, resulting in an Evaporation Residues (ER). The ER represents the desired fusion product between all the possible unwanted outcomes. Proton evaporation is also possible, but by orders of magnitude less likely [74, 75]. This is due to the higher number of neutrons in nuclei, as well as the lower energy needed to eject them from the nucleus ($\approx$ 12 MeV for protons, $\approx$ 9 MeV for neutrons) [67].

The cross-section σ of a particular nuclear reaction increases with its probability, and for the successful formation of an ER is given by Equation 8 [71]:

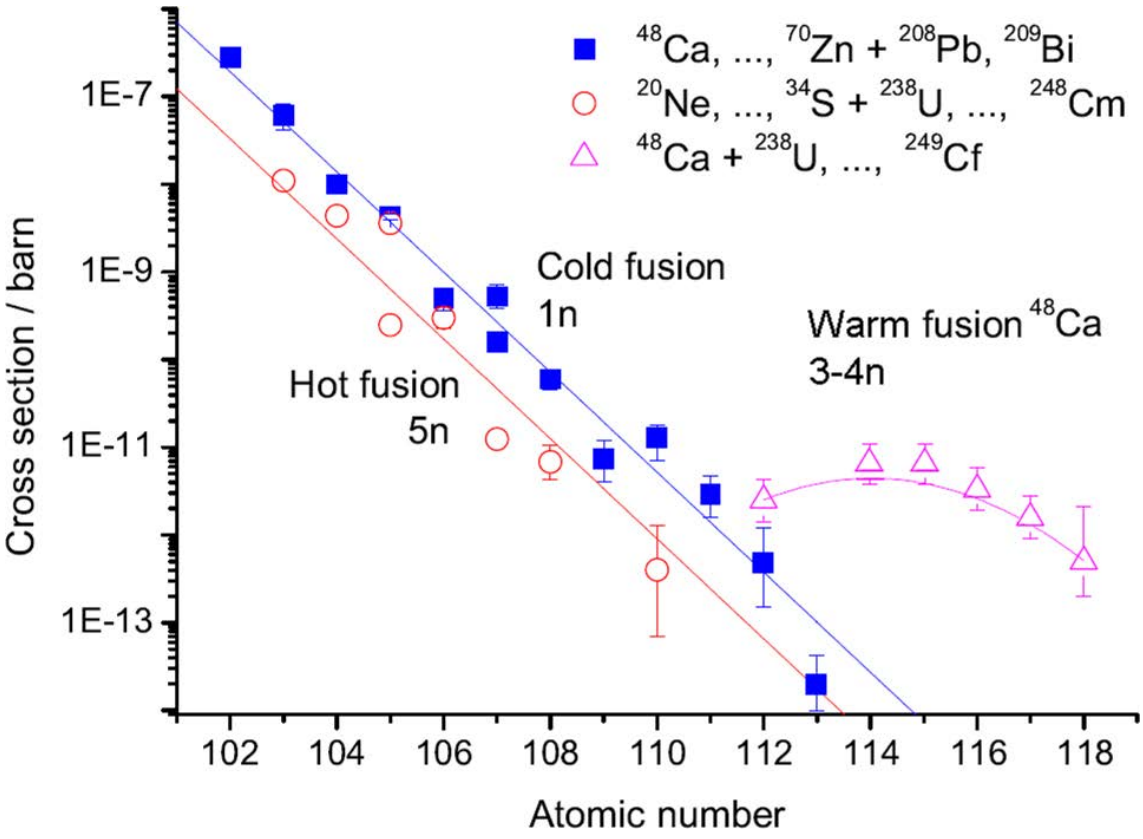

Figure 8: Experimental fusion evaporation reaction cross sections for nuclei with $Z \geq 102$. Shown are the 1n cold fusion evaporation reactions (squares), the 5n channel of hot fusion (circles), and for the 3-4n of warm fusion (triangles). Image taken from [73].

$$\sigma^{xn}_{EVR}(E) \approx \frac{\pi}{k^2} \sum_{l=0}^{\infty} (2l+1) \cdot P_{cont}(E,l) \cdot P_{CN}(E^*,l) \cdot P_{xn}(E^*,l) \tag{8}$$

where $\sigma^{xn}_{EVR}(E)$ is the reaction cross section for the x neutron evaporation channel, and k is the wavenumber. The cross section stems out of three probabilities;

I. $P_{cont}(E,l)$ - Probability for nuclei to come into contact

II. $P_{CN}(E^*,l)$ - Probability forming CN at excitation energy E^* and angular momentum l

III. $P_{xn}(E^*,l)$ - Probability to survive x evaporations and form the ER

It is evident, that the angular momentum l of the CN caused by the collision with the projectile plays an important role in this interaction. Projectiles far off-target will cause very large l, and results in deep inelastic scattering or a mere exchange of nucleons (quasi-elastic fission), completely foregoing the formation of a CN (see Figure 7). This quasi-elastic fission results in nuclear transfer reaction products, able to produce most lighter elements in the periodic table, essentially undesired byproducts. For projectiles on-target, l of a successfully formed CN also plays a role in its survival; for values too large will result in spontaneous fission, while lower l have the greatest chances of forming an ER [76, 77]. Consequently, as successful fusion mainly occurs with on-target projectiles, the spread of ERs recoiling out of the target is relatively narrow, with a deviation of $\approx 10^{\circ}$ from the beam axis [78–80]. As the cross section is directly related to the probability of successful fusion, it is of course critically important.

Typical SHE cross sections are in the *picobarn* region (Figure 8). To find the number of evaporation residues, N_{ER} produced for a particular reaction, the following equation can be used:

$$N_{ER} = \varepsilon \cdot N_{projectile} \cdot N_{target} \cdot \sigma \tag{9}$$

where ε is the efficiency of detection for the particular experimental setup (including transport losses, losses inherent in the experimental setup), σ is the SHE cross section, N_{target} is the number of target atoms exposed to the beam and can be obtained by multiplying the irradiated area by the target thickness and density. $N_{projectile}$ is the total number of atoms fired at the target and is usually experimentally determined by measuring the beam current. It is given by

$$N_{projectile} = \int_{t_0}^{t_f} I_b \, dt \cdot \frac{1}{C_p e} \tag{10}$$

where I_b is the ion beam current, integrated over time of the experiment (from start time - t_0, to final time - t_f), C_p is the charge of the projectiles in the beam and e the elementary charge ($= 1.602 \cdot 10^{-19}$ C). For example, the reaction used in this work (see also Chapter 5)

^{48}Ca(^{242}Pu,3n)^{287}Fl

with $\sigma = 7$ pb, $N_{target} = 2.48 \cdot 10^{18}$ atoms, a total beam integral of $N_{projectile} = 3.34 \cdot 10^{18}$ atoms and assuming no loss in efficiency, this corresponds to 58 ^{287}Fl atoms produced for the duration of the 26 days of continuous irradiation, or ≈ 2 atoms/day.

1.2.5 Targets

SHE target materials are an essential component to the synthesis process. They must be produced in a specific, uniform thinness so that ERs can recoil out. Furthermore, as they are exposed to high-intensity, high-energy heavy-ion beams for long periods of time, they must generally have a high melting point, capable of diverting the heat deposited in them by the beam yet strong enough to withstand some mechanical stress [72]. Thin targets are less capable of conducting the heat built up. Target overheating can cause melting, change in the thickness or brittleness (Figure 9) [81, 82]. Several means to keep the temperature moderate have been employed, often in combination. Moving target wheels allow for cooling of target segments while they are not being directly irradiated, while targets are sometimes cooled by gas streams [83, 84]. Currently available targets are pushed to their limits given the ever-increasing beam intensities of modern upgraded accelerators. Target sputtering, localized melting and release of carbon contaminants can all cause issues during experimentation [85]. For example, target sputtering and melting can change the carefully selected target thickness, resulting in sub-optimal beam energies as well as loss of target material. Impurities such as carbon compounds can adversely affect gas chromatography based experiments by causing contamination in the tightly controlled inert gas mixture (see Chapters 5, 6). Past chemistry experiments with Cn suffered from periodic contamination of the detectors repeatedly from 2007 to present. One such identified likely source is ejection of carbon compounds from the target material[4].

Target production can be done in a number of ways, with electrodeposition generally being the most popular, as it produces uniform and somewhat adherent films [87–89]. The choice of

[4]From Paul Scherrer Institute experimental records 2008, 2009, 2013 and 2015.

Figure 9: A rotating ^{249}Cf target wheel after bombardment with ^{50}Ti heavy ion beam. The once smooth banana-shaped target sections have suffered deformation due to prolonged irradiation. Image from [86].

target material stems from the fusion reaction chosen, and asymmetrical reactions (lighter projectile with heavier targets) are preferred due to higher cross sections, such as the ^{48}Ca-induced fusion. Therefore heavier targets such as actinides are preferred. Actinide target materials with $Z > 98$ are practically unavailable today, which makes heavier fusion projectiles necessary. Additionally, due to the aforementioned increasing N/Z ratio for heavier nuclei, any naturally available projectile-target combination in the fusion process will inherently result in neutron deficient CN.

1.2.6 The Synthesis of Cn via Fl

There are countless combinations of elements that could, in theory, result in copernicium isotopes. There are however, very few that will result in efficient, successful fusion. In the 1996 discovery of Cn, the reaction

$$^{208}\mathrm{Pb}(^{70}\mathrm{Zn}, \mathrm{n})^{277}\mathrm{Cn}$$

was used [90]. The reported cross section was ≈ 1 pb. A doubly magic target nucleus was employed, and the cold fusion led to the evaporation of only one neutron. Two decays attributed to the SHE were recorded over the course of 23 days. The 1 pb cross section is reasonable for SHE, but the ER is severely neutron deficient. It is still the lightest Cn isotope known to date and has the half-life of 0.69 ms, too short for any chemistry experiments.

The two isotopes most interesting to chemists are ^{283}Cn and ^{285}Cn, due to their relatively longer half-lives (3.8 s and 29 s respectively). ^{283}Cn can be produced directly with sufficiently large cross sections of about 2 pb in the reaction [91]:

$$^{238}\mathrm{U}(^{48}\mathrm{Ca},3\mathrm{n})^{283}\mathrm{Cn}$$

A common reaction for chemistry purposes, and the chosen pathway for this work is

$$^{242}\mathrm{Pu}(^{48}\mathrm{Ca},3\mathrm{n})^{287}\mathrm{Fl} \longrightarrow {}^{283}\mathrm{Cn} + \alpha$$

which is an indirect pathway as the ^{287}Fl decays to ^{283}Cn via α-decay [92]. The doubly magic ^{48}Ca is also employed. This reaction is beneficial due to higher cross sections (Figure 10). While 2- and 4 n evaporation channels also exist, these do not produce Cn isotopes long-lived enough for chemistry and will therefore not be considered here.

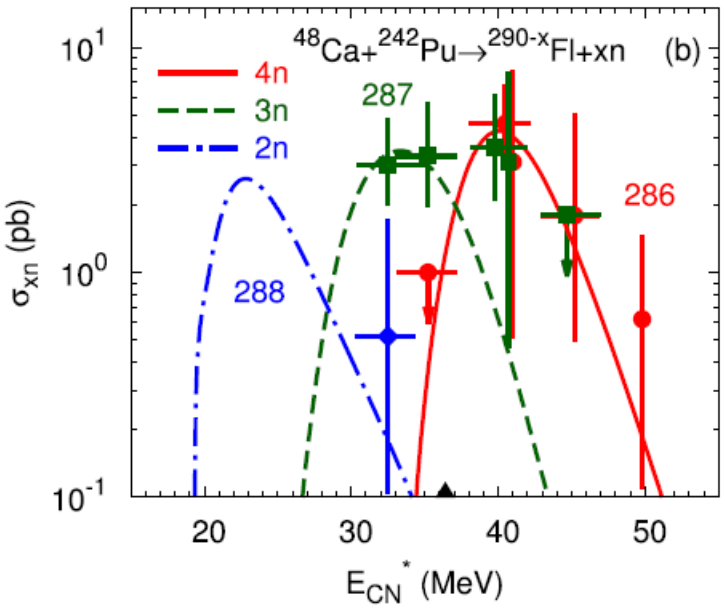

Figure 10: Production cross sections for the ^{48}Ca on ^{242}Pu reaction with 2n to 4n evaporation channels as a functions of the excitation energy of the CN. Image and calculated values (lines) from [93], symbols are experimental data from [94].

The most desirable Cn isotope at first glance is the comparatively neutron rich ^{285}Cn with a half-life of 29 s. Its synthesis however, is obstructed by the lack of suitable target materials. Direct synthesis via ^{240}U is not possible due to the target's 14 h half-life. The next-best pathway again is the indirect production via

$$^{244}\mathrm{Pu}(^{48}\mathrm{Ca}, 3\mathrm{n})^{289}\mathrm{Fl}$$

with the reasonably good cross section of ≈ 2-7 pb [94–96]. ^{244}Pu is an extremely rare isotope, thought to only occur in minuscule trace amounts on earth from primordial sources produced in the stellar rapid neutron-capture process (r-process) [97, 98]. Unlike other Pu isotopes, it cannot be produced in the nuclear fuel cycle, as the lighter isotope ^{243}Pu with its short half-life prohibits further neutron captures. Earth's resources are therefore very limited to some astronomical, and few anthropogenic sources stemming from high-flux reactors and

nuclear weapons tests [99]. The main source of ^{244}Pu is from decay of ^{248}Cm. ^{248}Cm in turn is available in gram quantities[5] [100].

1.2.7 Superheavy Element Detection

A crucial part in SHE research is the detection of single atoms. Fortunately, their radioactive nature makes it possible to sense substances even at one-atom-at-a-time level. The first step, naturally, lies in the production of new elements and establishing their decay properties. Almost all SHE decay via two modes: α-decay and SF. Electron capture is also possible for some, due to the neutron deficient nature of currently known isotopes. False reports of decay data have caused confusion in the past and can even render entire experimental campaigns meaningless. It is therefore imperative to study SHE decay before chemistry experiments can be done.

SHE are detected via their α-particles and SF fragment spectroscopy, which are both distinct highly energetic [65]. This spectroscopy helps to unambiguously identify an element above the noise and background signals often present [101]. Finally, half-life data can be used to identify specific decay chains. By detecting a potential SHE decay at a given time, one can search for the daughter decay. Statistically, for multiple highly energetic α-particles in short sequence followed by SF occurring randomly or unrelated is extremely low [102].

[5] from the decay of ^{252}Cf, produced both in reactors and particle accelerators.

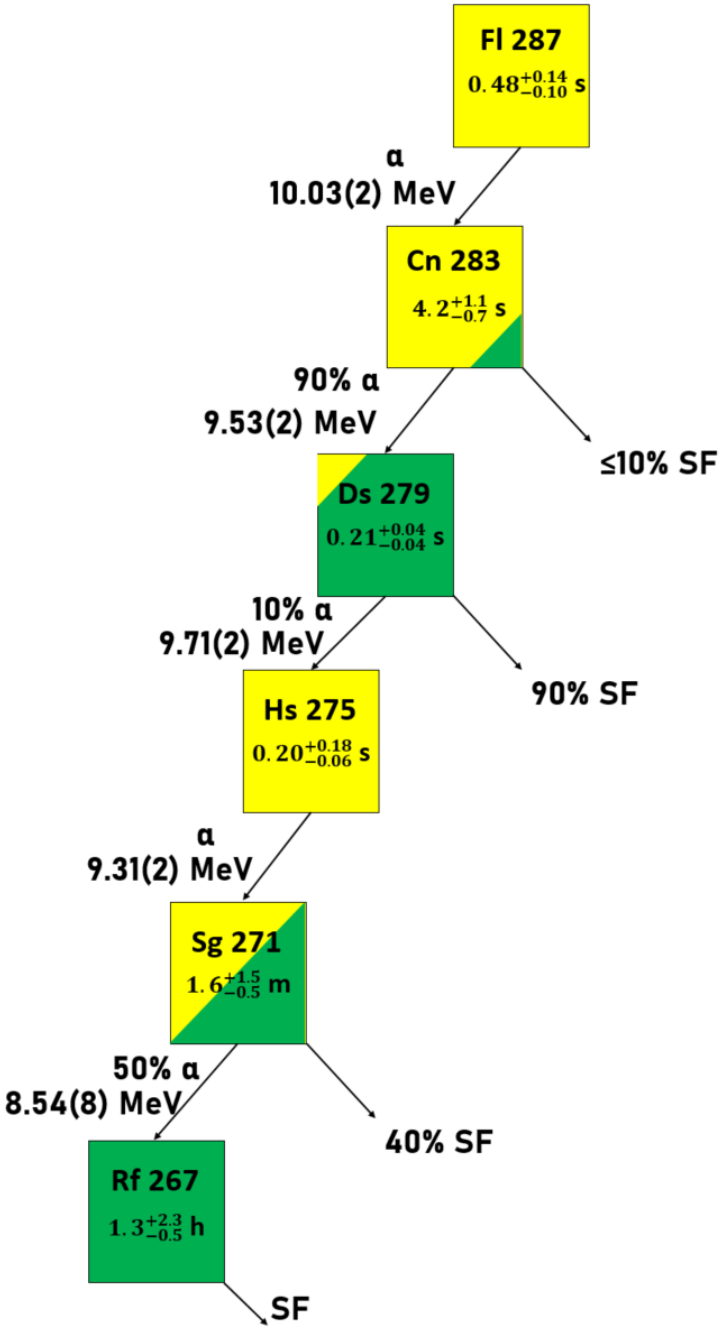

Figure 11: Decay properties of ^{287}Fl showing all possible decay daughters and SFs. α-decay shown in yellow, SF in green squares. Uncertainties shown in brackets, data from [103].

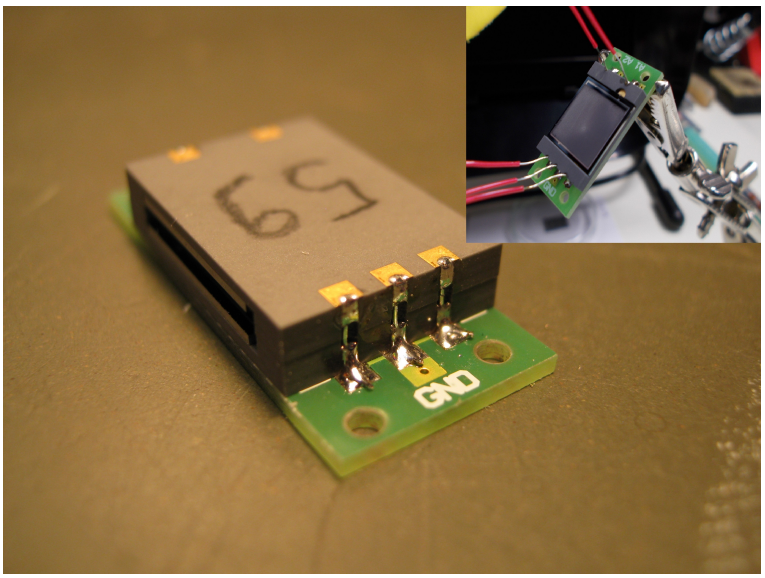

Figure 12: Image of a PIN diode sandwich forming a chromatographic channel in the gap between the top and bottom detectors. Top right shows a bottom detector covered in a thin grey selenium film alone.

In this work, the detection of α-particles and SF was done using a 64 Positive Implanted N-type (PIN) diode α-particle and SF detector array (Image 12). These PIN diodes were arranged in a "sandwich" geometry, effectively making up a two-sided 32 cm chromatographic column with 1 cm length resolution. The sandwich geometry enabled detection capabilities on both sides of the chromatographic channel with an almost 100% detection efficiency for SF fragments and 86% for $\alpha-$particles from atoms deposited on the active area of the detector surface [104, 105].

1.3 The Study Methodology of SHE and Homologs

Elements produced at the limit of stability using the violent method of fusion deserve appropriately specialized experimental techniques. The main hurdles standing in the way of performing chemistry with SHEs once they have been produced can be reduced to two principal issues:

I. Short half-lives

II. Low cross sections resulting in single-atom chemistry

Nuclear transfer reaction products can also interfere with SHE detection by increasing the signal background in the respective α-spectra region of interest. Working with a physical pre-separator, which selectively allows SHE to enter the experiment, can minimize such interference. These pre-separators can also have downsides (such as transmission losses) but their discussion is beyond the scope of this work. For further information, the reader is encouraged to find resources about existing pre-separators such as TASCA [79], GARIS-I & II [78, 106], DGFRS-1 & 2 [107–109], and SHIP [110].

SHE experiments can use liquid-phase and gas-phase chemistry depending on the predicted chemical properties and half-lives of the isotope studied. Elements Hs, Rf, Db, and Sg all have been studied successfully in the liquid phase [111–117]. The main features of liquid-phase chemistry with heavy elements produced in nuclear fusion reactions is the collection of the products on a substrate, which can easily be dissolved. Alternatively they are collected on aerosols using a gas-jet technique and then dissolved in an aqueous solution. The resulting solution is then chemically separated, usually using an ion-exchange column or liquid-liquid extraction and the products are identified by subsequent α- and SF spectroscopy of collected fractions. The time required to collect and dissolve samples followed by separation in these experiments is the rate determining step. Only elements with $t_{1/2} > 30$ seconds can be detected using such methods. Later chemistry experiments employed gas chromatography as the primary method, which will be discussed in detail later.

Rutherfordium (Z = 104) was first chemically investigated using the ^{242}Pu(^{22}Ne,3n)^{260}Rf ($t_{1/2} = 70$ s) reaction in Dubna by Zvára *et. al.* where the SHE recoiled into a 3:1 chlorinating agent mixture of $NbCl_5$ and $ZrCl_4$ vapors and nitrogen as carrier gas and was transported onto a mica SF detectors [118, 119]. This work was however long considered inconclusive [120] and a liquid phase experiment was later done. The ^{248}Cm(^{18}O,5n)^{261}Rf ($t_{1/2} = 70$ s) reaction was used at Lawrence Berkeley National Laboratory by Silva *et al.* in a cation exchange chro-

matography column using organic chelating agents. Evaporation residues were stopped in a He gas jet and flushed onto the surface of a mechanical rabbit which was washed, transferring the SHE into solution [121].

Dubnium (Z = 105) was first chemically investigated using the ^{243}Am(^{22}Ne,3-5n)$^{262-260}$Db ($t_{1/2} = 1.5 - 33.8$ s) reaction in Dubna by Zvára *et. al.* again by chlorination of the ERs in a stream of nitrogen, then gas thermochromatographic separation, albeit the experiment was inconclusive [122]. Db chlorides were observed to be less volatile than their Nb homolog but later reevaluation of the data suggested similar ΔH_{ads} values for both [73, 123]. It was later identified by Gregorich et. al. by chemical separation in the aqueous phase [117].

Seaborgium (Z = 106) was first chemically investigated using the ^{249}Cf(^{18}O,4n)^{263}Sg ($t_{1/2} =$ 1 s) reaction in Dubna by formation of chlorides and oxychlorides with $SOCl_2$ in an argon carrier gas thermochromatography, again with inconclusive results [124]. The same year, liquid-phase experiments at Darmstadt were performed. ERs were stopped in a He(KCl) aerosol gas stream which was deposited on a glass plate [112]. This was washed with HNO_3/HF solution into a cation exchange column whose eluent was dried and measured for α- and SF decay, however only the decay daughters Rf and No were detected. Later experiments formed Sg oxide hydroxide in gas streams and detected the SHE directly [125].

Bohrium (Z = 107) was first chemically investigated using the ^{249}Bk(^{22}Ne,4n)^{267}Bh ($t_{1/2} =$ 17 s) reaction where ERs were stopped in a He gas stream on a carbon aerosol which transported them to a 1000 °C quartz wool oven [126]. The Bh then reacted with added HCl and O_2 gases to form volatile BhO_3Cl and was transported through a quartz chromatographic column to a α- and SF detector.

Hassium (Z = 108) was first chemically investigated in the gas-phase at Gesellschaft für Schwerionenforschung (GSI), Darmstadt using the ^{248}Cm(^{26}Mg,4-5n)$^{269-270}$Hs (^{269}Hs $t_{1/2} =$ 9.7 s, ^{270}Hs $t_{1/2} = 3.6$ s) reaction where ERs were stopped in a He gas stream with 10% O_2 content and passed over a 600 °C quartz wool segment to facilitate oxidation [127]. The tetroxide HsO_4 was passed over a quartz surfaced PIN detector array with a negative temperature gradi-

ent in the Cryo On-Line Detector (COLD).

Meitnerium (Z = 109) - No experimental chemical investigations have yet been done [128].

Darmstadium (Z = 110) - No experimental chemical investigations have yet been done [128].

Roentgenium (Z = 111) - No experimental chemical investigations have yet been done [128].

Copernicium (Z = 112) was first chemically investigated at FLNR, Dubna in 2007 using the indirect ^{242}Pu(^{48}Ca,3n)^{287}Fl (^{283}Cn $t_{1/2}$ = 3.8 s) reaction. ERs were stopped in a He-Ar noble gas mixture and transported in elemental form to the COLD array with a negative temperature gradient applied along the detector [129]. Fl was also investigated in parallel at that point and during follow-up experiments.

Nihonium (Z = 113) - a first claim for a chemical investigation ^{243}Am(^{48}Ca,3n)^{288}Mc (^{284}Nh $t_{1/2}$ = 0.97 s) alongside Mc in 2020 at GSI, Darmstadt where ERs were stopped in a noble gas stream and transported over a quartz surface followed by a gold surface in the Cryo-Online Multidetector for Physics and Chemistry of Transactinides (COMPACT 1 & 2) detectors [130, 131]. Other attempts at chemical investigation include vacuum adsorption chromatography [128, 132].

Flerovium - (^{287}Fl $t_{1/2}$ = 0.48 s) was simultaneously produced for the copernicium experiments (see copernicium). Due to the short half-life, few atoms have ever been observed and its chemistry is still a point for debate [129, 133].

Moscovium (Z = 115) (^{288}Mc $t_{1/2}$ = 170 ms) The Nh investigation was through indirect synthesis via ^{288}Mc in 2020 and observed in parallel (see nihonium).

Livermorium - No experimental chemical investigations have yet been done.

Tennessine - No experimental chemical investigations have yet been done.

Oganesson - No experimental chemical investigations have yet been done.

1.3.1 The Element Copernicium

This work specifically focuses on the SHE copernicium ($Z = 112$) and its nearest homolog mercury ($Z = 80$). SHEs are usually researched in the context of their lighter homologs as this sheds some light on trends in the periodic table. Cn was first successfully synthesised in 1996 at the Gesellschaft für Schwerionenforschung (GSI) in Darmstadt, Germany [90]. This element is of special interest to chemists for a number of reasons. Due to the half-lives of its isotopes it is currently one of the heaviest elements that are stable long enough to make it readily accessible for chemical investigations. It is among the heaviest elements that has been experimentally characterized [105, 129]. Its position in the periodic table and therefore its electronic structure is of high interest; its proposed electronic structure of [Rn]$5f^{14}6d^{10}7s^2$ suggests a closed s- and d-shell. [134, 135].

Let us consider the more familiar homolog Hg. One can already observe extraordinary properties in this element - the only liquid metal at room temperature and almost entirely monomeric in the gas phase, $Hg_{(g)}$. Hg has the electronic structure [Xe]$4f^{14}5d^{10}6s^2$, with a closed set of sub-shells similar to Cn. The first ionisation potential is 10.43 eV, a rather high value [136]. This explains its relative inertness and the possibility to find it in its elemental state in nature. The following two ionisation potentials are 18.64 (2nd), and 34.4 eV (3rd) respectively, effectively ruling out compounds past the +II oxidation state.

1.3.2 Relativistic Effects in Copernicium

The basis for relativistic effects on chemistry are built on the relativistic one-electron equation of Paul Dirac, which for one electron in potential $V(r)$ is given by [137]:

$$h\psi = (c\alpha p + \beta mc^2 + eV(r))\psi = E\psi \tag{11}$$

The solutions can then be used as a one-electron states in a single Slater determinant [32]

$$\Psi(N) = |\psi_1(1)\psi_2(2)...\psi_N(N)| \tag{12}$$

with the Hamiltonian

$$H = \sum_i h_i + \sum_{i>j} \frac{1}{r_{ij}} \tag{13}$$

the relativisitc Hartree-Fock or Dirac-Fock equation is obtained (Equation 14).

$$H\Psi = E\Psi \tag{14}$$

The solutions for Equation 14 up to atomic number $Z = 120$ are tabulated by Desclaux [138] and for group 12 are presented in Table 3.

Table 3: Total energies of the atoms (in atomic units) for group 12 elements as calculated by Desclaux [138]. E_r is relativistic, E_{nr} is non-relativistic energy. A column showing the ratio to highlight the magnitude of the relativistic effect.

Z	Element	$-E_r$	$-E_{nr}$	Ratio (E_r/E_{nr})
30	Zn	1794	1778	1.009
48	Cd	5589	5465	1.023
80	Hg	19624	18409	1.066
112	Cn	47234	40937	1.154

As a crude approximation, some simple calculations can be done to highlight relativistic effects on an atom. Mercury already experiences significant relativistic effects on its electrons. As an example, using Albert Einstein's relativistic mass-energy equivalence, the mass of an electron orbiting a Hg nucleus is corrected [139]:

$$m_{rel} = \frac{m_0}{\sqrt{1 - (\frac{v}{c})^2}} \tag{15}$$

where m_{rel} is the relativistic electron mass, m_0 the electron mass ($= 9.109 \cdot 10^{-31}$ kg) at rest, and v the speed of an electron in orbit. To find an approximation for v, the Bohr model for a hydrogen-like species[6] electron in orbital n can be used:

$$v = \frac{2\pi e^2}{nh} Z \tag{16}$$

where e is the elementary charge ($= 1.602 \cdot 10^{-19}$ C) and h is Planck's constant ($= 6.62 \cdot 10^{-34}$ J/Hz). Similarly, the Bohr model can be used to approximate the radius r of an orbital according to:

$$r = \frac{Ze^2}{mv^2} \tag{17}$$

(16) can be solved for the velocity of a given electron. Using the velocity, (15) can then be solved. The relativistic mass and rest mass can then be used in Equation (17) to result in the different radii. It becomes apparent that the radius of the relativistic orbital size changes. This can be done for the elements in a group, highlighting the increasing magnitude of the relativistic effects (Figure 13).

[6]This is an approximation for an atomic nucleus of infinitesimal (zero) radius.

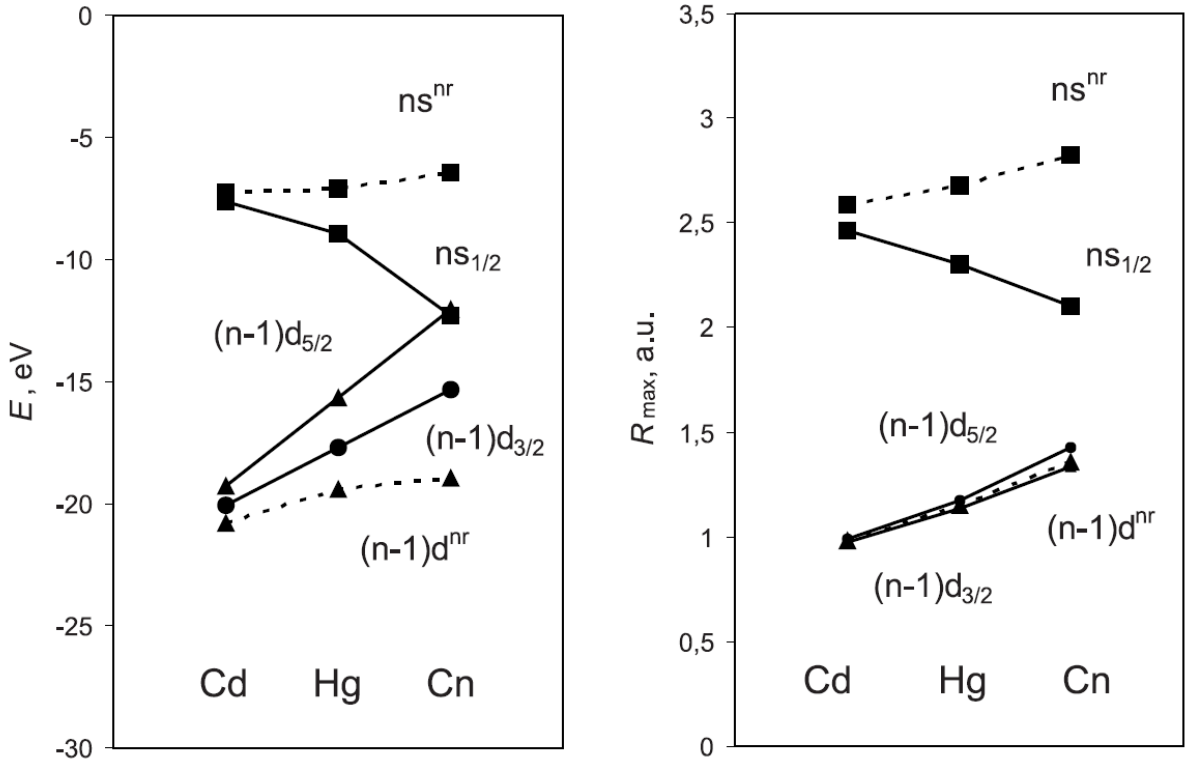

Figure 13: Relativistic (solid line) and non-relativistic (dashed line) energies and maximum radius (R_{max}) of the valence $s-$ and $d-$ atomic orbitals of group 12 elements. Relativistic values obtained using Dirac-Fock equation. Picture taken from [134], data from [138].

For a mercury atom, an s electron travels at near 60% the speed of light, thus resulting in a near 25% shrinkage in the Bohr radius. Such effects are even more pronounced for the much heavier Cn with greater Z.

1.3.3 Physical Properties and Group 12 Trends

This section will discuss established and theoretical properties of element 112 in context to its lighter homologs. The proposed $7s$ and $7p_{1/2}$ valence electron stabilization of Cn and Fl respectively let researchers suspect noble gas-like properties; inert with high volatility. They were thought to occur in the elemental state and investigated as such [105, 123, 129, 140]. A

summary of the known and predicted properties of the group 12 elements can be found in table 4.

Table 4: A summary of the group 12 element properties. Data unless otherwise noted from [141]. Predicted properties *a* from [36], *b* from [142], *c* from [143], *d* from [144], *e* from [145].

Property	Zn	Cd	Hg	Cn
State (STP)	Solid	Solid	Liquid	Liquid[a]
Melting point (°C)	420	321	-38.8	10 ± 11[a]
Boiling point (°C)	907	767	357	67 ± 10[a]
density (g/cm^3)	7.14	8.65	13.5	14.7-23.7[a,b]
Preferred ox. states	+2	+1, +2	0, +1, +2	0, +2[b]
1st IP (eV)	9.4	9.0	10.4	12.0[c], 13.0-13.8[d]
2nd IP (eV)	18.0	16.9	18.8	22.5[c], 21.1[b]
Atomic Radius (v. d. Waals, pm)	201	218	223	171[e]

The first chemical experiments on Cn were designed to search for these properties. Cn was tested in parallel with Hg and Rn by Yakushev et al. by comparing the adsorption of the elements on metallic surfaces in a gas chromatography setup [146]. Gold covered detectors were chosen as these elements would likely only show their metallic character in contact with noble metal surfaces. "Hg-like" behaviour of Cn would likely result in a strong adsorption interaction, or noble gas ("Rn-like") behaviour would result in more inert behaviour towards the gold [147]. Despite repeated experiments, no decays attributable to 112 were detected. Several follow-up studies were performed, equally fruitless [148, 149]. While Cn spontaneous fission was being detected, it appeared the atoms were not reaching the detector setup. It was only later discovered that the half-life of the isotope under investigation, ^{283}Cn, was much shorter than the $\approx 80s$ initially determined [101, 150]. This caused the atoms to decay during the long transport times.

Two successive experiments in 2006 and 2007 which accounted for the short half-life fi-

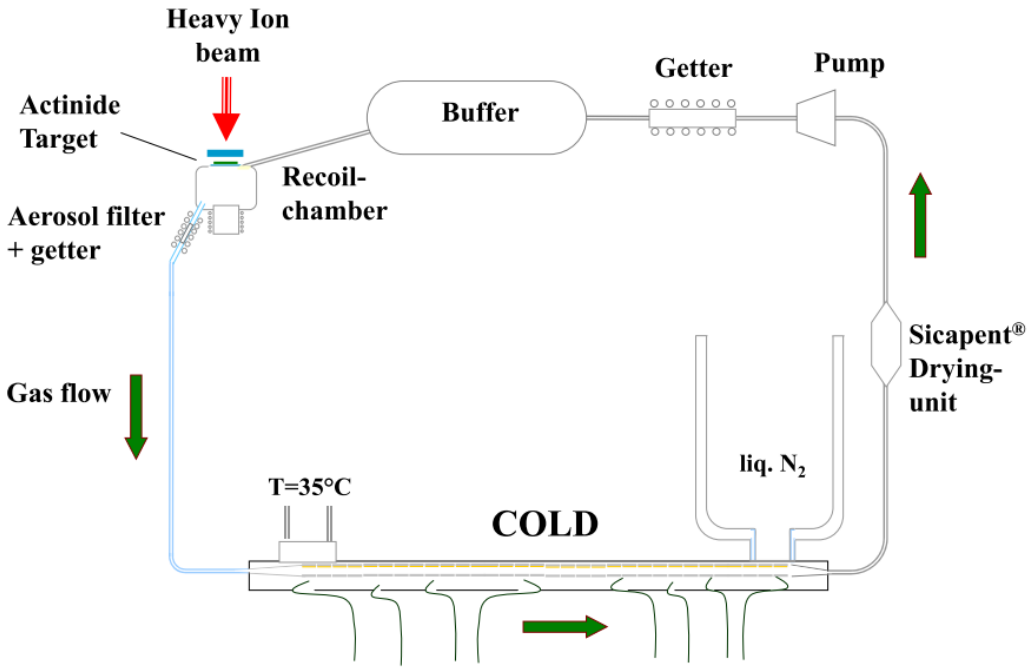

Figure 14: The GC loop for the COLD used in the chemical characterization of Cn. Image from [123].

nally succeeded in chemically characterizing Cn using the COLD setup (Figure 14) [105]. Again, Hg and Rn were produced in parallel by a heavy ion beam on a target admixture. The ^{242}Pu(^{48}Ca,3n)^{287}Fl reaction was used to produce ^{283}Cn indirectly due to increased cross sections, and the possibility to study ^{287}Fl in parallel. Fusion ERs were thermalized in a quartz recoil chamber with an inert noble gas mixture (Ar/He) and the atoms were passed through an aerosol filter over a gold-covered detector array with a temperature gradient to compare their adsorption interactions. Due to trace amounts of water in the experiment, ice was also depositing on the detector where liquid nitrogen was cooling. The experiments established adsorption enthalpies:

$$-\Delta H_{ads}^{Au}(\mathrm{Rn}) = 27 < -\Delta H_{ads}^{Au}(\mathrm{Cn}) = 52 < -\Delta H_{ads}^{Au}(\mathrm{Hg}) = 98 \text{ kJ/mol}.$$

placing Cn somewhere in the middle between the two other elements. It was concluded that while Cn was more inert and volatile than its lighter homolog Hg, it still was not as inert as the

noble gas Rn.

1.3.4 The Case for Chalcogens: Selenium

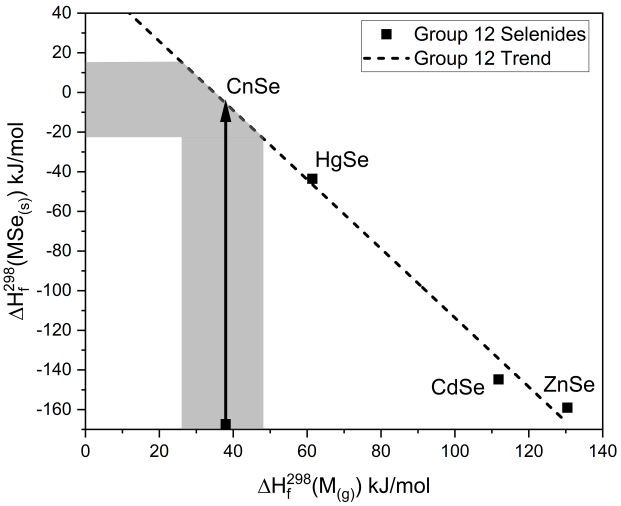

Figure 15: Trends for the group 12 metal (M) selenide (Se) formation, $\Delta H_f^{298}(MSe_{(s)})$, correlated to the respective enthalpy of sublimation for the monatomic gas $\Delta H_f^{298}(M_{(g)})$ at 298 K. Data from [151] except for $\Delta H_f^{298}(\mathrm{Cn}_{(g)})$ from [105]. Shaded area represents uncertainty.

The first chemical interaction of Cn had been established with Au in comparison to its lighter homolog Hg. Researchers were looking for the next step; the source of inspiration was taken from Hg chemistry and its interaction with chalcogens. Oxygen was excluded, as it is unsuitable to serve as a chromatography surface. In nature, Hg is commonly found in the form of cinnabar, HgS [152]. It was therefore decided to repeat the Au comparative experiments using sulfur as a stationary phase [153]. Unfortunately, the chalcogen S is rather complex, forming over 30 different allotropes - more than any other element [154]. Due to allotrope formation, obtaining a uniform, stable chromatography column proved difficult.

Consequently, it was decided to investigate the next homolog of sulfur, namely selenium.

A more detailed account on the chemistry of Se will be given later. Similar to the earlier experiment, the argument was put that if Cn would adsorb to a lesser degree to Se than Hg, its more inert nature would be further confirmed. Furthermore, the possibility of a CnSe bond forming was of interest. Figure 15 depicts the extrapolated formation enthalpy of copernicium selenide.

An empirical correlation between the macroscopic property of an element, the sublimation enthalpy ΔH_{subl} (given as $\Delta H_f^{298}(M_{(g)})$ in Figure 15) and the microscopic property of adsorption on a metallic surface such as gold has been long established [147]. The Eichler-Miedema model used this correlation early on to calculate enthalpies of adsorption for a series of compounds [155–157]. It is therefore possible to experimentally determine the adsorption enthalpy of a SHE on a microscopic single-atom scale and estimate the sublimation enthalpy as a property of the bulk element. Taking the Hg-Se system as an example, the sublimation enthalpy for Hg on the Se surface can be given by [147]:

$$\Delta H_{subl} = \Delta H_{comp} - \Delta H_{ads} \tag{18}$$

Where ΔH_{comp} is the enthalpy of breaking the compound bond and the energy required to promote Hg from the bulk Se to the adsorbed state on the surface.

Therefore, in the given Hg-Se system, ΔH_{comp} can be seen equivalent to the enthalpy of formation of the compound HgSe (or $\Delta H_f^{298}(MSe_{(s)})$ in Figure 15). Using this relation for the gold experiment in 2008, Eichler *et al*. were later able to estimate the $\Delta H_f^{298}(\mathrm{CnSe_{(s)}})$ based on the sublimation enthalpy[7] of Cn, $\Delta H_f^{298}(\mathrm{Cn_{(g)}})$ [105].

While the lighter group 12 metals readily form selenides, the established $\Delta H_f^{298}(\mathrm{Cn_{(g)}})$ suggests that CnSe is less stable than its lighter homologs and could in fact be unstable. For this reason an experimental campaign was launched 2016 with the aim to investigate the Cn-Se interaction, an initiative which was continued in the framework of this work [153].

[7] At the time, sulfur was still chosen as the stationary phase.

1.3.5 Gas Chromatography

The principal investigation method of chemical properties in superheavy elements is currently Gas Chromatography (GC). The principles behind GC are quite similar to liquid-phase chemistry. In this work SHE nuclei are produced in a nuclear fusion evaporation reaction where the recoil products are thermalized and transported to a detector using a carrier gas. Other methods, such as vacuum chromatography for even faster transport times are under development, and have been used for homolog experiments. However, none have yet succeeded in a chemical investigation of a SHE [132, 158]. Compared to the liquid-phase, GC does not require the dissolution in a liquid, so precious time is saved. Due to the long SHE experiment duration of weeks to months, modern GC experiments generally tend to recycle their mobile phase carrier gas in a loop for purity reasons (Figure 14). The SHEs in the mobile phase are transported similar to a classical gas chromatography to a stationary phase. This is a chromatographic surface chosen on the basis of trends from lighter homologs, and the predicted and established properties of the SHE. The repeated adsorption-desorption process between tracers and the stationary phase can reveal the adsorption enthalpy, ΔH_{ads}. As shown in the previous chapter, this value can be related to the macroscopic property of sublimation (or the "volatility") of the bulk material, H_{subl}. Even intangible quantities - as little as one single SHE atom at a time can be detected.

GC can be done in two modes. Isothermal Chromatography (IT) closely resembles classic GC in that a mobile phase (carrier gas) transports ERs to a stationary phase. In SHE chemistry however, Thermochromatography (TC) is often preferred as it enables fast separation of gaseous chemical species [159]. Similar to IT, a tracer is carried by a mobile phase. The main difference lies in a temperature gradient applied over the column with the stationary phase, which allows for one experiment to cover a wide temperature range. Thus, using a TC, the enthalpy of adsorption can be evaluated from as little as only a few atoms in one single experiment [160]. This method is naturally very attractive, as SHE production rates are so low. Tracers deposit within the chromatographic channel thereby resulting in an interal chromatogram (de-

position pattern), which is characteristic for a given element in TC[8]. These narrow deposition patterns result from the vast majority of tracers depositing in a specific region. Due to this narrow pattern, even very few atoms in the same deposited region can indicate the resulting deposition pattern. In the first chemical characterization of Cn, as little as two atoms were used for a first estimation of the adsorption enthalpy on a gold surface [129, 147]. Using the established empirical link between ΔH_{ads} and the volatility of an element, the sublimation enthalpy ΔH_{subl} could then be derived [105, 161].

1.3.6 Adsorption

There are a number of equilibrium isotherm models that have been developed which aim to describe the retention and release of a chromatographic heterogeneous phase at equilibrium. These models include the single layer adsorption Langmuir isotherm model, several of its derivatives seeking to improve on it, adding multi-layer adsorption such as the Freundlich isotherm model[162], or the Flory-Huggins isotherm model [163]. Other noteworthy extensions include the Brunauer-Emmett-Teller isotherm [164], its derivatives the Frenkel-Halsey-Hill isotherm or the McMillan-Teller isotherm which all were established with multi-layer adsorption in mind [165, 166]. The choice of model should be made based on what experimental conditions will be described best by it. For the present work, the Langmuir model was used as a basis, as the assumptions it rests on describe experimental conditions adequately:

I. The column stationary phase is uniform where all adsorption sites are equivalent.

II. tracer-tracer interactions must be discounted.

III. Adsorption is reversible.

IV. The chromatography operates under laminar flow conditions.

[8]Deposition time increases exponentially with 1/T. For more information see Modelling: Monte-Carlo Simulations.

An alteration was made to these assumptions - the adsorbate and adsorbent being Hg and Se, these may be capable of forming stable HgSe, an irreversible process under these conditions. To account for this possibility, adjustments were made to the microscopic Monte-Carlo Simulation (MCS) by Zvára used to describe tracer behaviour in chromatographies. These adjustments will be discussed later in this chapter, and in-depth in Chapter 4.

SHE experiments are performed in open columns with laminar flow at a flow rate of Q (Figure 16). Higher flow speeds cause turbulence, which due to chaotic movement, local changes in flow speed and pressure cannot be controlled adequately to result in reproducible data. The motion of gas as parallel layers (such as under the conditions of laminar flow) allow for diffusion controlled movement of tracers in the carrier.

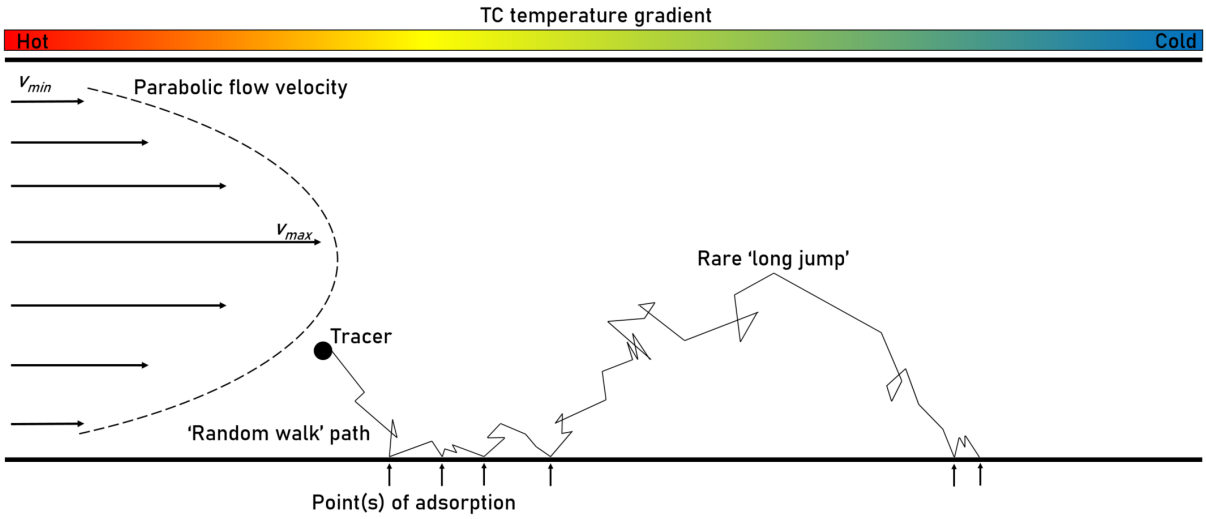

Figure 16: Cross-section of a chromatographic column illustrating the laminar flow of a gas. The gas velocity is fastest at the center of the column (v_{max}) and slows down as one approaches the edges. Tracers follow a diffusion controlled 'random walk' as they travel with the carrier gas, usually with multiple successive adsorptions to the column. 'Long jumps' on a macroscopic scale are rare under these conditions. For TC the temperature gradient is illustrated above.

As the radioactive tracer is transported downstream, it inevitably interacts with the chromatographic surface, adsorbing to it when it comes into contact. This adsorption can be caused

by only a weak van der Waals interaction in which case it is known as *physisorption*. Typical values are in the range of $-\Delta H_{ads} = 20$ kJ/mol [167]. Such an interaction would be typical of the earlier mentioned example, the adsorption of noble gas Rn on Au. The stronger adsorption force is known as $chemisorption$, where a chemical reaction occurs between adsorbate and surface. The threshold between the two modes of adsorption is generally taken to be $-\Delta H_{ads} \approx 50$ kJ/mol, with larger values being attributed to chemisorption. Since the free energy, $\Delta G < 0$ for a spontaneous process, the entropy for a species to adsorb from the gas phase is always $\Delta S < 0$ and

$$\Delta G = \Delta H - T\Delta S \tag{19}$$

the adsorption for a monatomic species is always exothermic. This value therefore represents the strength of the chemical interaction between the tracer and substrate.

Adsorption is generally speaking a reversible process. Depending on the surrounding temperature, the strength of the adsorption bond, as well as intrinsic material properties such as phonon vibrations, the adsorbate can desorb repeatedly in a jump-adsorption-desorption cycle. Near the column surface (known as boundary layer), the flow velocity approaches zero. Due to the slow flow velocity in this region, the tracer is able to reach equilibrium with the stationary phase. Furthermore, here the tracer movement is diffusion-controlled where it will collide with the surface tens to hundreds of times [168]. Multiple random movements can also bring it closer to the center of the column where the tracer will experience a *long jump*; the tracer's longitudinal motion is almost entirely controlled by the carrier gas flow. During the long jump, diffusion only governs lateral motion. These long jumps govern the majority of the movement along the length the column. This process eventually realizes the deposition pattern of the tracer in a column which is specific to the tracer-substrate pair under these conditions (Figure 17). This deposition pattern (known as an internal chromatogram) is usually a fast visualisation of the chemical behaviour of the species tested and gives chemists the ability to quickly and qualitatively compare chromatographic results.

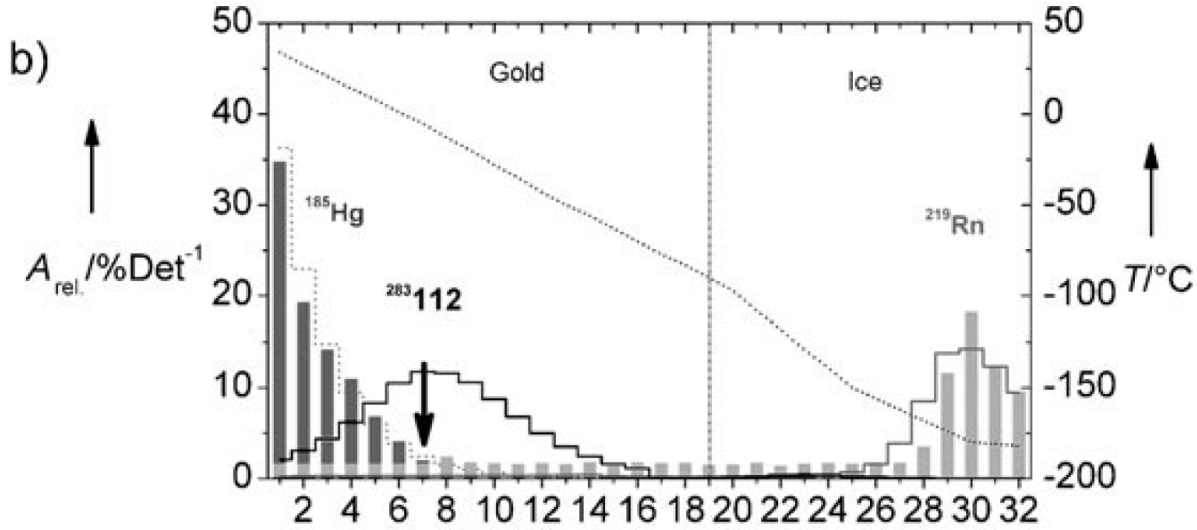

Figure 17: Deposition pattern from the 2008 Cn thermochromatography, image from [105]. Bars represent the deposition yield of nuclides. One can at first glimpse see the separation of Hg (left) on the first section of the Au coated column at higher temperatures from the Rn deposited at the very end of the column ≈ -175°C. The solid line indicates simulated behaviour of Cn, element 112 under these conditions.

Internal chromatograms are characteristic and governed by many experimental parameters such as column shape and dimensions, flow speed, temperature gradient and the carrier gas. A "sharp" peak is generally favoured as it indicates low experimental error and clear results. Peak broadening can occur due to a number factors, and if it is unexpected can point to a number of issues with the experiment, such as a contamination present. Monte-Carlo simulations which have been first developed by Zvára and co-workers, have been used for years to successfully describe these types of experiments [168, 169].

1.3.7 Modelling: Monte-Carlo Simulations

Gas chromatography is a versatile tool to perform chemical separations and to measure volatility properties of a chemical species. These GCs can be modelled using a Monte-Carlo Simulation (MCS). When combining the two methods, and accurately fine-tuning the parameters of

such a MCS, even more possibilities are opened up. Interpretation of results can be enhanced, as well as predicting the effects of changing certain experimental parameters and even predicting the viability of a certain experimental setup in the present context. MCSs work on the principle of describing the behaviour of one single-atom at a time travelling through a chromatographic setup and considering its possible fates. The MCS developed by Zvára in 1985 builds on the Langmuir adsorption model and contains the four assumptions discussed earlier (see Chapter 1.3.6) [169].

These assumptions must hold true for SHE experiments to produce reliable data: Should the tracer be irreversibly bound to the chromatographic surface, i.e. a chemical reaction occurs, ΔH_{ads} is no longer measured exclusively (Figure 18). Surfaces should therefore be chosen appropriately, also considering uniformity. Dimer-, polymerisation and disproportionation reactions are ruled out in one-atom-at-a-time chemistry, simplifying the system to a single-tracer-to-surface interaction. Finally, the flow speed should be appropriately adjusted to minimize transport times, while keeping the Reynolds number below $\approx$ 2000 to ensure laminar conditions [170]. For our experimental setup with the COLD, typical flow speeds are 1.8 - 2.2 L/min.

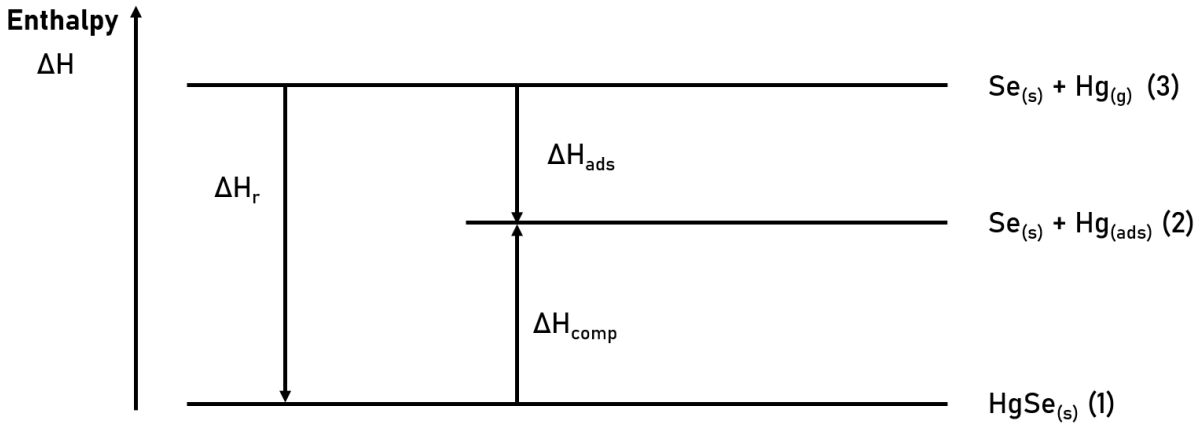

Figure 18: Energy diagram illustrating the mercury selenium system. ΔH_r, the enthalpy of reaction from state (3) to form (1) contains the ΔH_{ads} to adsorb the Hg to the surface, minus the enthalpy ΔH_{comp}, the energy required to break bonds and promote Hg from HgSe to the adsorbed state on the surface.

The MCS begins with a tracer at the entrance to the column, swept along by the carrier gas flow rate. Since tracers are radioactive, they are given a half-life based on the isotope being simulated. For ordinary radioisotopes, the transport time does not affect the experiment significantly, however for SHEs, the half-life is short enough. Tracer diffusion in the carrier gas is taken as Brownian and described using Gilliland's 1934 semi-empirical equation [171–173]:

$$D = 4.3 \cdot 10^{-3} T^{3/2} \frac{(\frac{1}{M_1} + \frac{1}{M_2})^{1/2}}{\frac{P}{P_0}(V_1^{1/3} + V_2^{1/3})^2} \tag{20}$$

where D is the diffusion coefficient (cm^2/s), $M_{1,2}$ is the molar mass of the tracer or carrier respectively (g/mol), $V_{1,2}$ their respective molar volumes (cm^3/mol), T the local temperature (K), P the pressure (Pa) and P_0 the standard pressure (= 101325 Pa). This equation primarily affects the transverse motion through the column. As the flow is laminar (Figure 16), this means the tracer usually will undergo multiple adsorption-desorption cycles at the periphery of the column. Only once it diffuses far enough to the center of the column does the flow speed increase appreciably enough to transport it along a 'long jump'.

As a tracer atom is carried down the column, it will inevitably collide with the stationary phase repeatedly, where it will adsorb. In TC This average time spent in the adsorbed state, t_m, increases exponentially with respect to the decreasing surface temperature (Equation 21)[160, 169]:

$$t_m = \frac{1}{\upsilon_0} e^{\frac{\Delta H_{ads}}{T}} \tag{21}$$

where υ_0 is the lattice phonon frequency of the stationary phase (Hz) and T is the temperature of the stationary phase at the given position (K). In a MCS a randomization factor will assign an actual time adsorbed to the atom based on t_m.

GC normally involves cylindrical columns, simplifying the problem by exploiting the sym-

metry. In cylindrical columns the average length of a long jump d_m (m) of a tracer is given by the Golay equation as [174]:

$$d_m = \frac{\pi r^2 D}{G} + \frac{(11 - 16R_i + 6R_i^2) \cdot G}{48\pi D} \tag{22}$$

where r is the column radius (m), D the diffusion coefficient (m^2/s, see equation 20), G the gas flow volume (m^3/s) and R_i the retention factor given by

$$R_i = \frac{\frac{1}{u}}{\frac{1}{u} + v_i \cdot t_{ads}} \tag{23}$$

where u is the flow velocity (m/s), t_{ads} the mean adsorption time (s) and v_i the mean number of particle collisions per unit length (m^{-1}) given by the Boltzmann velocity related to the gas flow velocity as:

$$v_i = \frac{r}{Q}\sqrt{\frac{2\pi RT}{M}} \tag{24}$$

Where Q is the flow rate (m^3/s), R is the gas constant (= 8.31447 J/mol.K) and M the molar mass of the tracer (g/mol).

Due to technical limitations however, the chemistry experiments involving Cn use a square channel of PIN diodes, forming a rectangular channel with dimensions a by b (m). For rectangular channels, the above equations are slightly modified based on studies performed by Poppe which describe the system well [175]. The modifications are dependent on the dimensions of the chromatographic channel. In this case, the mean distance of the tracer d_m in a channel with dimensions 1.2 by 8.3 mm as in the COLD is given by:

$$d_m = \frac{2Dab}{G} + \frac{(6.867 + 20.79R_i + 31.43R_i^2) \cdot G \cdot a}{105(1 + R_i)^2 \cdot D \cdot b} \tag{25}$$

The square channel affects the gas velocity u, and R_i being dependent on u, this affects equation 25.

Until now, the core MCS based on Zvára's model as used by chemists in this field has been discussed. This work expanded on the core by including reaction kinetics based on both, the Arrhenius and Eyring-Polanyi equation respectively, and fitting experimental data to determine the energetics of the Hg-Se reaction. For the approach using the Arrhenius equation, the well-known

$$k = A \cdot e^{\frac{-E_a}{RT}} \tag{26}$$

was used to determine the Arrhenius activation energy, E_a, where k is the rate constant of the reaction and A is the pre-exponential factor [176]. A ($\leq 10^{10}$ for bimolecular reactions) and E_a were iterated to determine a reaction rate. This rate was used to generate a reaction time (see random parameters below) to be compared with the adsorption time t_{ads} for each collision with the surface. Tracers which reacted before they could desorb again were considered as irreversibly bound in a chemical bond and the resulting deposition pattern was used to find a minimum deviation from the experimental data with a χ^2-test.

The same approach was used with the Eyring-Polanyi equation [176]:

$$k = \kappa \frac{k_b T}{h} \cdot e^{\frac{-\Delta G^{\ddagger}}{RT}} \tag{27}$$

where k represents the rate constant of the reaction, k_b is the Boltzmann constant, h the Planck constant, and $\Delta G^{\ddagger}$ is the Gibbs free energy of activation for the reaction. κ is the Eyring transmission coefficient and represents the probability of a successful forward reaction to occur for the transition state. It is generally taken to be 1 or within $\approx 10\%$ of one [176].

The calculations so far give average values for the parameters d_m and v_i in the simulation. To reflect the more realistic microscopic behaviour of tracers however, the MCS uses the equations

to generate random values for each tracer for the given parameters, based on a logarithmic distribution:

$$\text{The lifetime of the tracer: } t_{lt} = -\frac{t_{1/2}}{ln(2)} \cdot log(x) \tag{28}$$

$$\text{The actual distance travelled: } d = -d_m \cdot log(x) \tag{29}$$

$$\text{The number of adsorptions: } N_a = -v_i \cdot log(x) \tag{30}$$

$$\text{The reaction time: } t_{reac} = -\frac{1}{k} \cdot log(x) \tag{31}$$

where x represents a randomly drawn number between 0 and 1.

The advantage of the core MCS is that it can be adapted and modified for a wide range of applications. In the case of SHEs the lifetime t_{lt} of atoms for instance is so short, that in-flight decay of atoms becomes a significant issue, meaning that an element decaying before it had the chance to exit the chromatographic column can still be simulated. For the 2016 investigation of the Cn and Fl interaction with thin selenium surfaces, the MCS was functionalized with a composite chromatographic surface simulation, which could model multiple surface properties in parallel [153]. These simulations once fine-tuned to reliably reproduce experimental data, allow the user to iterate step-wise the ΔH_{ads} in order to find the best fit describing the deposition pattern, detect causes of unusual behaviour in new experimental setups, or even avoid these in the first place. A simplified program flowchart of the MCS is shown in figure 19.

In this work, the basic MCS was used to describe isothermal- and thermochromatographies in chapters 3 and 5. A modified MCS was used in chapter 4 designed to minimize errors to experimental results with the task of determining the activation energy of the reaction between Hg and Se.

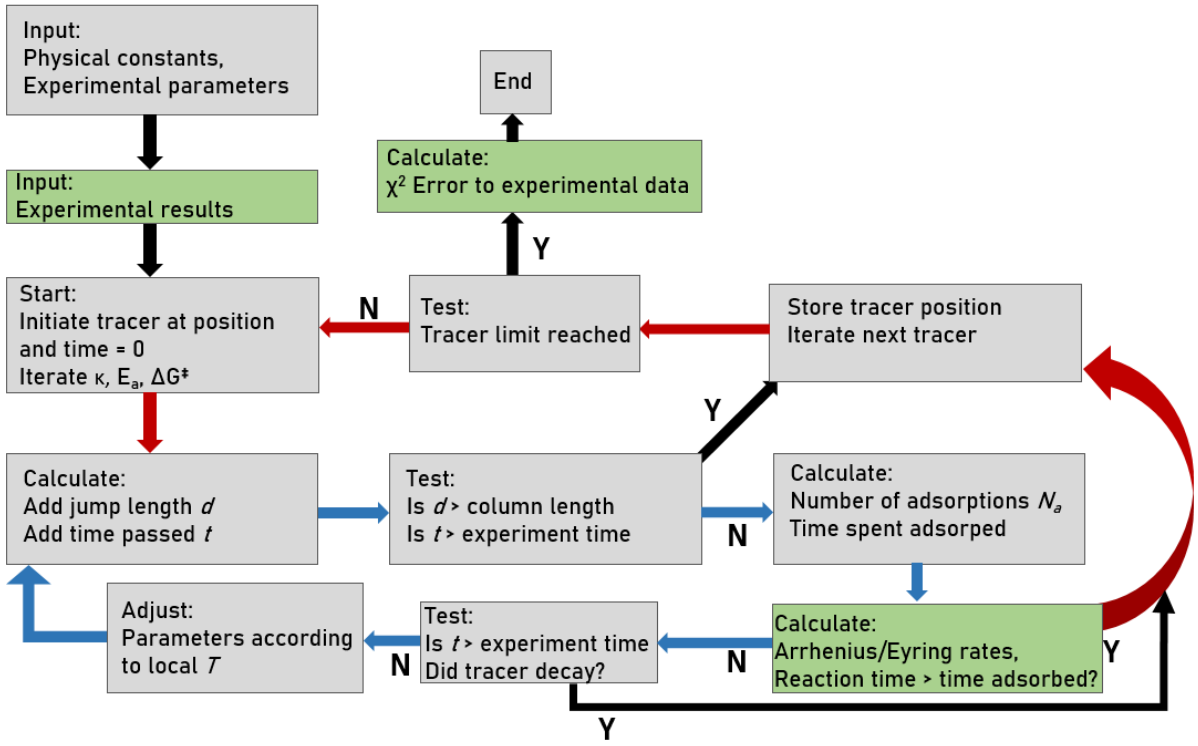

Figure 19: Simplified program flowchart of the MCS used to describe a TC. Grey boxes represent the core program used, green boxes are additions in this work. The initial experiment parameters are put into the system, allowing the program to simulate one atom at a time progressing through the column. The loop experienced by an individual tracer is represented by blue arrows. The loop iterating parameters to fit experimental data is given by red arrows. Various conditions are set to end the particle loop such as decaying in-flight, reacting with the surface or exiting the column thus triggering the next iteration of tracer.

1.4 Selenium Chemistry

As has been discussed, Se plays an important role in expanding on the chemistry of Cn. Selenium was first discovered in 1818 by the Swedish chemist Berzelius as a by-product of the sulfuric acid manufacturing process [177, 178]. It was soon identified as a chalcogen; Chalcogens are commonly found in the -2 oxidation state and have the tendency to form allotropes. As such, Se itself exhibits complex allotropic behaviour. Because of this there was longstanding uncertainty about its different states [179]. Even today naming Se allotropes by their appearance, red, grey or black, as is often colloquially done, can be the cause of misunderstandings [180]. An illustration of the key states and allotropes of Se can be seen in figure 20.

The first Cn experiments conducted with Se were based on the reactivity of amorphous *a*-Se towards Hg. In a GC setting, Hg passing over an a-Se surface will spontaneously react and adsorb irreversibly to the surface [181]. The argument was, that if Cn exhibited less reactivity, or the CnSe bond was unstable (Figure 15), then there should be a distinct difference in the observable GC deposition patterns.

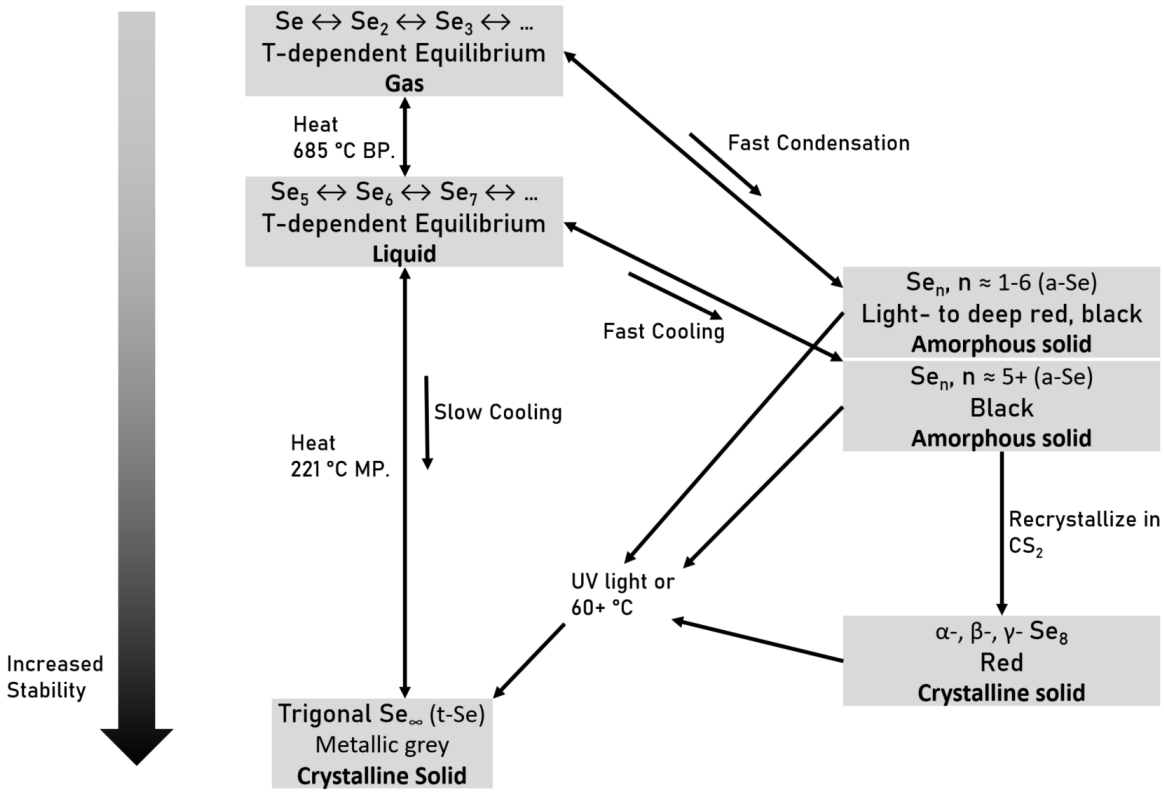

Figure 20: The common states of Selenium and its allotropes, with increasing stability towards the bottom. The most thermodynamically stable state at STP is known as trigonal 'grey' selenium (t-Se) and has a grey metallic sheen. Both allotropes, the red crystalline states ($\alpha-, \beta-, \gamma-$ Se) and amorphous (a-Se) selenium will over time change to t-Se, however this process is vastly catalyzed using UV light or temperatures above $\approx 60°$C. Rhombohedric Se_6 has been omitted for simplicity.

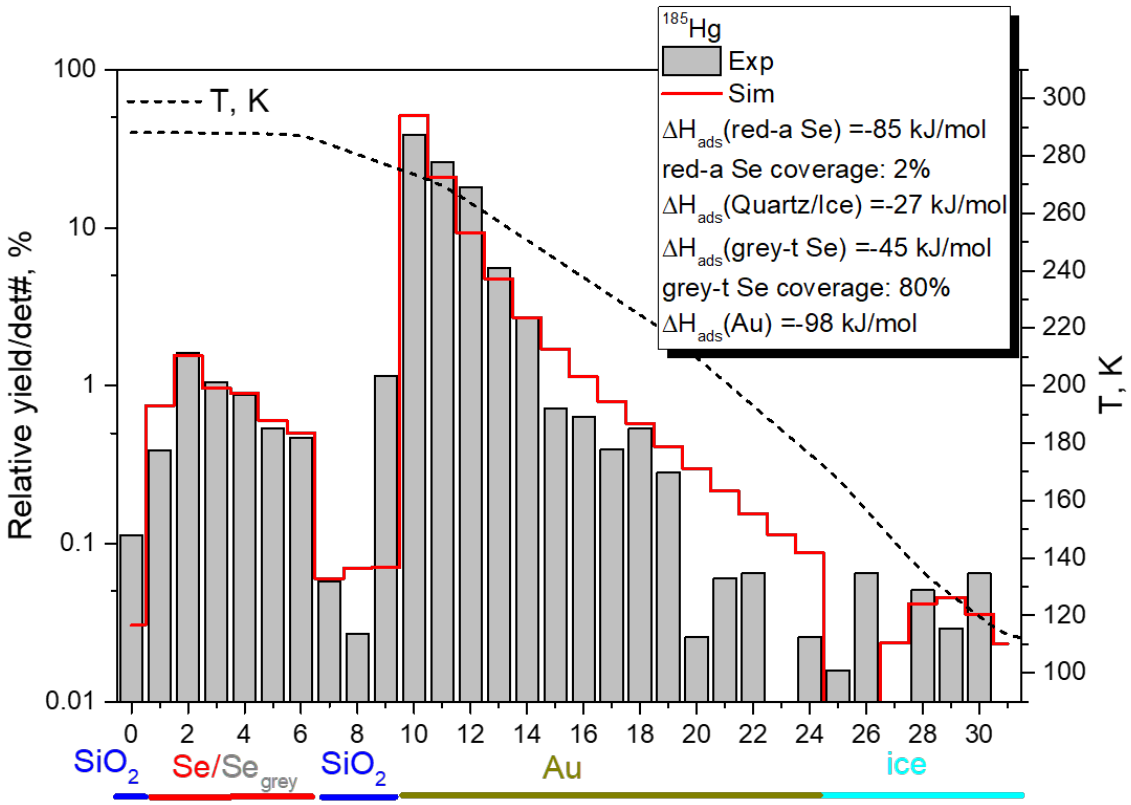

Figure 21: The relative chromatographic yield of ^{283}Cn and $^{183-185}$Hg in the COLD during the 2016 experimental campaign. Red line represents a MCS of the experimental conditions, dotted line shows the negative temperature gradient. The $^{183-185}$Hg deposition pattern shows a low affinity for the beginning of the GC column with red-grey Se coating, while it deposited diffusion controlled on the Au PINs. Contrary to expectation, all two ^{283}Cn events were detected on the Se surface. Graph adapted from [182].

During that campaign, two significant decays were attributed to ^{283}Cn, both which deposited on the Se surface (Figure 21). While this was a good first approximation for the chemical interaction between Cn and Se, there were also some complications [153]. Firstly, the experiment was designed with an *a*-Se stationary surface. Since this allotrope will spontaneously change into the more stable *t*-Se over time, and typical experimental campaigns are of several week duration, there was some ambiguity about the identity of the surface. Hg radioisotopes were being produced in parallel for the 4 week duration of the experiment as a tracer monitoring the surface. However, due to the potential of the surface to gradually change, a great uncertainty arose about the nature of the chemical interaction. Additionally, two decay chains of ^{283}Cn were a great achievement, however statistically still not significant enough to unambiguously prove a Cn-Se interaction.

This thesis commences from the lessons learnt in previous campaigns and the experimental setup was designed to address the issue of the ambiguous *a*-Se surface in order to simplify the problem. The chromatographic surface was therefore chosen to be *t*-Se which was used in the current investigations. Chapter 2 deals with the development and classification of selenium as a chromatographic surface. The optimized *t*-Se surface was then used in an off-line model experiment with Hg in Chapter 3, to explore the reaction kinetics of these two elements. Chapter 4 shows the application of the selenium stationary phase in an on-line experiment with copernicium, and a first indication of a reaction of copernicium is presented. Finally, Chapter 5 presents a method to closely investigate and improve on the complications encountered during the on-line experiment in Chapter 4.

References

1. Hofmann, S. *et al.* On the discovery of new elements (IUPAC/IUPAP Report). *Pure and Applied Chemistry* **92,** 1387–1446. ISSN: 0033-4545 (2020).
2. Mendeleev, D. Ueber die Beziehungen der Eigenschaften zu den Atomgewichten der Elemente. *Zeitschrift für Chemie,* 405–406 (1869).

3. Newland, J. A. R. On the Law of Octaves. *Chemical News* **12,** 83 (1865).

4. Meyer, L. *Die Modernen Theorien der Chemie und Ihre Bedeutung für die Statistik* 2nd, 319–323. ISBN: 3663537137 (Maruschke und Berendt, Breslau, 1872).

5. Mendeleev, D. Die Periodische Gesetzmaessigkeit der Chemischen Elemente. *Annalen der Chemie ud Pharmacie* **8,** 133–229 (1871).

6. Weeks, M. E. The discovery of the elements. XV. some elements predicted by mendeleeff. *Journal of Chemical Education* **9,** 1606–1619. ISSN: 00219584 (1932).

7. Moseley, H. XCIII. The high-frequency spectra of the elements. *The London, Edinburgh, and Dublin Philosophical Magazine and Journal of Science* **26,** 1024–1034. ISSN: 1941-5982 (1913).

8. Moseley, H. LXXX. The high-frequency spectra of the elements. Part II. *The London, Edinburgh, and Dublin Philosophical Magazine and Journal of Science* **27,** 703–713. ISSN: 1941-5982 (1914).

9. Rutherford, E. Nuclear Constitution of Atoms. *Nature* **105,** 500–501 (1920).

10. Perrier, C. & Segré, E. Some chemical properties of element 43. *The Journal of Chemical Physics* **5,** 717–720. ISSN: 00219606 (1937).

11. Perrier, C. & Segrè, E. Technetium: The element of atomic number 43. *Nature* **159,** 24. ISSN: 00280836 (1947).

12. Yoshihara, H. K. Discovery of a new element 'nipponium': Re-evaluation of pioneering works of Masataka Ogawa and his son Eijiro Ogawa. *Spectrochimica Acta - Part B Atomic Spectroscopy* **59,** 1305–1310. ISSN: 05848547 (2004).

13. Becquerel, H. Sur les radiations émises par phorphorescence. *Comptes rendus hebdomadaires des séances de l'Académie des Sciences* **122,** 420–421 (1896).

14. Becquerel, H. Sur les radiations invisibles émises par les corps phosphorescents. *Comptes rendus hebdomadaires des séances de l'Académie des Sciences* **122,** 501–503 (1896).

15. Seaborg, G. T. & Segre, E. The Trans-Uranium Elements. *Nature,* 863–865 (1947).

16. Seaborg, G. T. The man-made chemical elements beyond uranium. *Physics Today* **15,** 19–30. ISSN: 19450699 (1962).

17. Seaborg, G. T. The Periodic Table Tortuous Path to Man-Made Elements. *Chemical and Engineering News* **57,** 46–52 (1979).

18. Fermi, E. Possible production of elements of atomic number higher than 92. *Nature* **133,** 898–899. ISSN: 00280836 (1934).

19. McMillan, E. & Abelson, P. H. Radioactive element 93. *Physical Review* **57,** 1185–1186. ISSN: 0031899X (1940).

20. Seaborg, G. T. *Lawrence Berkeley Laboratory* in *Lawrence Livermore Laboratory National Laboratory Conference* (1981).

21. AB, N. P. O. *Nobel Prize in Chemistry* `https://www.nobelprize.org/prizes/chemistry/1951/summary/` (2021).

22. Zagrabaev, V., Karpov, A. & Greiner, W. Future of superheavy element research : Which nuclei could be synthesized within the next few years ? *Journal of Physics: Conference Series* **420,** 1–15 (2013).

23. Runcorn, S. K. On the possible existence of superheavy elements in the primeval Moon. *Earth and Planetary Science Letters* **39,** 193–198. ISSN: 0012821X (1978).

24. Dmitriev, S. N. *et al.* Search for the Spontaneously Fissioning Nuclide in Cheleken Hot Brines. *JINR Rapid Communications* **5,** 13–20 (1988).

25. Ter-Akopian, G. M. & Dmitriev, S. N. Searches for superheavy elements in nature: Cosmic-ray nuclei; spontaneous fission. *Nuclear Physics A* **944,** 177–189. ISSN: 03759474 (2015).

26. Köber, E. & Langrock, E. J. Search for Superheavy Elements in the Nature. *Isotopenpraxis Isotopes in Environmental and Health Studies* **26,** 576–583. ISSN: 0021-1915 (1990).

27. Thornton, B. F. & Burdette, S. C. Neutron stardust and the elements of Earth. *Nature Chemistry* **11,** 4–10. ISSN: 17554349. http://dx.doi.org/10.1038/s41557-018-0190-9 (2019).

28. Ogg, J. G., Ogg, G. M. & Gradstein, F. M. *A Concise Geologic Time Scale* 1st, 10 (Elsevier, Amsterdam, 2016).

29. IUPAC. *IUPAC Periodic Table of the Elements* 2018. https://iupac.org/what-we-do/periodic-table-of-elements/ (2021).

30. Smits, O. R., Mewes, J. M., Jerabek, P. & Schwerdtfeger, P. Oganesson: A Noble Gas Element That Is Neither Noble Nor a Gas. *Angewandte Chemie - International Edition* **59,** 23636–23640. ISSN: 15213773 (2020).

31. Pitzer, K. S. Are elements 112, 114, and 118 relatively inert gases? *The Journal of Chemical Physics* **63,** 1032–1033. ISSN: 00219606 (1975).

32. Pyykko, P. & Desclaux, J. P. Relativity and the Periodic System of Elements. *Accounts of Chemical Research* **12,** 276–281. ISSN: 15204898 (1979).

33. Norrby, L. J. Why is mercury liquid? Or, why do relativistic effects not get into chemistry textbooks? *Journal of Chemical Education* **68,** 110. http://pubs.acs.org/doi/abs/10.1021/ed068p110 (1991).

34. Jansen, M. Effects of relativistic motion of electrons on the chemistry of gold and platinum. *Solid State Sciences* **7,** 1464–1474. ISSN: 12932558 (2005).

35. Hammer, B. & Norskov, J. Why gold is the noblest of all the metals. *Nature* **376,** 238–240 (1995).

36. Mewes, J. M., Smits, O. R., Kresse, G. & Schwerdtfeger, P. Copernicium: A Relativistic Noble Liquid. *Angewandte Chemie - International Edition* **58,** 17964–17968. ISSN: 15213773 (2019).

37. Calvo, F., Pahl, E., Wormit, M. & Schwerdtfeger, P. Evidence for low-temperature melting of mercury owing to relativity. *Angewandte Chemie - International Edition* **52,** 7583–7585. ISSN: 14337851 (2013).

38. Schwerdtfeger, P., Pašteka, L. F., Punnett, A. & Bowman, P. O. Relativistic and quantum electrodynamic effects in superheavy elements. *Nuclear Physics A* **944,** 551–577. ISSN: 03759474. http://dx.doi.org/10.1016/j.nuclphysa.2015.02.005 (2015).

39. Schädel, M. *Chemistry of superheavy elements* 2nd (eds Schädel, M. & Saughnessy, D.) 2. ISBN: 9783642374654 (Springer, Berlin, Heidelberg, 2014).

40. Oganessian, Y. T. *et al.* Synthesis of a new element with atomic number Z=117. *Physical Review Letters* **104,** 1–4. ISSN: 00319007 (2010).

41. Kragh, H. The search for superheavy elements: Historical and philosophical perspectives, 1–46. arXiv: 1708.04064. http://arxiv.org/abs/1708.04064 (2017).

42. Wapstra, A. H. Criteria that must be satisfied for the discovery of a new chemical element to be recognized. *Pure and Applied Chemistry* **63,** 879–886. ISSN: 0033-4545 (1991).

43. IUPAC & IUPAP. Criteria that must be satisfied for the discovery of a new chemical element to be recognized: DISCOVERY OF THE TRANSFERMIUM ELEMENTS. **65,** 1757–1814 (1993).

44. Soti, Z., Magill, J., Pfennig, G. & Derher, R. Karlsruhe nuclide chart - new 9. edition 2015. https://www.osti.gov/biblio/22531290 (July 2015).

45. Aston, F. W. Atoms and their packing fractions. *Nature* **120,** 956–959. ISSN: 00280836 (1927).

46. Strum, L. Massendefekt und charakteristische Kerngrößen. *Zeitschrift für Physik* **50,** 555–558. ISSN: 14346001 (1928).

47. Einstein, A. Ist die Trägheit eines Körpers von seinem Energieinhalt abhängig? *Annalen der Physik* **323,** 639–641 (1905).

48. Bethe, H. A. Nuclear Processes as Many-Body Problems. *Reviews of Modern Physics* **9,** 69–244. ISSN: 00346861 (1937).

49. Weizsäcker, C. F. Zur Theorie der Kernmassen. *Zeitschrift für Physik* **96,** 431–458. ISSN: 14346001 (1935).

50. Gamow, G. Mass defect curve and nuclear constitution. *Proceedings of the Royal Society of London. Series A, Containing Papers of a Mathematical and Physical Character* **126,** 632–644. ISSN: 0950-1207 (1930).

51. Myers, W. D. & Swiatecki, W. J. Nuclear masses and deformations. *Nuclear Physics* **81,** 1–60. ISSN: 00295582 (1966).

52. Choppin, G., Liljenzin, J.-O. & Rydberg, J. *Radiochemistry and Nuclear Chemistry* 3rd ed., 42. ISBN: 9788578110796. arXiv: arXiv : 1011 . 1669v3 (Academic Press, Göteborg, Sweden, 2001).

53. Möller, P. The limits of the nuclear chart set by fission and alpha decay. *EPJ Web of Conferences* **131.** ISSN: 2100014X (2016).

54. Mayer, M. G. On closed shells in nuclei. *Physical Review* **74,** 235–239. ISSN: 0031899X (1948).

55. Haxel, O., Jensen, J. H. D. & Suess, H. E. On the "magic numbers" in nuclear structure. *Physical Review* **75,** 1766. ISSN: 0031899X (1949).

56. *The Nobel Prize in Physics 1963* 2021. https : //www . nobelprize . org/prizes/physics/1963/summary/ (2021).

57. Zagrebaev, V. & Greiner, W. Synthesis of superheavy nuclei: A search for new production reactions. *Physical Review C - Nuclear Physics* **78,** 1–11. ISSN: 1089490X (2008).

58. Oganessian, Y. Nuclei in the "island of stability" of superheavy elements. *Journal of Physics: Conference Series* **337.** ISSN: 17426596 (2012).

59. Meldner, H. Predictions of New Magic Regions and Masses for Super Heavy Nuclei from Calculations with Realistic Shell Model Single Particle Hamiltonians. *Ark. Fys.* **36,** 593–598 (1966).

60. Sobiczewski, A., Gareev, F. A. & Kalinkin, B. N. Closed Shells for Z > 82 and N > 126 in a Diffuse Potential Well. *Physics Letters* **22,** 500–502 (1966).

61. Grumann, J., Mosel, U., Fink, B. & Greiner, W. On the stability of superheavy nuclei around Z = 114 and Z = 164. *Zeitschrift für Physik* **228,** 371–386. ISSN: 14346001 (1969).

62. Grumann, J., Mosel, U., Fink, B. & Greiner, W. On the stability of superheavy nuclei around Z = 114 and Z = 164. *Zeitschrift für Physik* **228,** 371–386. ISSN: 14346001 (1969).

63. Türler, A. The expansion of the periodic table to its natural limits. *Chimia* **73,** 173–178. ISSN: 00094293 (2019).

64. Randrup, J., Larsson, S. E., Möller, P., Sobiczewski, A. & Lukasaik, A. Theoretical estimates of spontaneous-fission half-lives for superheavy elements based on the modified-oscillator model. *Physica Scripta* **10,** 60–64. ISSN: 14024896 (1974).

65. Ćwiok, S., Nazarewicz, W. & Heenen, P. H. Structure of odd-n superheavy elements. *Physical Review Letters* **83,** 1108–1111. ISSN: 10797114 (1999).

66. Sobiczewski, A., Muntian, I. & Patyk, Z. Problem of "deformed" superheavy nuclei. *Physical Review C - Nuclear Physics* **63,** 343061–3430612. ISSN: 1089490X (2001).

67. Choppin, G., Liljenzin, J.-O. & Rydberg, J. *Radiochemistry and Nuclear Chemistry* 3rd ed., 374–376. ISBN: 9788578110796. arXiv: arXiv : 1011 . 1669v3 (Academic Press, Göteborg, Sweden, 2001).

68. Schädel, M. & Shaughnessy, D. A. *Chemistry of the superheavy elements* 2nd, 1–81 (2015).

69. Zagrebaev, V. I. & Greiner, W. Cross sections for the production of superheavy nuclei. *Nuclear Physics A* **944,** 257–307. ISSN: 03759474. http://dx.doi.org/10.1016/j.nuclphysa.2015.02.010 (2014).

70. Zagrebaev, V. Fusion-fission dynamics of super-heavy element formation and decay. *Nuclear Physics A* **734,** 164–167. ISSN: 03759474 (2004).

71. Loveland, W. D., Morrissey, D. J. & Seaborg, G. T. in *Modern Nuclear Chemistry* 2nd, 247–303 (John Wiley and Sons, New Jersey, 2006). ISBN: 9780471115328.

72. Kratz, J. V. The Search for Superheavy Elements. *Radiochimica Acta* **32,** 25–41. ISSN: 05562813 (1983).

73. Türler, A. & Pershina, V. Advances in the production and chemistry of the heaviest elements. *Chemical Reviews* **113,** 1237–1312. ISSN: 00092665 (2013).

74. Siwek-Wilczyńska, K., Cap, T. & Kowal, M. Exploring the production of new superheavy nuclei with proton and α -particle evaporation channels. *Physical Review C* **99,** 2–7. ISSN: 24699993 (2019).

75. Lopez-Martens, A. *et al.* Measurement of proton-evaporation rates in fusion reactions leading to transfermium nuclei. *Physics Letters, Section B: Nuclear, Elementary Particle and High-Energy Physics* **795,** 271–276. ISSN: 03702693. https://doi.org/10.1016/j.physletb.2019.06.010 (2019).

76. Lützenkirchen, K. *et al.* Angular distributions in quasi-fission reactions: Evidence for incomplete relaxation of the tilting mode. *Zeitschrift für Physik A Atoms and Nuclei* **320,** 529–530. ISSN: 03402193 (1985).

77. Back, B. B. Complete Fusion and Quasifission in Reactions between Heavy Ions. *Physical Review C* **31,** 2104–2112 (1985).

78. Kaji, D., Morimoto, K., Sato, N., Yoneda, A. & Morita, K. Gas-filled recoil ion separator GARIS-II. *Nuclear Instruments and Methods in Physics Research, Section B: Beam Interactions with Materials and Atoms* **317,** 311–314. ISSN: 0168583X. http://dx.doi.org/10.1016/j.nimb.2013.05.085 (2013).

79. Semchenkov, A. *et al.* The TransActinide Separator and Chemistry Apparatus (TASCA) at GSI - Optimization of ion-optical structures and magnet designs. *Nuclear Instruments and Methods in Physics Research, Section B: Beam Interactions with Materials and Atoms* **266,** 4153–4161. ISSN: 0168583X (2008).

80. Davids, C. N. Recoil separators. *Nuclear Instruments and Methods in Physics Research, Section B: Beam Interactions with Materials and Atoms* **204,** 124–128. ISSN: 0168583X (2003).

81. Kurth, F., Froemel, J., Tanaka, S., Esashi, M. & Gessner, T. *Electroplating of neodymium iron alloys* in *2016 IEEE 11th Annual International Conference on Nano/Micro Engineered and Molecular Systems, NEMS 2016* (IEEE, 2016), 405–408. ISBN: 9781509019472.

82. Meyer, C. C. *Ion-Beam Induced Structural and Chemical Changes in Targets used for Superheavy Element Production* in *TASCA Workshop* (Darmstadt, 2021).

83. Marx, D. *et al.* A Rotating Target Wheel with Thin Targets for Heavy Ion Beams of High Current Densities. *Nuclear Instruments and Methods* **163,** 15–20 (1979).

84. Nitschke, J. M. A high intensity heavy-ion recoil-target system. *Nuclear Instruments and Methods* **138,** 393–406. ISSN: 0029554X (1976).

85. Greene, J. P., Heinz, A., Falout, J. & Janssens, R. V. Rotating target wheel system for super-heavy element production at ATLAS. *Nuclear Instruments and Methods in Physics Research, Section A: Accelerators, Spectrometers, Detectors and Associated Equipment* **521,** 214–221. ISSN: 01689002 (2004).

86. Jäger, E. *et al.* High intensity target wheel at TASCA: Target wheel control system and target monitoring. *Journal of Radioanalytical and Nuclear Chemistry* **299,** 1073–1079. ISSN: 02365731 (2014).

87. Yaffe, L. Preparation of thin Films, Sources, and Targets. *Annual Review of Nuclear Science* **12,** 153–188. ISSN: 0066-4243 (1962).

88. Aumann, D. C. & Müllen, G. Preparation of targets of Ca, Ba, Fe, La, Pb, Tl, Bi, Th and U by electrodeposition from organic solutions. *Nuclear Instruments and Methods* **115,** 75–81. ISSN: 0029554X (1974).

89. Müllen, G. & Aumann, D. C. Preparation of targets of Np, Pu, Am, Cm and Cf by electrodeposition from organic solutions. *Nuclear Instruments and Methods* **128,** 425–428. ISSN: 0029554X (1975).

90. Hofmann, S. *et al.* The new element 112. *Zeitschrift für Physik A Hadrons and Nuclei* **354,** 229–230. ISSN: 0939-7922 (1996).

91. Kaji, D. *et al.* Decay measurement of 283Cn produced in the 238U(48Ca,3n) reaction using GARIS-II. *Nuclear Physics* **51,** 2018 (2018).

92. Ellison, P. A. *et al.* New superheavy element isotopes: Pu242(Ca48,5n)114-285. *Physical Review Letters* **105,** 27–30. ISSN: 00319007 (2010).

93. Hong, J., Adamian, G. G. & Antonenko, N. V. Ways to produce new superheavy isotopes with Z = 111–117 in charged particle evaporation channels. *Physics Letters, Section B: Nuclear, Elementary Particle and High-Energy Physics* **764,** 42–48. ISSN: 03702693. http://dx.doi.org/10.1016/j.physletb.2016.11.002 (2017).

94. Oganessian, Y. T. & Utyonkov, V. K. Superheavy nuclei from 48Ca-induced reactions. *Nuclear Physics A* **944,** 62–98. ISSN: 03759474. http://dx.doi.org/10.1016/j.nuclphysa.2015.07.003 (2015).

95. Oganessian, Y. *et al.* Synthesis of superheavy nuclei in the 48Ca+244Pu reaction: 288-114. *Physical Review C* **62,** 041604. ISSN: 0556-2813. http://prc.aps.org/abstract/PRC/v62/i4/e041604%5Cnhttp://link.aps.org/doi/10.1103/PhysRevC.62.041604 (2000).

96. Hong, J., Adamian, G. G., Antonenko, N. V., Jachimowicz, P. & Kowal, M. Rate of decline of the production cross section of superheavy nuclei with Z=114-117 at high excitation energies. *Physical Review C* **103,** 14–16. ISSN: 24699993 (2021).

97. Alexander, E. C. J., Lewis, R. S., Reynolds, J. H. & Michel, M. C. Plutonium-244: Confirmation as an Extinct Radioactivity. *Science,* 837–840 (1972).

98. Turner, G., Harrison, T. M., Holland, G., Mojzsis, S. J. & Gilmour, J. Extinct 244Pu in ancient zircons. *Science* **306,** 89–91. ISSN: 00368075 (2004).

99. Armstrong, C. R., Brant, H. A., Nuessle, P. R., Hall, G. & Cadieux, J. R. Anthropogenic plutonium-244 in the environment: Insights into plutonium's longest-lived isotope. *Scientific Reports* **6,** 1–8. ISSN: 20452322 (2016).

100. Lumetta, G. J., Thompson, M. C., Penneman, R. A. & Eller, P. G. in *The Chemistry of the Actinide and Transactinide Elements* 1397–1443 (Springer, Dordrecht, 2007).

101. Oganessian, Y. T. *et al.* Measurements of cross sections and decay properties of the isotopes of elements 112, 114, and 116 produced in the fusion reactions233,238U, 242Pu, and248Cm+48Ca. *Physical Review C - Nuclear Physics* **70,** 3–5. ISSN: 1089490X (2004).

102. Stoyer, M. A. *et al. Estimating Super Heavy Element Event Random Probabilities Using Monte Carlo Methods* in *The 4th International Conference on the Chemistry and Physics of the Transactinide Elements* (Sochi, 2011).

103. Oganessian, Y. T. & Utyonkov, V. K. Super-heavy element research. *Reports on Progress in Physics* **78,** 36301. ISSN: 00344885. http://dx.doi.org/10.1088/0034-4885/78/3/036301 (2015).

104. Schädel, M. Superheavy Element Chemistry - Achievements and Perspectives. *Journal of Nuclear and Radiochemical Sciences* **8,** 47–53. ISSN: 14346060 (2007).

105. Eichler, R. *et al.* Thermochemical and physical properties of element 112. *Angewandte Chemie - International Edition* **47,** 3262–3266. ISSN: 14337851 (2008).

106. Haba, H. *et al.* Development of Gas-jet Transport System Coupled to the RIKEN Gas-filled Recoil Ion Separator GARIS for Superheavy Element Chemistry. *Journal of Nuclear and Radiochemical Sciences* **8,** 55–58. ISSN: 1345-4749 (2007).

107. Subotic, K. *et al.* Evaporation residue collection efficiencies and position spectra of the Dubna gas-filled recoil separator. *Nuclear Instruments and Methods in Physics Research, Section A: Accelerators, Spectrometers, Detectors and Associated Equipment* **481,** 71–80. ISSN: 01689002 (2002).

108. Wittwer, D. *et al.* Gas phase chemical studies of superheavy elements using the Dubna gas-filled recoil separator - Stopping range determination. *Nuclear Instruments and Methods in Physics Research, Section B: Beam Interactions with Materials and Atoms* **268,** 28–35. ISSN: 0168583X. http://dx.doi.org/10.1016/j.nimb.2009.09.062 (2010).

109. Popeko, A. G. On-line separators for the Dubna Superheavy Element Factory. *Nuclear Instruments and Methods in Physics Research, Section B: Beam Interactions with Ma-*

terials and Atoms **376,** 144–149. ISSN: 0168583X. http://dx.doi.org/10.1016/j.nimb.2016.02.025 (2016).

110. Münzenberg, G. Ein geschwindigkeitsfilter für die analyse von schwerionen-reaktionsprodukten. *International Journal of Mass Spectrometry and Ion Physics* **14,** 363–387. ISSN: 00207381 (1974).

111. Schädel, M. & Shaughnessy, D. A. *Chemistry of the superheavy elements* 2nd, 309–374 (2015).

112. Schädel, M. *et al.* First aqueous chemistry with seaborgium (element 106). *Radiochimica Acta* **77,** 149–159. ISSN: 00338230 (1997).

113. Hulet, E. K. *et al.* Chloride complexation of element 104. *Journal of Inorganic and Nuclear Chemistry* **42,** 79–82. ISSN: 00221902 (1980).

114. Gober, M. K. *et al.* Chemical Properties of Element 105 in Aqueous Solution: Extractions into Diisobutylcarbinol. *Radiochimica Acta* **57,** 77–84. ISSN: 21933405 (1992).

115. Szeglowski, Z. *et al.* Investigation of elements 107, bohrium (Bh) and 108, hassium (Hs) in sulfuric acid solutions according to the test experiments with their homologs. *Journal of Radioanalytical and Nuclear Chemistry* **251,** 311–314. ISSN: 02365731 (2002).

116. Guseva, L. I. *et al.* On-line investigation of short-lived Os and Re isotopes as a test for chemical studies of 108 (Hs) and 107 (Bh) elements in HCl solutions by continuous chromatography. *Journal of Radioanalytical and Nuclear Chemistry* **260,** 357–362. ISSN: 02365731 (2004).

117. Gregorich, K. E. *et al.* Aqueous Chemistry of Element 105. *Radiochimica Acta* **43,** 223–231 (1988).

118. Zvára, I. *et al.* Chemical Properties of Element 104. **2,** 340 (1966).

119. Zvara, I. *et al.* Experiments on chemistry of element 104-kurchatovium-V. Adsorption of kurchatovium chloride from the gas stream on surfaces of glass and potassium chloride. *Journal of Inorganic and Nuclear Chemistry* **32,** 1885–1894. ISSN: 00221902 (1970).

120. Greenwood, N. N. Recent developments concerning the discovery of elements 101-111. *Pure and Applied Chemistry* **69,** 179–184. ISSN: 00334545 (1997).

121. Silva, R., Harris, J., Nurmia, M., Eskola, K. & Ghiorso, A. Chemical Separation of Rutherfordium. *Inorganic and Nuclear Chemistry Letters* **6,** 871–877 (1970).

122. Zvara, I. *et al. Experiments on chemical identification of spontaneously fissionable isotope of element 105* tech. rep. (1970). http://www.osti.gov/servlets/purl/4954935/.

123. Türler, A., Eichler, R. & Yakushev, A. Chemical studies of elements with Z ≥ 104 in gas phase. *Nuclear Physics A* **944,** 640–689. ISSN: 03759474. http://dx.doi.org/10.1016/j.nuclphysa.2015.09.012 (2015).

124. Timokhin, S. N., Yakushev, A. B., Honggui, X., Perelygin, V. P. & Zvára, I. Chemical Identification of Element 106 by Thermochromatography. *J. Radioanal. Nucl. Chem.* **212,** 31–34. ISSN: 00338230 (1996).

125. Hübener, S. *et al.* Physico-chemical characterization of seaborgium as oxide hydroxide. *Radiochimica Acta* **89,** 737–741. ISSN: 00338230 (2001).

126. Eichler, R. *et al.* Chemical characterization of bohrium. *Nature* **407,** 106–108 (2000).

127. Düllmann, C. E. *et al.* Chemical investigation of hassium (element 108). *Nature* **418,** 859–862. ISSN: 00280836 (2002).

128. Steinegger, P. Open questions on chemistry in the synthesis and characterization of superheavy elements. *Communications Chemistry* **4,** 8–11. ISSN: 23993669. http://dx.doi.org/10.1038/s42004-021-00529-8 (2021).

129. Eichler, R. *et al.* Chemical characterization of element 112. *Nature* **447,** 72–75. ISSN: 0028-0836. http://www.nature.com/doifinder/10.1038/nature05761 (2007).

130. Yakushev, A. *Chemistry experiments with odd- Z elements , Nh and Mc* in (GSI, Darmstadt, 2021), 1–16.

131. Pershina, V., Ilias, M. & Yakushev, A. Reactivity of the Superheavy Element 115 , Mc , and Its Lighter Homologue , Bi , with Respect to Gold and Hydroxylated Quartz Surfaces from Periodic Relativistic DFT Calculations : A Comparison with Element 113 , Nh (2021).

132. Steinegger, P. *et al.* Vacuum Chromatography of Tl on SiO2 at the Single-Atom Level. *Journal of Physical Chemistry C* **120,** 7122–7132. ISSN: 19327455 (2016).

133. Yakushev, A. *et al.* Superheavy element flerovium (Element 114) is a volatile metal. *Inorganic Chemistry* **53,** 1624–1629. ISSN: 00201669 (2014).

134. Pershina, V. Relativistic electronic structure studies on the heaviest elements. *Radiochimica Acta* **99,** 459–476. ISSN: 00338230 (2011).

135. Gaston, N., Opahle, I., Gäggeler, H. W. & Schwerdtfeger, P. Is eka-mercury (element 112) a group 12 metal? *Angewandte Chemie - International Edition* **46,** 1663–1666. ISSN: 14337851 (2007).

136. Jackson, R. A. *The chemistry of mercury* **2,** 48–51. ISBN: 9780333178638 (1978).

137. Dirac, P. A. M. The Quantum Theory of the Electron. *Proc. R. Soc. London* **117,** 610–624 (1928).

138. Desclaux, J. *Atomic Data and Nuclear Data Tables,* 311 (1973).

139. Einstein, A. *Zur Elektrodynamik Bewegter Körper* 1905.

140. Eichler, R. First foot prints of chemistry on the shore of the Island of Superheavy Elements. *Journal of Physics: Conference Series* **420,** 012003. ISSN: 1742-6588. http://stacks.iop.org/1742-6596/420/i=1/a=012003?key=crossref.a4877d08c84891076123d03ba7a38c36 (2013).

141. Rumble, J. R. in *CRC Handbook of Chemistry and Physics* 101st. Chap. Melting, B (CRC PRess, Taylor and Francis, Boca Raton, FL, 2020).

142. Fricke, B. in *Struct. Bonding* J. D. Duni, 89–144 (Springer, Berlin, 1975).

143. Hoffman, D. C., Lee, D. M. & Pershina, V. in *The Chemistry of the Actinide and Transactinide Elements* 1652–1752 (Springer, Dordrecht, 2006). ISBN: 1402035985.

144. Dzuba, V. A. Ionization potentials and polarizabilities of superheavy elements from Db to Cn (Z=105-112). *Physical Review A* **93,** 1–5. ISSN: 24699934. arXiv: 1602.08190 (2016).

145. Pershina, V., Borschevsky, A., Eliav, E. & Kaldor, U. Prediction of the adsorption behavior of elements 112 and 114 on inert surfaces from ab initio Dirac-Coulomb atomic calculations. *Journal of Chemical Physics* **128.** ISSN: 00219606 (2008).

146. Yakushev, A. B. *et al.* First attempt to chemically identify element 112. *Radiochimica Acta* **89,** 743–745. ISSN: 00338230 (2001).

147. Eichler, R. Empirical relation between the adsorption properties of elements on gold surfaces and their volatility. *Radiochimica Acta* **93,** 245–248. ISSN: 00338230 (2005).

148. Eichler, R. *et al.* Attempts to chemically investigate element 112. *Radiochimica Acta* **94,** 181–191. ISSN: 2193-3405. http://www.degruyter.com/view/j/ract.2006.94.issue-4/ract.2006.94.4.181/ract.2006.94.4.181.xml (2006).

149. Yakushev, A. B. *et al.* Chemical identification and properties of element 112. *Nuclear Physics A* **734,** 204–207. ISSN: 03759474 (2004).

150. Oganessian, Y. T. *et al.* Search for new isotopes of element 112 by irradiation of 238U with 48Ca. *European Physical Journal A* **5,** 63–68. ISSN: 14346001 (1999).

151. Barin, I. *Thermochemical Data of Pure Substances* 3rd. ISBN: 3527287450 (VCH Publishers, Inc., New York, USA, 1995).

152. Earnshaw, A. & Greenwood, N. in *Chemistry of the Elements* 2nd, 1201–1226 (Butterworth-Heinemann, Oxford, UK, 1997).

153. Chiera, N. M. *Towards the Selenides of the Superheavy Elements Copernicium and Flerovium* PhD thesis (University of Bern, 2016).

154. Steudel, R. & Eckert, B. in *Topics in Current Chemistry* 1–80 (Springer, Berlin, Heidelberg, 2003).

155. Eichler, B. & Rossbach, H. Adsorption of Volatile Metals on Metal Surfaces and its Application in Nuclear Chemistry: I. Calculations of Adsorption Enthalpies for Hypothetical Superheavy Elements with Z around 114. *Radiochimica Acta* **33,** 121–125. ISSN: 21933405 (1983).

156. Rossbach, H. & Eichler, B. Adsorption von Metallen auf metallische Oberflächen und Möglichkeiten ihrer Nutzung in der Kernchemie. *Akademie der Wissenschaft der DDR,* 1–20 (1984).

157. Roesch, F. & Eichler, B. Adsorption von Metallen auf metallische Oberflaechen und Moeglichkeiten ihrer Nutzung in der Kernchemie. *Zentralinstitut für Kernphysik* **ZFK-575,** 1–20 (1986).

158. Eichler, R. & Schädel, M. Adsorption of radon on metal surfaces: A model study for chemical investigations of elements 112 and 114. *Journal of Physical Chemistry B* **106,** 5413–5420. ISSN: 10895647 (2002).

159. Schädel, M. & Shaughnessy, D. A. *Chemistry of the superheavy elements* 2nd, 377–382 (2015).

160. Eichler, B. & Zvára, I. Evaluation of the Enthalpy of Adsorption from Thermochromatographical Data. *Radiochimica Acta* **30,** 233–238 (1982).

161. Eichler, B. *Volatilization behavior of transactinides from metal surfaces and melts* tech. rep. 03-01 (Paul Scherrer Institute, Villigen, 2002), 1.

162. Freundlich, H. Über die Adsorption in Lösnungen. *Z. Phys. Chem* **57,** 385–470 (1907).

163. Foo, K. Y. & Hameed, B. H. Insights into the modeling of adsorption isotherm systems. *Chemical Engineering Journal* **156,** 2–10. ISSN: 13858947 (2010).

164. Brunauer, S., Emmett, P. H. & Teller, E. Adsorption of Gases in Multimolecular Layers. *Journal of the American Chemical Society* **60,** 309–319. ISSN: 15205126 (1938).

165. Hill, T. L. Theory of Physical Adsorption. *Advances in Catalysis* **4,** 211–258. ISSN: 03600564 (1952).

166. McMillan, W. G. & Teller, E. The Assumptions of the B.E.T. Theory. *Journal of Physical Chemistry,* 17–20 (1951).

167. Atkins, P. *Physical Chemistry* 8th, 917 (Oxford University Press, Oxford, UK, 2006).

168. Zvara, I. Problems in thermochromatographic separation of radioelements. *Journal of Radioanalytical and Nuclear Chemistry* **204,** 123–134 (1996).

169. Zvára, I. Simulation of Thermochromatographic Processes by the Monte Carlo Method. *Radiochimica Acta* **38,** 95–102. ISSN: 21933405 (1985).

170. Sommerfeld, A. Ein Beitrag zur hydrodynamischen Erklärung der turbulenten Flüssigkeitsbewegungen. *Atti del IV Congresso Internazionale dei Matematici* **3,** 116–124 (1908).

171. Gilliland, E. R. Diffusion Coefficients in Gaseous Systems. *Industrial and Engineering Chemistry* **26,** 681–685. ISSN: 00197866 (1934).

172. Yang, L. M. Kinetic theory of diffusion in gases and liquids I. Diffusion and the Brownian motion. *Proceedings of the Royal Society of London. Series A. Mathematical and Physical Sciences* **198,** 94–116. ISSN: 0080-4630 (1949).

173. Zvára, I. *The Inorganic Radiochemistry of Heavy Elements* ISBN: 9781402066016 (Springer, Berlin, 2008).

174. Golay, M. J. E. Gas Chromatographic Terms and Definitions. *Nature* **182,** 1146–1147 (1958).

175. Poppe, H. Mass transfer in rectangular chromatographic channels. *Journal of Chromatography A* **948,** 3–17. ISSN: 00219673 (2002).

176. Ašperger, S. *Chemical Kinetics and Reaction Mechanisms* 2nd, 14–25. ISBN: 9781461348719 (Croatian Academy of Sciences and Arts, Zagreb, 2003).

177. Jorpes, J. E. *Jac. Berzelius: His Life and Work* 61–63 (UC Press, Berkeley, 1970).

178. Berzelius, J. Recherches sur un nuveau corps minéral trouvé dans le soufre fabriqué à Fahlun. *Annales de Chimie et de Physique* **9,** 160–180 (1818).

179. Saunders, A. P. The allotropic forms of selenium. *Journal of Physical Chemistry* **4,** 423–513. ISSN: 00223654 (1899).

180. Minaev, V. S., Timoshenkov, S. P. & Kalugin, V. V. Structural and Phase Transformations in Condensed Selenium. *Journal of Optoelectronics and Advanced Materials* **7,** 1717–1741. ISSN: 09544119 (2005).

181. Chiera, N. M., Eichler, R., Vögele, A. & Türler, A. Vapor deposition coating of fused silica tubes with amorphous selenium. *Thin Solid Films* **592,** 8–13. ISSN: 00406090. arXiv: 9809069v1 [arXiv:gr-qc]. http://dx.doi.org/10.1016/j.tsf.2015.08.043 (2015).

182. Chiera, N. M. *Towards the Selenides of the Superheavy Elements Copernicium and Flerovium* PhD thesis (University of Bern, 2016), 170.

2 Preparation and Classification of Chromatographic Surfaces of Selenium

Paper Title: Amorphous and Trigonal Selenium Films for Chromatographic Applications

Authors: P. Ionescu[a,b], R. Eichler[b], A. Türler[a]

[a]University of Bern, 3012 Bern, Switzerland

[b]Paul Scherrer Institute, 5232 Villigen, Swizerland

To be submitted to *Thin Solid Films*.

Author Contribution: All authors contributed to the study conception and design. Material preparation, data collection and analysis were performed by P. Ionescu. The first draft of the manuscript was written by P. Ionescu and all authors commented on previous versions of the manuscript.

2.1 Abstract

Three methods for the preparation of chromatographic amorphous and trigonal selenium surfaces are presented. The methods presented are a novel selenium casting method, photo-induced chemical vapour deposition and physical vapour deposition. The methods are compared for their ability to cover surfaces of complex geometry, film thickness and stability to aging. The allotropic conversion between amorphous and trigonal selenium was investigated, and it was found that trigonal selenium maintains reactive monovalent Se atom sites after complete crystallization.

2.2 Introduction

Selenium is a highly versatile element owing to its allotropy, exhibiting different chemical properties even in the elemental state [1, 2]. The versatility extends to its uses in many contemporary materials for optoelectronics and nanoscience [3–6] which have specialized applications in the biomedical field [7] and environmental sector [8]. Among its many uses, thin films of elemental selenium have been historically used extensively in xerography devices, but also found application in optical sensors, medical imaging, data storage devices, semiconductors and even radiation detectors [9–11]. Even though many publications exist on the chromatographic detection of selenium, its extensive use as detectors and in thin films has high untapped potential for seeing it used as the stationary phase for both gas and liquid chromatography. Recently, in the fundamental research of superheavy elements, this potential was recognized and a series of gas chromatography experiments began first with Hg as the lighter homolog of Cn ($Z = 112$) [12, 13]. Later, a first chemical experiment was performed with Cn ($Z = 112$) on a selenium chromatographic surface, albeit inconclusive results [14]. In these several week-long experiments, stable films of Se were required on Positive Implanted N-type (PIN) diode α-particle and spontaneous fission detectors, so that the detector surface would not change for the duration. The Se films were also required to be relatively thin ($\approx$ 200 nm) in order to maintain a good energy resolution of the detected radiation.

There are a number of ways to obtain elemental Se coatings ranging from Physical Vapor Deposition (PVD) via pulsed laser evaporation [15, 16], vapour-transport deposition [17], to solution growth [18, 19]. In this work, a number of methods for Se coatings were explored. The properties of the resulting Se films were characterized comparatively for the ultimate use as a stationary phase in gas chromatography. The methods were chosen based on their ability to produce uniform, stable films, the ability to coat substrates of complex shapes and resulting thickness. The methods employed were a novel mold casting method, Photo-Induced Chemical Vapor Deposition (PICVD), and evaporative Physical Vapor Deposition (PVD). Allotropy plays an important role in selenium chemistry and can exhibit complex behaviour. However, confusing and misleading terminology that has emerged in the study of selenium through nam-

ing conventions based on the color of the material which does not necessarily represent the absolute arrangement of atoms in the bulk material. In this work, the predominant allotropes of Se used were amorphous Se_n (*a*-Se, n ≈ 1 - 6) usually in the form of short chains [2, 17, 20], amorphous vitreous Se_n (n ≈ 8) in a mixture of chains and rings [21], and finally the most stable form, crystalline trigonal Se_∞ (*t*-Se) which forms polymeric chains [22–24].

The different chromatographic surfaces produced were analyzed and compared using isothermal gas chromatography with a ^{197m}Hg radioactive tracer. Hg was chosen because of an already known adsorption interaction with amorphous and trigonal Se allotropes from earlier experiments established at $-\Delta H_{ads}^{Hg}(t\text{-Se}) \geq 60$ kJ/mol and $-\Delta H_{ads}^{Hg}(a\text{-Se}) \geq 85$ kJ/mol for *t*-Se and amorphous *a*-Se respectively [12]. The resulting deposition patterns of the chromatography were then interpreted using a modified microscopic Monte-Carlo Simulation (MCS) of a gas chromatography pioneered by Zvára [25].

2.3 Experimental - Preparation of Cylindrical Gas Chromatography Columns

2.3.1 Selenium Cast Method

All fused silica tubes were cleaned in preparation for coating by heating to 1000°C with a N_2 gas stream. Fused silica tubes ($\varnothing_{inner}$ 4mm) were cut to 20 cm segments and sealed by melting on one end. Figure 22 illustrates the process of the Se cast; Se granules (Chempur. 99.999%) were melted at 250°C. PTFE tubing ($\varnothing_{outer}$ 3mm) reinforced with a brass core was introduced into the melt slowly, displacing the selenium along the sides. The system was kept in this state for 5 minutes to avoid the formation of bubbles and cooled rapidly by immersing the fused silica in iced water. Once the system was cold, the chromatographic column was cut open at the sealed end and the PTFE tubing removed, leaving a solid vitreous Se column of 0.5 mm wall thickness. Finally, the vitreous columns were annealed in an oven at 75°C for up to 48 hours to convert the column to the *t*-Se allotrope.

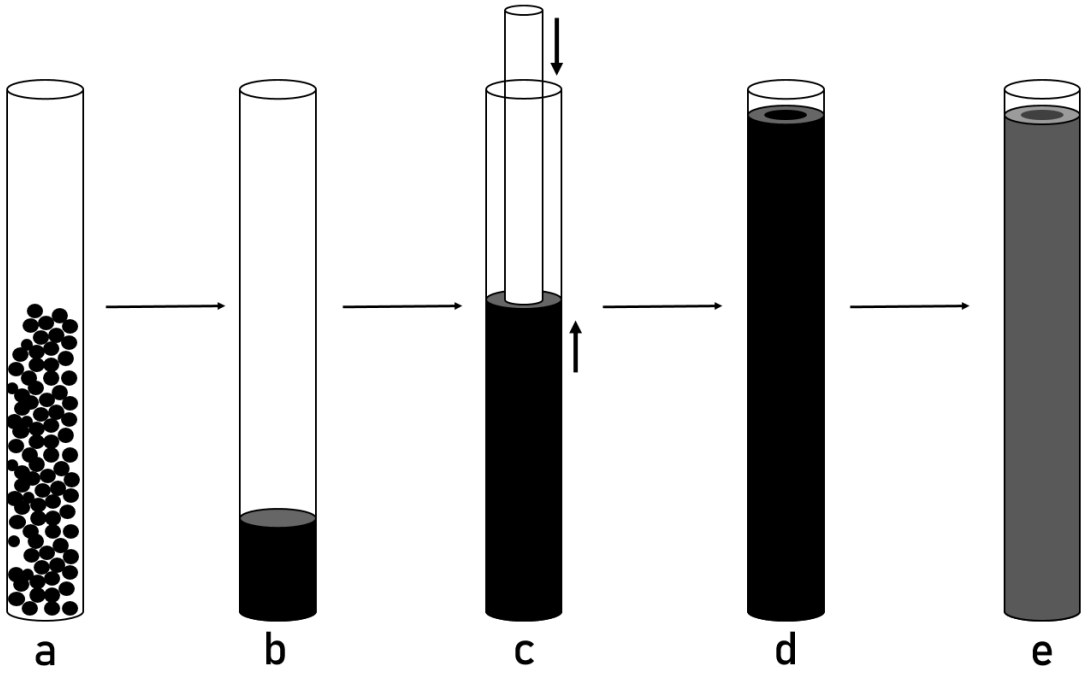

Figure 22: Casting method for solid Se chromatographic columns. **a** Granular Se is packed into a quartz tube where it is **b** melted at 250°C. **c** A PTFE tube is inserted displacing the Se melt around its sides and allowed to cool. **d** The PTFE is removed from the solidified amorphous black Se leaving a cylindrical column which can be **e** converted to gray t-Se.

2.3.2 Photo-Induced Chemical Vapour Deposition (PICVD) Method

Se granules were heated in a fused silica tube to 450°C in a H_2 gas stream (Figure 23).

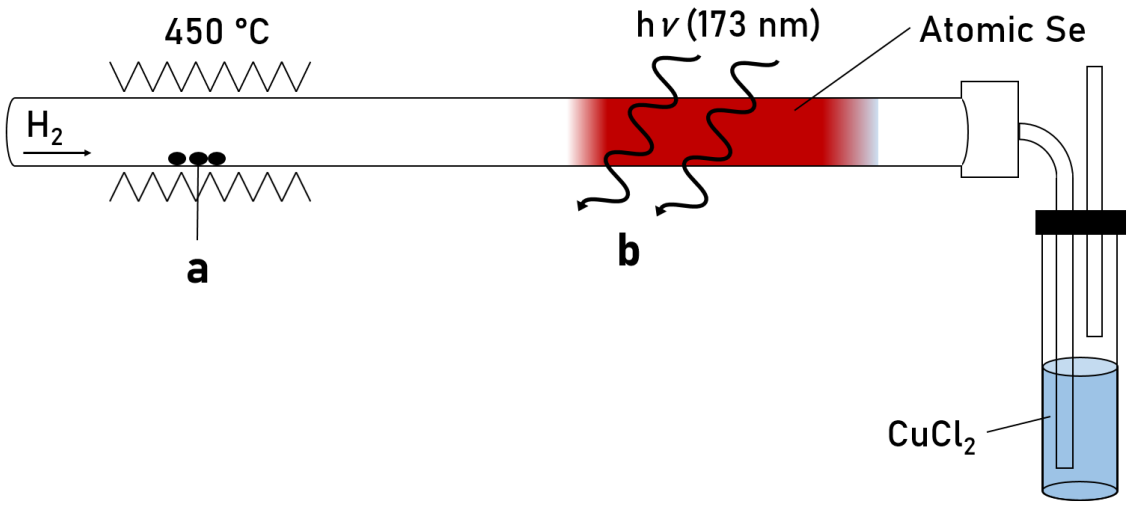

Figure 23: Schematic of the PICVD used to coat quartz tubes. **a** A hydrogen gas stream reacts with melted Se at 450°C. The gaseous H_2Se is transported in the stream to **b** where a 173 nm UV lamp photolyzes it. Atomic Se deposits controlled by diffusion onto the walls. Any unreacted H_2Se is caught in a trap with $CuCl_2$ solution.

The two species reacted according to reaction 32.

$$H_{2(g)} + Se_{(l)} \longrightarrow H_2Se_{(g)} \tag{32}$$

While H_2Se formation is more efficient at higher temperatures, for the purposes of this experiment lower temperatures were more appropriate, as the Se would otherwise evaporate too quickly without reacting and condense outside the oven. The H_2Se was carried by the gas stream to a 173 nm UV lamp where the molecule underwent photolysis according to reaction 33.

$$H_2Se_{(g)} \xrightarrow{hv} H_{2(g)} + Se_{(s)} \tag{33}$$

Any unreacted H_2Se was captured in a gas washing bottle with $CuCl_2$. By moving the UV light source, a tube of indefinite length can be coated and coating was performed until the gas wash bottle began showing signs of CuSe formation, indicating that no more photolysis was taking place. It was attempted to convert the resulting chromatographic columns from the

freshly deposited amorphous atomic (red) Se to the gray *t*-Se state, however tempering at 75°C for up to 48 hours resulted in visibly only some areas changing colour to gray.

2.3.3 Thin Film Physical Vapor Deposition (PVD) Method

For the coating of rectangular flat surfaces, quartz slides were cleaned for 15 minutes inside an UV-Ozone cleaner (Jelight Company Inc. 42-220). The clean substrate was then placed inside a 3D-printed mask to prevent Se deposition on unwanted surfaces (Figure 24).

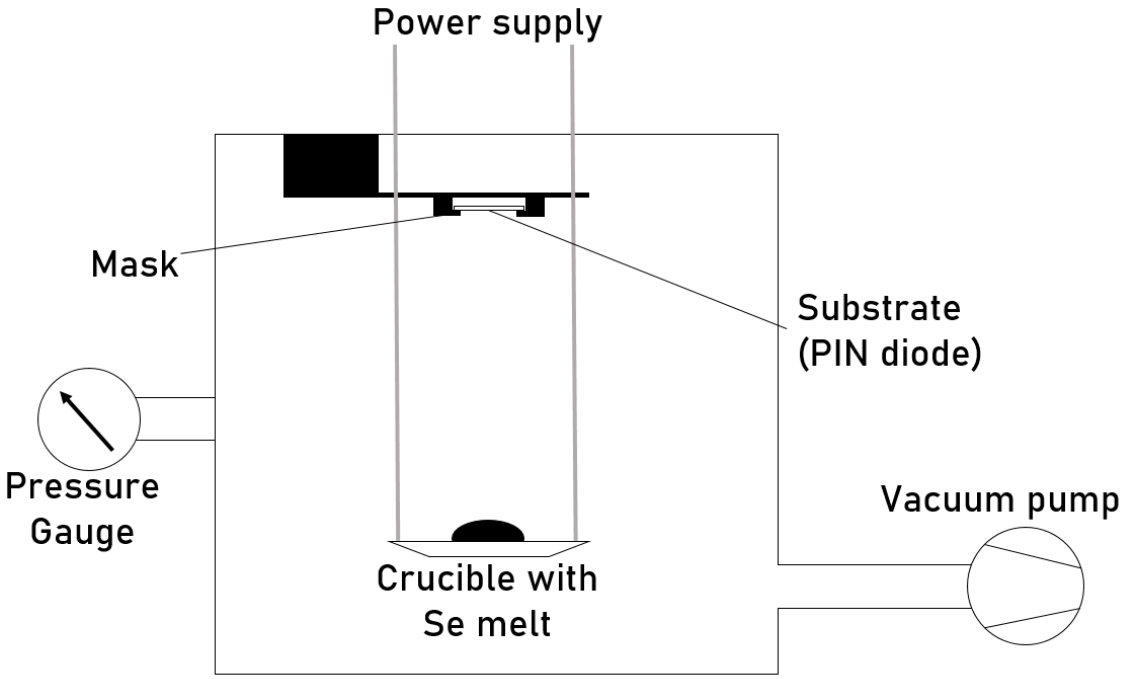

Figure 24: Schematic of the PVD apparatus used in the coating of samples. Se powder is pre-melted in the crucible before evacuation to form a solid pellet. This is then evacuated to $\leq 10^{-5}$ hPa. The crucible generates heat (40 W), evaporating the Se which condenses on the substrate. A mask ensures deposition only where required.

Ground Se powder (Chempur 99.999%) was placed in the heating crucible and pre-heated to melt in order to form a droplet then allowed to cool again. This prevented the powder from falling out of the crucible during evacuation and helped evaporate any water adsorbed to the

surface. The PVD apparatus was then evacuated to a pressure of $\leq 10^{-5}$ hPa and a current heated the crucible to evaporate the Se directly onto the substrate at room temperature. The resulting amorphous Se films were visibly uniform, deep transparent red. Conversion to the gray *t*-Se allotrope was achieved by annealing at 75°C or by exposing the film to a 253 nm UV lamp for 12 hours, which changed the films to a uniform opaque metallic gray. Care must be taken in avoiding ozone forming UV lamps, as we observed oxidation of the Se layer.

2.3.4 Isothermal Gas Chromatography

Production of the carrier-free ^{197m}Hg (t_{1_2} = 23.8 h, main γ-ray 33% 133.99 keV) radioisotope for the gas chromatographic investigation in all experiments was done using the Injector II cyclotron of the High Intensity Proton Accelerator (HIPA) facility at the Paul Scherrer Institute with proton irradiation of a gold foil (99.95% purity, 0.1 mm thickness, ⌀ 19 mm) using the reaction:

$$^{\text{nat}}\text{Au}(p,n)^{197m}\text{Hg} \tag{34}$$

For isothermal gas chromatography the activated gold foil was then placed in a fused silica tube inside a starter oven where the ^{197m}Hg tracer was volatilized at 1000°C in a He gas flow (99.9990 vol% purity) (Figure 25). The He flow rate was controlled by a mass flow controller (Brooks Instruments Series 5851E, i) and GC was done at standard pressure.

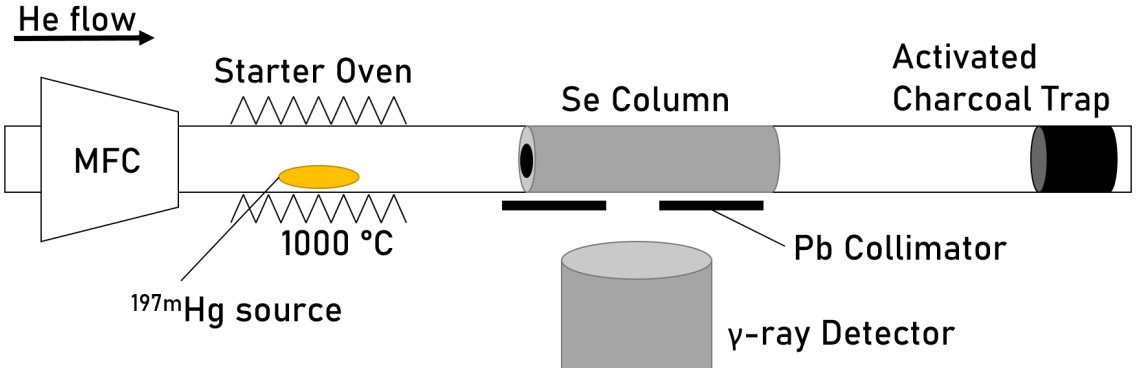

Figure 25: Schematic of the isothermal gas chromatography setup. A He flow regulated by a Mass Flow Controller (MFC) passes over the irradiated Au foil at 1000°C transporting the ^{197m}Hg tracer to the Se stationary phase. Any tracer which did not deposit in the column was trapped on activated charcoal. After the experiment, the tracer deposition was measured along the column and activated charcoal trap using a collimated γ-ray detector. For PVD covered quartz slides, a rectangular Teflon® channel was used.

The tracer was allowed to interact with the chromatographic surface while any escape from the back of the column was prevented using an activated charcoal trap. The deposition pattern was then established using a lead collimated (2 cm Pb thickness, 1cm wide window) high-purity germanium (HPGe) γ-ray detector (Ortec GEM-23185) in 1 cm segments. In all experiments, all activity was accounted for and no deposition of ^{197m}Hg on fused silica was detected or lost elsewhere.

2.4 Results and Discussion

2.4.1 Properties of Physical Vapor Deposition Films

PVD was successfully used to obtain consistently uniform *a*-Se films without holes, which could be converted to the *t*-Se allotrope through annealing at 75°C or UV light ($\lambda = 250$ nm) (Figure 26). The films adhere well to quartz substrates and resist light scratching or washing off with solvents.

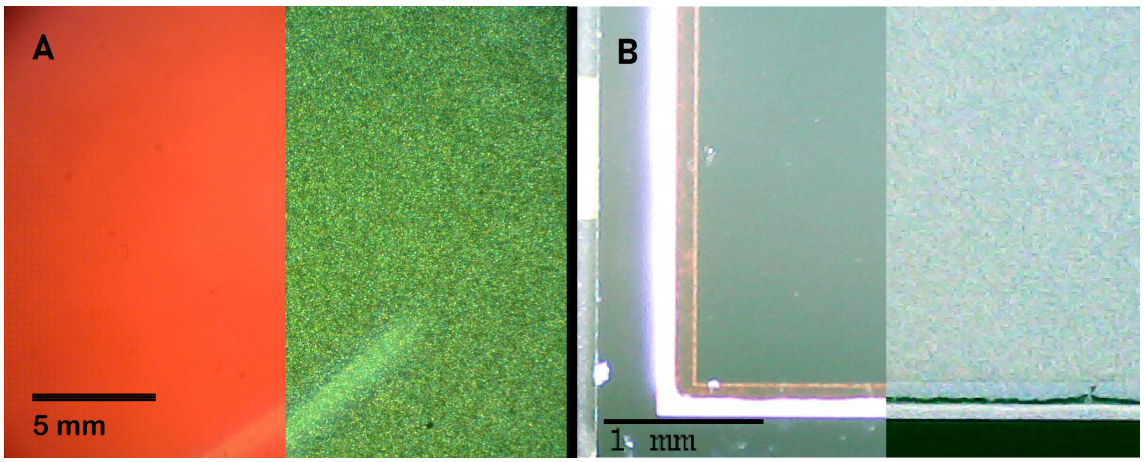

Figure 26: **A:** Microscopy image of quartz slide with the *a*-Se PVD layer before and after conversion to *t*-Se, transmission lighting. **B:** PIN diode coated in *a*-Se before, and after conversion to *t*-Se with incident lighting.

Care must be taken to avoid UV conversion with O_3 generating lamps, as it was observed that the surface of the Se layer oxidised, making it water soluble. The thickness of the films was measured at the edge using Atomic Force Microscopy (AFM) (Nanosurf FlexAFM) and found to be 225 nm, with no change to the gray allotrope (Figure 27). Films were very smooth. Profilometry (Veeco Dektak 8) also revealed surface roughness, and it was found that little change occurred after the conversion process. The total surface area change was estimated at 1% (min) to 100% (max) from *a*-Se to *t*-Se, which MCSs found negligible for the purposes of our gas chromatography.

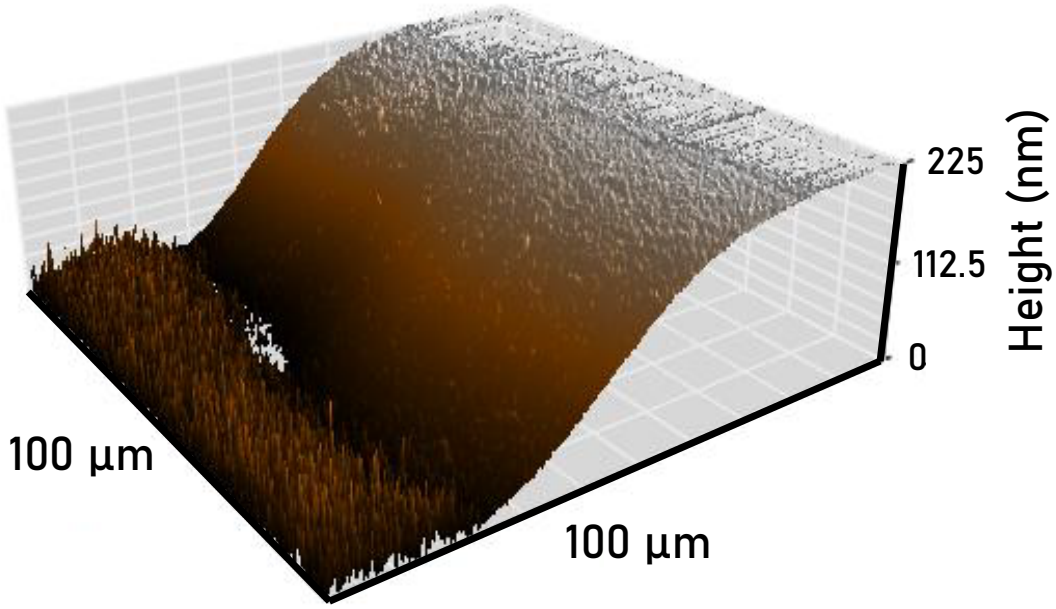

Figure 27: Atomic force microscopy image of a deposited a-Se film using PVD. Part of the quartz carrier was masked to allow measurement of the thickness of the film at 225 nm. The surface is homogeneous and smooth.

Isothermal GC at standard temperature and pressure was performed with a 50 ml/min He flow over a freshly prepared *a*-Se as well as a converted *t*-Se column (Figure 28). In order to analyze the chromatographic Se surface, the GC deposition pattern of the ^{197m}Hg tracer was interpreted using a MCS. Earlier experiments established the $-\Delta H_{ads}^{Hg}(t-Se) \geq 60$ kJ/mol and $-\Delta H_{ads}^{Hg}(a-Se) \geq 85$ kJ/mol for *t*-Se and amorphous *a*-Se respectively [12]. The MCS was programmed to randomly assign an *a*-Se or *t*-Se surface for each tracer interaction thereby simulating a heterogeneous surface. The proportion of the two allotropes was then varied until the deposition could be adequately described.

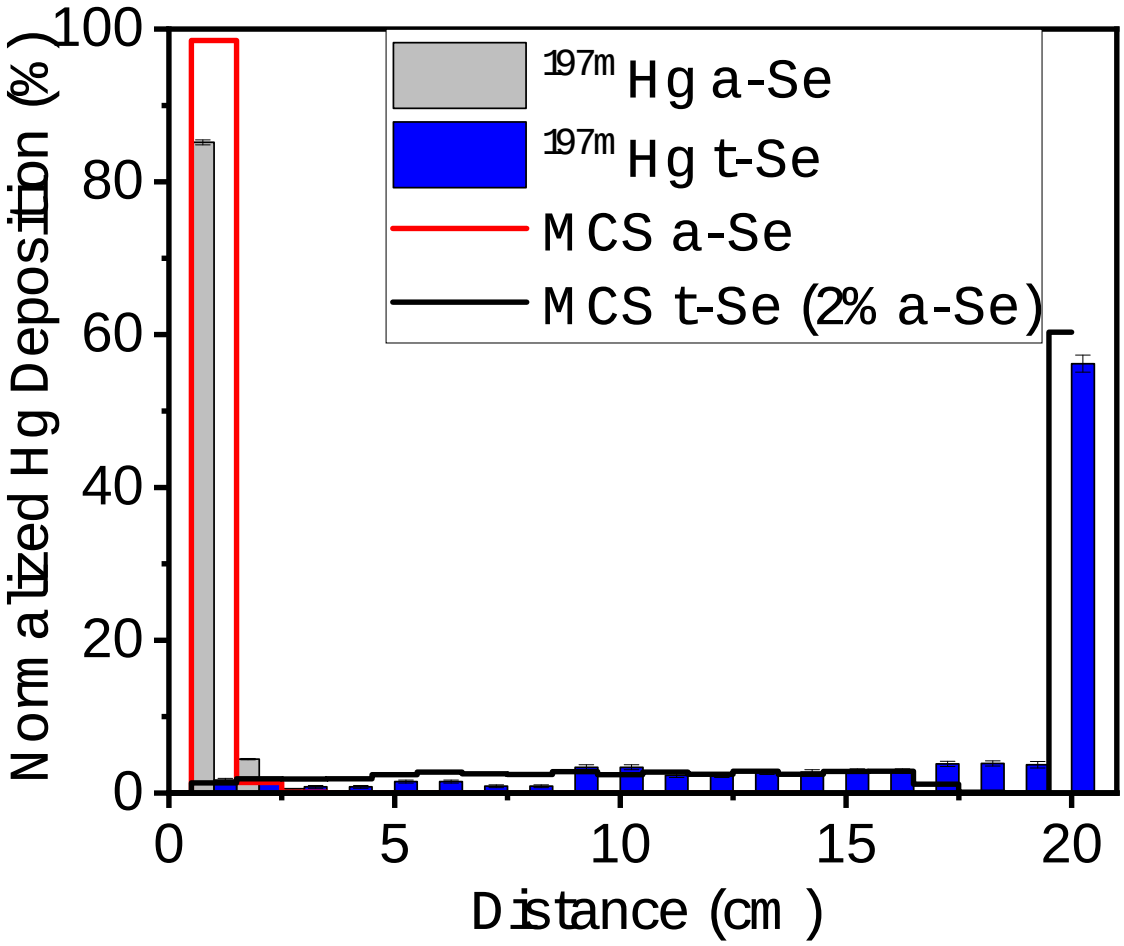

Figure 28: Isothermal GC at 25 °C, 50 ml/min He flow showing the ^{197m}Hg deposition pattern on red a-Se (gray bars) with the corresponding MCS (red line) and the same experiment repeated with a gray t-Se surface (blue bars) and the corresponding MCS (black line) with a 2% a-Se component. At position 20 cm an activated charcoal trap collects all nuclides that did not remain in the column.

The previously established adsorption enthalpy for amorphous *a*-Se was accurate in simulating the observed deposition pattern. Due to the slight retention of ^{197m}Hg in the *t*-Se column, the MCS described the surface best with an $\approx 2\%$ *a*-Se coverage. Attempts were made to reduce the *a*-Se surface proportion in a number of methods; repeated heating as described in [2], and CS_2 washing (due to the selective *a*-Se solubility in the solvent [26]), however the deposition did not change significantly. Since no method was able to fully remove the *a*-Se, an

explanation could be that the deposition of ^{197m}Hg was not truly due to *a*-Se, but instead due to open *t*-Se chain ends. As these are not divalent, as Se in the bulk, they should exhibit increased reactivity, similar to the amorphous allotrope. The higher surface roughness could also contribute to further exposed *t*-Se chain ends. It has been shown, that in *t*-Se approximately 1% of atoms are monovalent on chain ends [27, 28]. Image 29 shows an Scanning Electron Microscopy (SEM) Se film converted to the gray allotrope via heat.

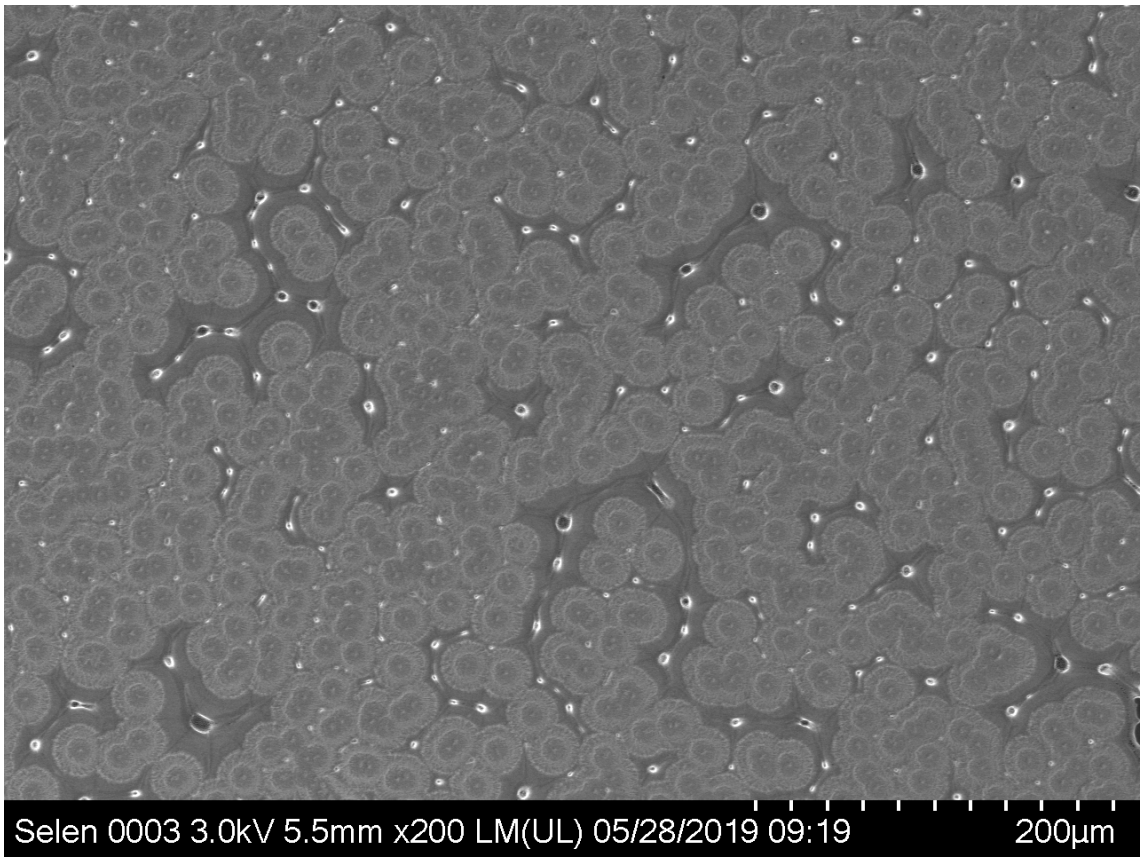

Figure 29: Scanning Electron Microscopy image of radially crystallized *t*-Se. The crystals are ≈ 34 μm in diameter.

When assuming a perimeter of open *t*-Se chain ends around each circular crystallite of ⌀ 34 μm, $\approx 1.3\%$ of the total surface area will make up monovalent Se atoms. When considering the above mentioned maximum factor 2 increase in surface area, it is plausible that despite conversion, *t*-Se can exhibit some *a*-Se-like behaviour in this poly-crystalline state. This finding is rather significant for the application in gas chromatography for superheavy element chem-

istry, as a heterogeneous acting surface can significantly complicate experiments and require more data before being able to extract meaningful results. Additionally, controlling the crystallization process and creating less open *t*-Se chain ends could affect the behaviour of such a surface.

X-Ray Diffraction (XRD) (Bruker AXS D8, Cu-Kα $\lambda = 1.5419$ Å) was performed on the thin Se films before and after conversion. The pattern was compared to the standard *t*-Se from the International Center for Diffraction Data [29] and showed that the annealing process successfully resulted in trigonal Se (Figure 30).

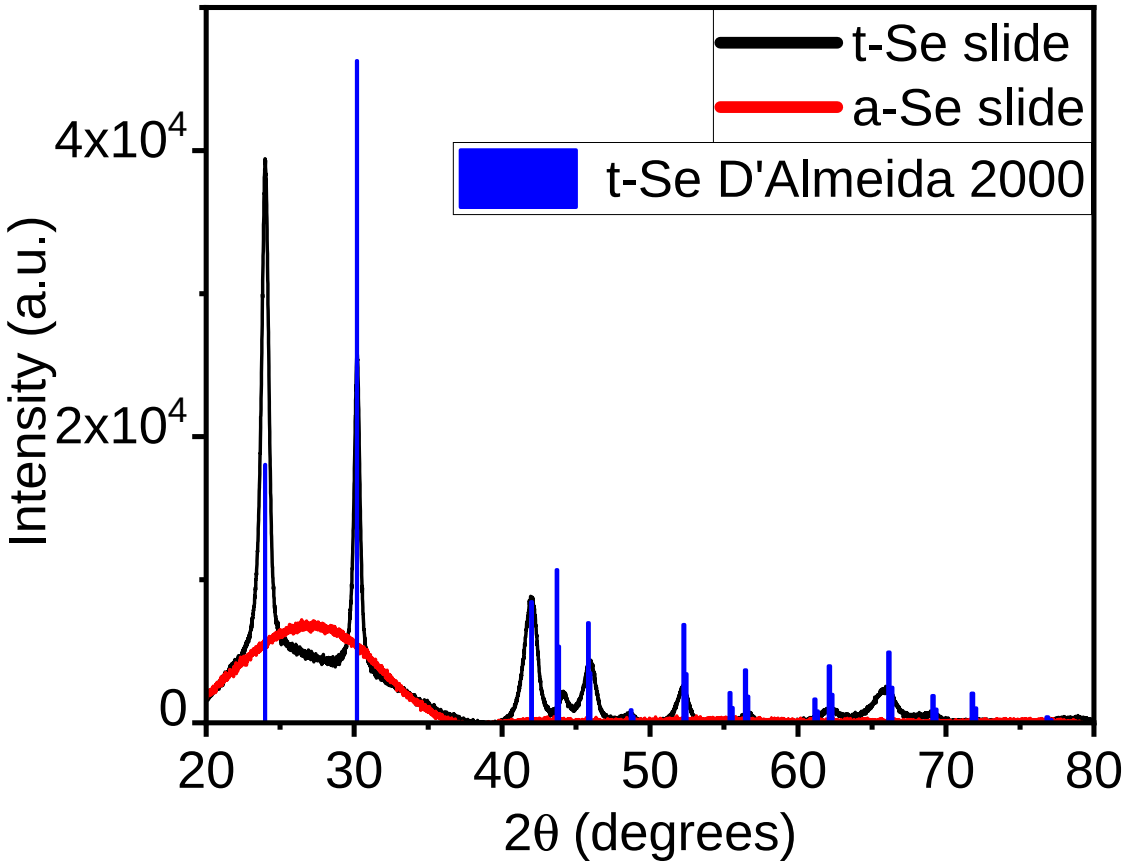

Figure 30: XRD pattern of thin Se films deposited using the PVD method. The red line shows a freshly deposited amorphous red Se film, the black line a t-Se film which has been allowed to crystallize from the amorphous phase. The blue pattern shows the standard literature reference for t-Se [29].

2.4.2 Properties of Selenium Cast

The cast method was successfully used to consistently produce vitreous black selenium tubes ($\varnothing_{inner}$ 3 mm, l_{max} 25cm) which were converted to the *t*-Se allotrope. Upon conversion, the smooth black amorphous surface changed visibly to a more textured metallic gray. The columns were solid, smooth with a wall thickness of 0.5 mm (Figure 31). The inherent wall strength makes the Se columns robust enough to stand free of the fused silica surroundings. Compared to previously used vapor-transport deposition methods described in [17], this was advantageous, as it ensured a 100 % surface coverage of the column.

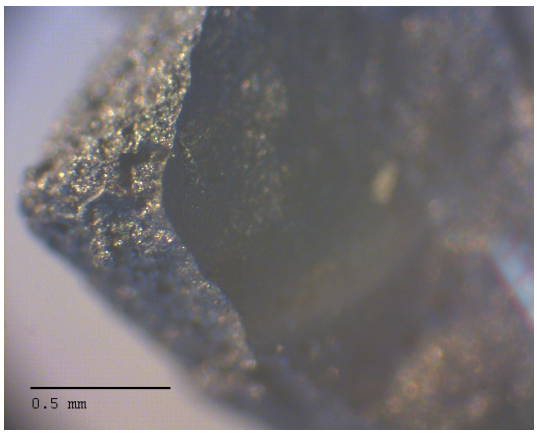

Figure 31: Fragment from a cast Se column converted to the *t*-Se allotrope showing the cross section of the wall (left).

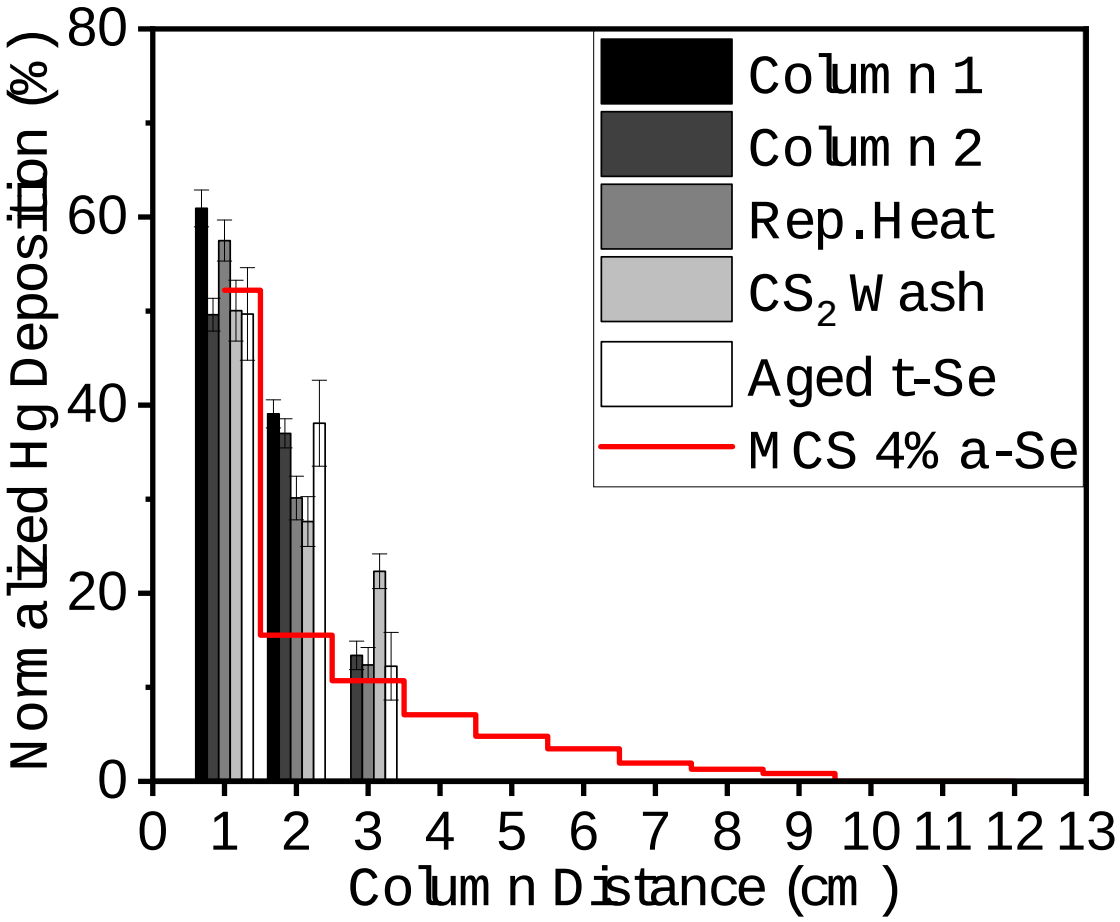

Figure 32: Normalized ^{197m}Hg deposition pattern in *t*-Se columns produced using the same method with different after-treatments (bars) and MCS with 4% *a*-Se surface coverage (red line). 25 ml/min He flow at 25°C isothermal conditions. Deposition pattern did not change for repeated heat conversion attempts (Rep. Heat), washing with CS_2 or aging the column for over 1 year.

Results in Figure 32 were consistent between repeated experiments. As can be seen, the MCS used to describe the deposition estimated a 4% *a*-Se surface despite the conversion process. Again, attempts to remove any *a*-Se via repeated annealing, CS_2 washes, or simple aging of the column for over a year did not change the deposition pattern, indicating complete conversion. It is noteworthy, that compared to the rectangular chromatography channel, the deposition of ^{197m}Hg occurred on the first section of the column instead of passing through and depositing on the charcoal trap. We can explain this behaviour using a MCS, which shows

that for our cylindrical shaped columns, there are more frequent tracer-surface interactions (in the order of 15x more when compared to our one-sided rectangular channel). Therefore, each ^{197m}Hg tracer is more likely to encounter a reactive Se site, where it will adsorb readily.

2.4.3 Properties of Photo-induced Chemical Vapor Deposition Films

Quartz columns produced via PICVD method ($\varnothing_{inner}$ 4 mm) resulted in a complete bright red coverage of the fused quartz tube. The first and final centimeter of the coating showed gradients of a deposition, as the UV light could not reach these points evenly. The columns were converted through annealing at 75°C and used in isothermal gas chromatography (Figure 33). Visibly, the columns changed colour to a pale gray.

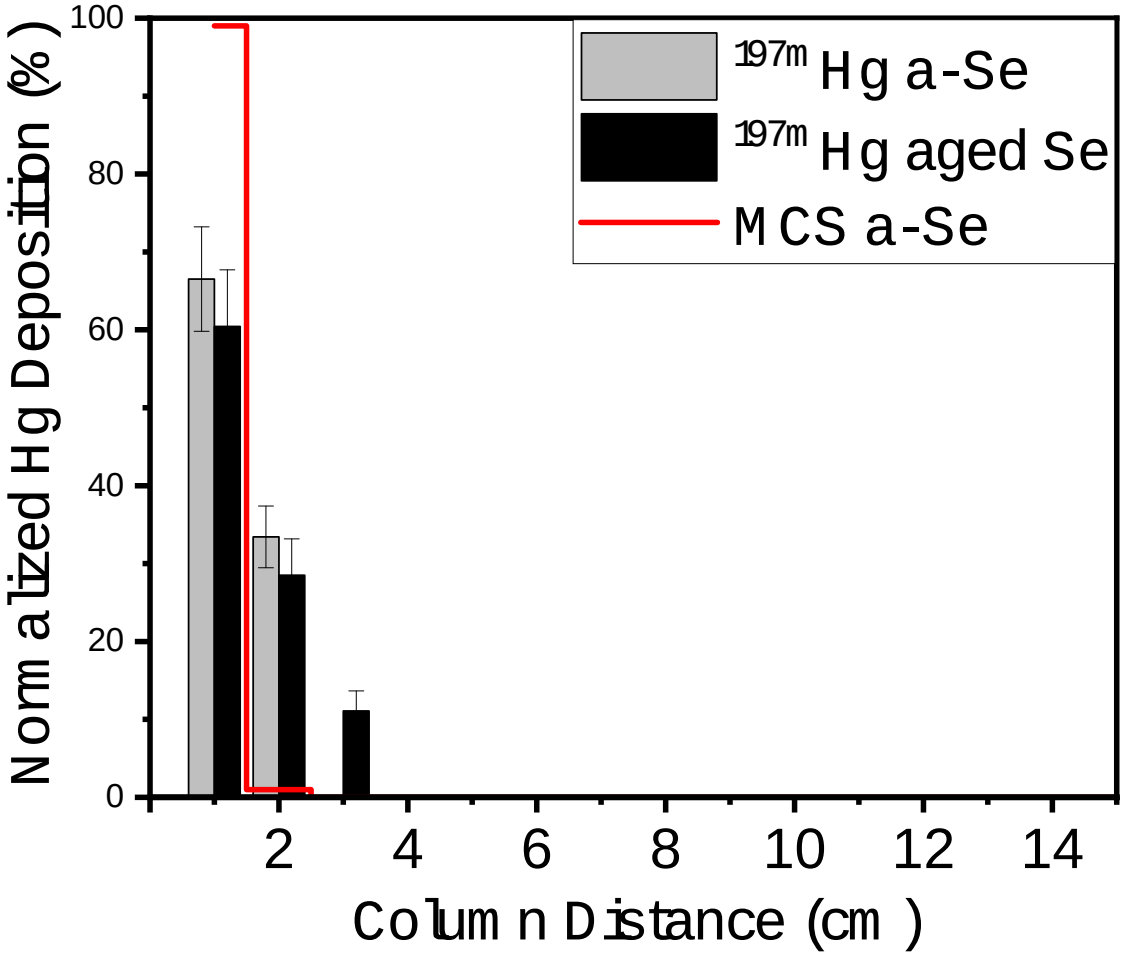

Figure 33: Isothermal chromatography at room temperature showing diffusion controlled deposition of ^{197m}Hg on both, a freshly prepared a-Se surface using the PICVD method (gray) and the same surface after heat treatment and aging over one year to facilitate conversion to t-Se. Note that due to the coating method, the first centimeter of the column has a lower deposition due to a coating gradient, therefore making the deposition less sharp. The MCS (red line) shows the sharp deposition peak of a purely *a*-Se coated column under these conditions. Position of activated charcoal trap at 20 cm.

Even after conversion and aging, the deposition of ^{197m}Hg was sharp in the first centimeters of the column. Profilometry scans showed an 800 nm layer thickness and a rougher surface compared to the PVD method. The as-deposited atomic *a*-Se coating is rougher by 10 - 120 % compared to the PVD *a*-Se. Compared to the other methods, as H_2Se is photolyzed, only single atoms of Se deposit on the surface at a time (during PVD) short chains can volatilize [17]). The increased surface roughness can be explained by the less tightly packed Se atoms, which will deposit on the first surface they encounter. Additionally, due to this increasingly disordered arrangement, crystallization to the gray *t*-Se allotrope is likely inhibited. Therefore, crystallization of longer polymer chains less likely, resulting in more reactive sites where ^{197m}Hg is retained.

2.5 Conclusions

The selenium coating and crystallization of fused silica chromatographic columns was investigated using XRD, AFM, profilometry and isothermal gas chromatography with the use of ^{197m}Hg as a tracer. Several methods for the production of chromatographic columns were explored, including a novel casting method, PICVD and evaporative PVD. The previously established adsorption enthalpies for Hg on Se were used in a MCS to analyze a heterogeneous surface and it was found that while crystallized *t*-Se has some amorphous *a*-Se characteristics, these were not due to incomplete crystallization but rather due to the polycrystalline nature of

the material. Open-ended *t*-Se chains likely act as reactive sites and their number influences the ^{197m}Hg adsorption during gas chromatography. It is likely not possible to completely prevent these open-ended chains, however they could likely be minimized using a slow crystallization with less nucleation sites (i. e. lower temperatures).

For the purpose of gas chromatographic investigations of SHE copernicium, the finding of a heterogeneous chromatographic stationary phase is significant as it adds complexity. Since there is a probability involved of the SHE interacting with one of the two surfaces behaving differently, more data will be required for improved statistics. Additionally, since the degree of polycrystallinity can vary between detectors, it must always be quantified using homolog studies. These findings will prove invaluable to future superheavy experimental campaigns which generally rely on non-heterogeneous surfaces for their experiments.

References

1. Saunders, A. P. The allotropic forms of selenium. *Journal of Physical Chemistry* **4,** 423–513. ISSN: 00223654 (1899).
2. Minaev, V. S., Timoshenkov, S. P. & Kalugin, V. V. Structural and Phase Transformations in Condensed Selenium. *Journal of Optoelectronics and Advanced Materials* **7,** 1717–1741. ISSN: 09544119 (2005).
3. Wagner, A. M., Knipe, J. M., Orive, G. & Peppas, N. A. Quantum dots in biomedical applications. *Acta Biomaterialia* **94,** 44–63. ISSN: 18787568. `https://doi.org/10.1016/j.actbio.2019.05.022` (2019).
4. Ponraj, J. S. *et al.* Photonics and optoelectronics of two-dimensional materials beyond graphene. *Nanotechnology* **27.** ISSN: 13616528 (2016).
5. Fan, T., Xie, Z., Huang, W., Li, Z. & Zhang, H. Two-dimensional non-layered selenium nanoflakes: Facile fabrications and applications for self-powered photo-detector. *Nanotechnology* **30.** ISSN: 13616528 (2019).

6. Huang, W. *et al.* Recent Advances in Semiconducting Monoelemental Selenium Nanostructures for Device Applications. *Advanced Functional Materials* **30,** 1–25. ISSN: 16163028 (2020).

7. Khurana, A., Tekula, S., Saifi, M. A., Venkatesh, P. & Godugu, C. Therapeutic applications of selenium nanoparticles. *Biomedicine and Pharmacotherapy* **111,** 802–812. ISSN: 19506007 (2019).

8. Sakho, E. & Oluwafemi, O. S. in *Nanomaterials for Solar Cell Applications* 1st, 387 (Elsevier, Amsterdam, 2019). ISBN: 978-0-12-813337-8.

9. Chowdhury, T. A., Oner, C. & Mandal, K. C. *Synthesis and Characterization of Amorphous Selenium Alloys Radiation Detectors* in *2017 IEEE Nuclear Science Symposium and Medical Imaging Conference, NSS/MIC 2017 - Conference Proceedings* (2018), 1–4. ISBN: 9781538622827.

10. Eggleton, B. J., Luther-Davies, B. & Richardson, K. Chalcogenide photonics. *Nature Photonics* **5,** 141–148. ISSN: 17494885 (2011).

11. Rowlands, J. & Kasap, S. Amorphous semiconductors usher in digital X-ray imaging. *Physics Today* **50,** 24–30. ISSN: 00319228 (1997).

12. Chiera, N. M. *et al.* Interaction of elemental mercury with selenium surfaces: model experiments for investigations of superheavy elements copernicium and flerovium. *Journal of Radioanalytical and Nuclear Chemistry* **311,** 99–108. ISSN: 15882780 (2017).

13. Eichler, R. *et al.* Attempts to chemically investigate element 112. *Radiochimica Acta* **94,** 181–191. ISSN: 2193-3405. `http://www.degruyter.com/view/j/ract.2006.94.issue-4/ract.2006.94.4.181/ract.2006.94.4.181.xml` (2006).

14. Chiera, N. M. *Towards the Selenides of the Superheavy Elements Copernicium and Flerovium* PhD thesis (University of Bern, 2016).

15. Hansen, S. G. & Robitaille, T. E. Characterization of the pulsed laser evaporation process: Selenium thin-film formation. *Applied Physics Letters* **50,** 359–361. ISSN: 00036951 (1987).

16. Fernández-Guasti, M., Haro-Poniatowski, E., Diamant, R., Ponce, L. & Jiménez, E. Pulsed-laser deposition of selenium. *Journal of Materials Science* **30,** 6253–6256. ISSN: 00222461 (1995).

17. Chiera, N. M., Eichler, R., Vögele, A. & Türler, A. Vapor deposition coating of fused silica tubes with amorphous selenium. *Thin Solid Films* **592,** 8–13. ISSN: 00406090. arXiv: 9809069v1 [arXiv:gr-qc]. http://dx.doi.org/10.1016/j.tsf.2015.08.043 (2015).

18. Pejova, B. & Grozdanov, I. Solution growth and characterization of amorphous selenium thin films: Heat transformation to nanocrystalline gray selenium thin films. *Applied Surface Science* **177,** 152–157. ISSN: 01694332 (2001).

19. Patil, A. M., Kumbhar, V. S., Chodankar, N. R., Lokhande, A. C. & Lokhande, C. D. Electrochemical behavior of chemically synthesized selenium thin film. *Journal of Colloid and Interface Science* **469,** 257–262. ISSN: 10957103. http://dx.doi.org/10.1016/j.jcis.2016.02.030 (2016).

20. Dobson, D. C., James, F. C., Safarik, I., Gunning, H. E. & Strausz, O. P. Photolysis of hydrogen selenide. *Journal of Physical Chemistry* **79,** 771–775. ISSN: 00223654 (1975).

21. Kaplow, R., Rowe, T. A. & Averbach, B. L. Atomic arrangement in vitreous selenium. *Physical Review* **168,** 1068–1079. ISSN: 0031899X (1968).

22. Kim, K. S. & Turnbull, D. Crystallization of amorphous selenium films. I. Morphology and kinetics. *Journal of Applied Physics* **44,** 5237–5244. ISSN: 00218979 (1973).

23. Kim, K. S. & Turnbull, D. Crystallization of amorphous selenium films. II. Photo and impurity effects. *J. Appl. Phys.* **45,** 3447–3452. http://ieeexplore.ieee.org/xpls/abs_all.jsp?arnumber=5100908 (1974).

24. Chaudhuri, S., Biswas, S. K., Choudhury, A. & Goswami, K. Amorphous to crystalline transition of selenium thin films of different thicknesses. *Journal of Non-Crystalline Solids* **46,** 171–179. ISSN: 00223093 (1981).

25. Zvára, I. Simulation of Thermochromatographic Processes by the Monte Carlo Method. *Radiochimica Acta* **38,** 95–102. ISSN: 21933405 (1985).

26. Stephens, R. B. Stress-enhanced crystallization in amorphous selenium films. *Journal of Applied Physics* **51,** 6197–6201. ISSN: 00218979 (1980).

27. Goldan, A. H. *et al.* Molecular structure of vapor-deposited amorphous selenium. *Journal of Applied Physics* **120.** ISSN: 10897550 (2016).

28. Bellissent, R. Short range order in the disordered states of selenium-tellurium mixtures. *Nuclear Instruments and Methods In Physics Research* **199,** 289–294. ISSN: 01675087 (1982).

29. International Center for Diffraction Data. *JCPDS 06-0362* 2021.

3 Inverse Thermochromatography of the Hg-Se System

Paper Title: Inverse Thermochromatography of the Hg-Se System to Determine Reaction Kinetics

Authors: P. Ionescu[a,b], R. Eichler[b], A. Türler[a]

[a]University of Bern, 3012 Bern, Switzerland

[b]Paul Scherrer Institute, 5232 Villigen, Swizerland

To be submitted to the *Journal of Radioanalytical and Nuclear Chemistry*.

Author Contribution: All authors contributed to the study conception and design. Material preparation, data collection and analysis were performed by P. Ionescu. The first draft of the manuscript was written by P. Ionescu and all authors commented on previous versions of the manuscript.

3.1 Abstract

The novel method of inverse thermochromatography was introduced. A positive temperature gradient applied to the gas chromatography column increases the reaction rate of the mobile-stationary phase system over the length of the column. The carrier-free single-atom radioactive $^{197m,\ 203}$Hg reacts with the *t*-Se stationary phase and is quantified along the column using γ-ray spectrometry giving an internal chromatogram. A microscopic Monte-Carlo simulation is used to describe the motion of the tracer in the column, using the Eyring-Polanyi and Arrhenius equation respectively to describe the reaction rate of the system. A Gibbs free energy for the HgSe formation of $\Delta G^{\ddagger}(\mathrm{HgSe}) = 95 \pm 12$ kJ/mol was determined, and an activation energy of $E_a(\mathrm{HgSe}) = 100 \pm 10$ kJ/mol with Arrhenius pre-exponential factor of $A = 4.3 \cdot 10^{13} \pm 2.6 \cdot 10^{13}$ s^{-1}. The results were used to empirically extrapolate the group 12 elements to the superheavy

element copernicium (Z = 112) which has a predicted E_a(CnSe) = 106 ± 22 kJ/mol.

3.2 Introduction

The principal aim of this work was to determine the reaction kinetics of the mercury-selenium system and to serve as a preliminary chemical study for mercury's Superheavy Element (SHE) homolog copernicium (Cn, Z = 112). The electronic structure and therefore the chemistry of SHEs is influenced by the high nuclear charge and scales with the number of protons [1, 2]. Cn is suspected, despite its group 12 position in the periodic table, to share strong similarities with a noble gas [3, 4]. This postulation led chemists to design a Thermochromatography (TC) where the adsorption characteristics of Cn, its lighter homolog Hg and the noble gas Rn were directly compared [5]. In recent years, first chemistry experiments with Cn and Fl (Z = 114) were performed, the heaviest elements characterized using Gas Chromatography (GC) to date [5, 6]. In these experiments, the adsorption behaviour $-\Delta H_{ads}^{Au}$ of the three species on gold was established Rn < Cn < Hg, confirming the increased noble gas-like behaviour of Cn while still retaining group 12 characteristics. The adsorption enthalpy of Cn on Au was found to be $-\Delta H_{ads}^{Au}(Cn) = 52^{+4}_{-3}$ kJ/mol [5]. To deepen our understanding of the chemistry of Cn, a follow-up GC experiment was designed using elemental Se-covered detectors as a chromatographic surface. Preliminary results were ambiguous, requiring better control over the Se allotropy and deeper understanding of its interaction with Hg [7].

Selenium is only second to sulfur in the number of allotropes it can form [8, 9]. Different allotropes can behave chemically distinct and GC experiments with Hg set the $-\Delta H_{ads}^{a-Se}(Hg) =$ 85 kJ/mol and $-\Delta H_{ads}^{t-Se}(Hg) = 60$ kJ/mol for amorphous and crystalline trigonal selenium respectively [10]. The first Cn experiment was designed with the more reactive a-Se and encountered difficulties due to spontaneous crystallization of the chromatographic surface to t-Se. The ambiguous surface identity and low statistics resulted in inconclusive results. To eliminate the uncertainty, the GC was repeated with t-Se as the stationary phase. Additional off-line experiments with the Hg-Se system to better understand this interaction were also performed. These off-line experiments revealed a heterogeneous nature of the t-Se surfaced due to open-ended t-Se chains (see Chapter 3).

Hg is known to form HgSe and can be found naturally occurring as the mineral tiemannite, discovered in 1852 [11, 12]. At Standard Temperature and Pressure (STP), Hg will not readily react with t-Se, and only adsorb weakly, prompting us to design an inverse TC to study this reaction closely at the tracer level using the Hg radioisotopes ^{197m}Hg and ^{203}Hg. As the Hg tracer is carried by the mobile phase through the t-Se column with a positive temperature gradient it interacts with the stationary phase in a repeated adsorption-desorption process. As the temperature increases, the reaction rate between mobile and stationary phase begins to surpass the rate of desorption, therefore allowing a reaction. This results in an internal chromatogram (deposition pattern) in the column, measurable by γ-ray spectroscopy. This is to our knowledge the first use of an inverse thermochromatography (positive temperature gradient) for the determination of reaction kinetics in a system.

The deposition pattern obtained in the inverse chromatography was then simulated using a microscopic Monte-Carlo Simulation (MCS) pioneered by Zvára [5, 13] and modified to account for the heterogeneous t-Se surface [10]. Two methods were used to model the formation of HgSe; An implementation of the Eyring-Polanyi equation to describe the HgSe formation from transition state theory via the Gibbs free energy of activation, $\Delta G^{\ddagger}$ [14, 15], and the empirical Arrhenius equation which uses the activation energy, E_a. It is assumed that as the Hg travels through the column and adsorbs to the Se surface, it will either desorb, or overcome the activation barrier and form HgSe (Figure 34).

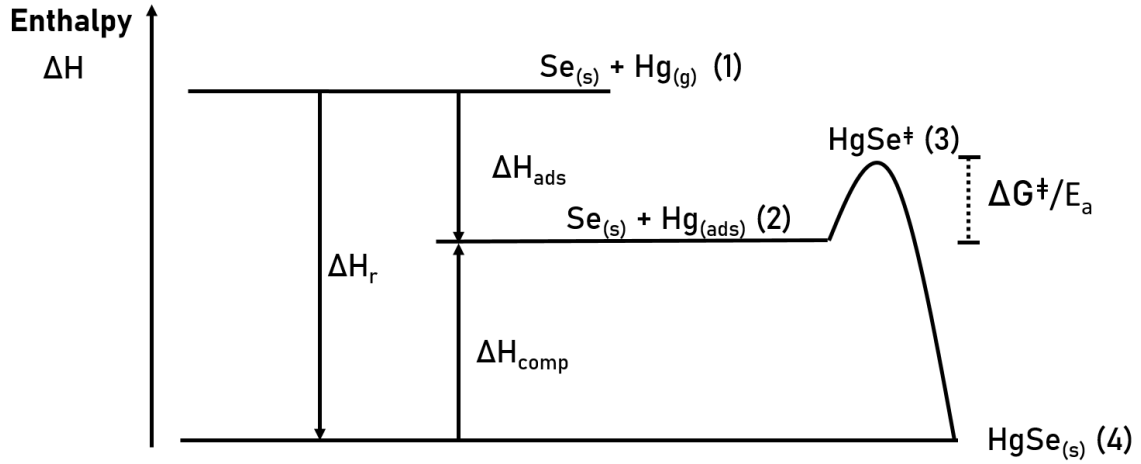

Figure 34: Energy diagram illustrating the Hg-Se system. ΔH_r, the enthalpy of reaction from state (1) to form (4) contains the ΔH_{ads} to adsorb gaseous Hg, minus the enthalpy ΔH_{comp}, the energy required to break bonds and promote Hg from HgSe to the adsorbed state on the surface. In this case, we postulate that in order to form the final product HgSe, the adsorbed Hg must first overcome an energy barrier through the $HgSe^{\ddagger}$ transition state (3) defined by $\Delta G^{\ddagger}$, or E_a depending on the model chosen. Note that $\Delta G^{\ddagger}$ is not equal to E_a, they are merely represented by the same schematic.

The reaction is taken to be irreversible. The mean time a tracer is adsorbed to the surface of the chromatographic column for each collision, t_m is given by reaction 35 [13].

$$t_m = \frac{1}{\upsilon_0} e^{\frac{\Delta H_{ads}}{T}} \tag{35}$$

where υ_0 is the lattice phonon frequency of Se, ΔH_{ads} is the adsorption enthalpy, and T is the temperature of the column surface.

To better describe single-atoms on a microscopic scale, a real time is randomly assigned to a tracer for each adsorption according to a logarithmic distribution:

$$t_a = t_m \cdot -log(x) \tag{36}$$

where x is a random mumber between 0 and 1.

3.2.1 Transition State Theory Approach using Eyring-Polanyi Equation

The Eyring-Polanyi equation is given by 37 [15]:

$$k_e = \kappa \frac{k_b T}{h} \cdot e^{\frac{-\Delta G^{\ddagger}}{RT}} \tag{37}$$

where k_e is the rate of the reaction, κ the transmission coefficient, k_b the Boltzmann constant, T the temperature, h the Planck constant, $\Delta G^{\ddagger}$ the Gibbs free energy of activation, and R the gas constant. As this represents the forward reaction rate, the reciprocal is used to simulate a random time for the reaction to occur, t_f, on a microscopic basis (equation 38):

$$t_f = \frac{1}{k_e} \cdot -log(x) \tag{38}$$

where x is a random number between 0 and 1.

From Zvára's publication, each tracer encounter with the surface experiences a series of adsorption-desorption events [13] (see Chapter 3). For each of these adsorptions, the forward reaction time is compared to the time each Hg tracer resides at the adsorption site; if the reaction proceeds forward ($t_f < t_a$), HgSe formation has occurred and the next atom is simulated (Figure 35). Both the adsorption- and reaction times are randomised according to a logarithmic distribution to better describe the tracer on a microscopic single-atom scale. The two unknown parameters κ and $\Delta G^{\ddagger}$ are varied iteratively in the simulation until a best fit is found for our experimental data. The transmission coefficient κ is generally taken to be $0.9 \leq \kappa \leq 1$ and represents the probability of the reaction successfully taking place [15].

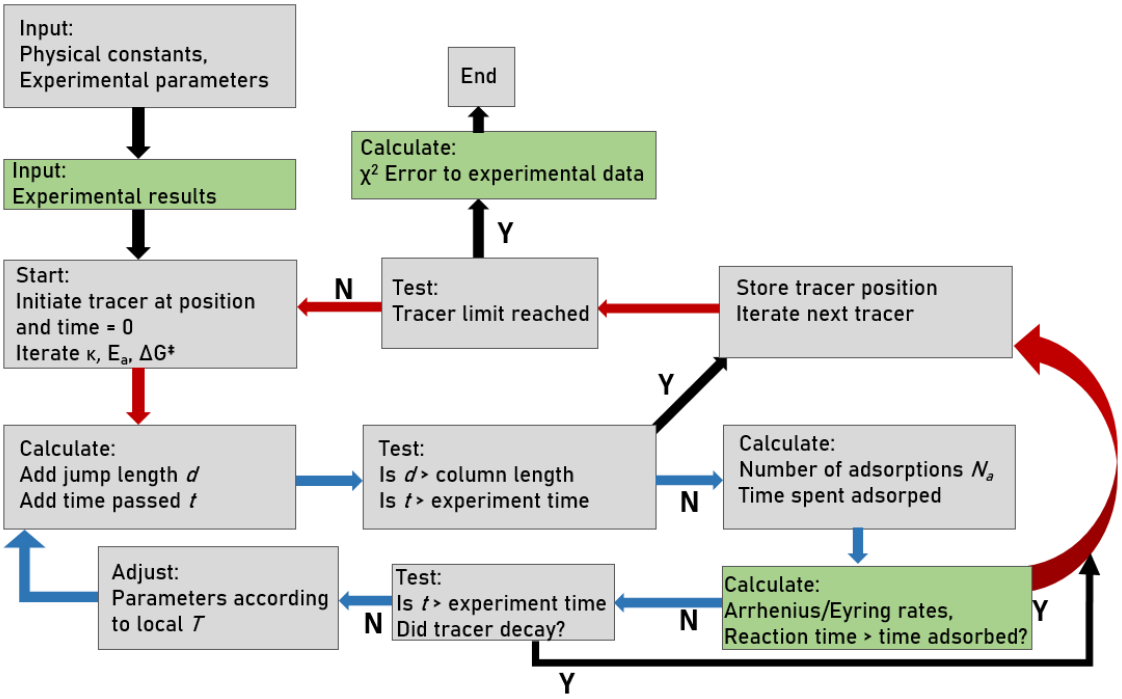

Figure 35: Simplified program flowchart of the MCS used to describe a TC. Grey boxes represent the core program used, green boxes are additions in this work. The initial experiment parameters are put into the system, allowing the program to simulate one atom at a time progressing through the column. The loop experienced by an individual tracer is represented by blue arrows. The loop iterating parameters to fit experimental data is given by red arrows. Various conditions are set to end the particle loop such as decaying in-flight, reacting with the surface or exiting the column thus triggering the next iteration of tracer.

3.2.2 Activation Energy Determination using Arrhenius Equation

Similar to the Eyring-Polanyi approach, the reaction rate was calculated using the Arrhenius equation (Eq. 39), then compared to the adsorption time of the tracer [16].

$$k_a = A \cdot e^{\frac{-E_a}{RT}} \tag{39}$$

where k_a is the rate of reaction, A the pre-exponential factor, and E_a the activation energy. The forward reaction time t_f is again taken from a logarithmic distribution (equation 40):

$$t_f = \frac{1}{k_a} \cdot -log(x) \tag{40}$$

where x is a random number between 0 and 1.

If during the MCS the reaction time t_f becomes sufficiently fast to allow HgSe formation while it is adsorbed, the tracer will react forming HgSe ($t_f < t_a$). Again, equation 35 is weighed against the reaction rate. Both parameters are logarithmically randomly distributed to simulate individual atoms on the microscopic scale. Here, the two unknown parameters iterated are A and E_a, where $A \approx 10^{13} s^{-1}$ as this is a range commonly set for monomolecular surface reactions [17, 18].

3.3 Experimental Setup

3.3.1 Radioisotope Tracer Production

Carrier-free ^{197m}Hg ($t_{1/2}$ = 23.8 h, main γ-line 33% 133.99 keV) radioisotope was obtained using the Injector II cyclotron of the High Intensity Proton Accelerator (HIPA) facility at the Paul Scherrer Institute by 60 MeV proton irradiation of a gold foil (99.95% purity, 0.1 mm thickness, ⌀ 19 mm) using reaction 41:

$$^{\text{nat}}\text{Au}(p, n)^{197m}\text{Hg} \tag{41}$$

For the production of ^{203}Hg (t_{1_2} = 46.6 days, main γ-line 81% 279.20 keV), thallium granules (Sigma-Aldrich, 99.99%) were heated in a tube furnace under nitrogen stream to remove any possible Hg impurities. The granules were then cooled and irradiated using fast neutrons at the Swiss Spallation Neutron Source (SINQ) facility at PSI, Switzerland via reaction 42.

$$^{nat}\mathrm{Tl}(n,p)^{203}\mathrm{Hg} \tag{42}$$

3.3.2 Inverse Thermochromatography

The method for preparing Physical Vapor Deposition (PVD) t-Se coated on rectangular substrates was described in detail in the previous chapter (Chapter 3). Inverse TC was performed using the setup pictured in Figure 36. A He stream (99.9990 vol% purity) through a fused quartz tube transported the tracer to a copper channel with a rectangular trench for the 16 t-Se covered substrates. Hg was not allowed to come into contact with the copper channel through a Teflon inlay. Any exposed copper was additionally covered in a layer of Fluorinert® FC-40 (Sigma-Aldrich) to passivate the surface.

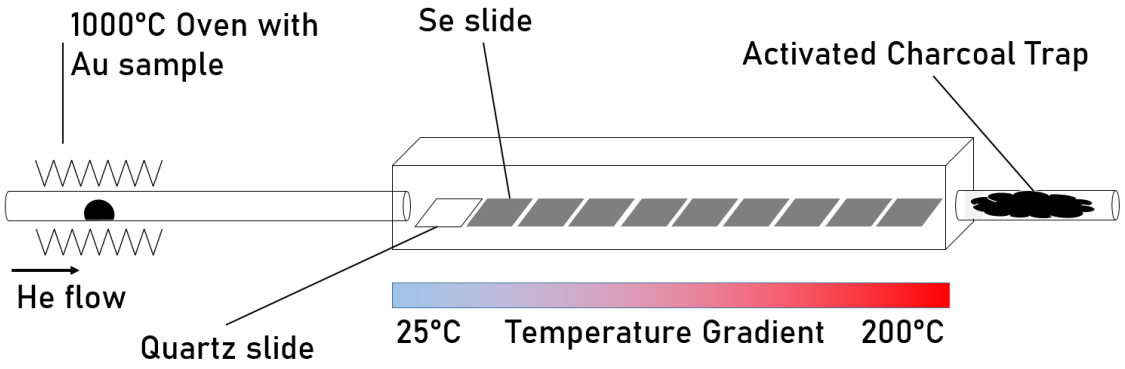

Figure 36: Schematic of the TC setup used to determine the deposition pattern of Hg on Se. An irradiated Au sample with trace Hg is heated to 1000°C in a starter oven and a He mobile phase carries the tracer to the chromatographic column containing an array of 16 t-Se coated slides over a temperature gradient. The t-Se coating is one-sided while the remainder of the column was coated in Teflon™. Any unreacted Hg was caught in an activated charcoal trap.

The first quartz slide was not covered in t-Se to ensure no deposition was occurring due to contaminants. A temperature gradient from room temperature to 200°C, close to the melting point of selenium was applied over the heat-conductive copper and the temperature was mon-

itored using three thermocouples. To ensure no escape of radioactive tracers, any unreacted Hg was captured on an activated charcoal trap at the exit of the chromatographic column. After the GC, the system was allowed to cool and the Hg activity of individual quartz slides was measured on a high-purity germanium (HPGe) γ-ray detector (Ortec GEM-23185) to construct an internal chromatogram. In all experiments the activity of the gold foil was measured before and after heating. All normalized measurements in internal chromatograms are based on the total activity introduced from the gold foil to ensure no tracers were retained on it.

3.4 Results and Discussion

3.4.1 The Gibbs Free Energy of Activation of Mercury Selenide

Figure 37 shows a typical deposition pattern of an inverse TC with ^{197m}Hg on t-Se.

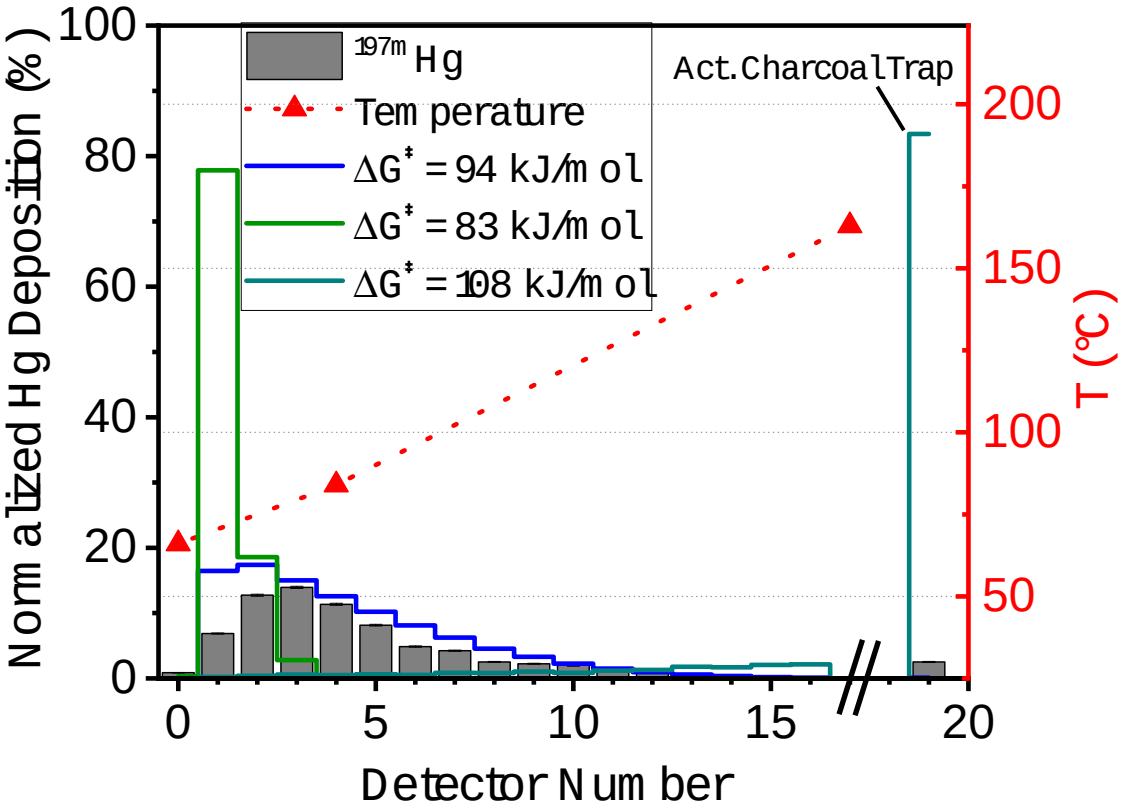

Figure 37: Normalized deposition of Hg in a *t*-Se coated rectangular chromatographic column measured by γ-ray spectrometry (grey bars) with temperature gradient (red line). Line break in axis shows end of the chromatographic channel. The three stepped lines show MCSs with different Gibbs free energies of activation to highlight the effect on the deposition pattern. $\kappa = 0.95$, $-\Delta H_{ads}^{t-Se} = 60$ kJ/mol, 50 ml/min He flow.

The MCS demonstrates the effect of $\Delta G^{\ddagger}$ on the deposition pattern. A lower value means that the energy barrier for HgSe formation is low, resulting in many ^{197m}Hg atoms bonding irreversibly within the first section of the column with a sharp peak. With a higher $\Delta G^{\ddagger}$, fewer ^{197m}Hg atoms have the required energy to overcome the barrier, and most desorb. They subsequently interact with the surface on multiple occasions, thus spreading the deposition over a wider area.

A chi-squared test was performed to find the optimal parameters for κ and $\Delta G^{\ddagger}$ for each simulation (Figure 38).

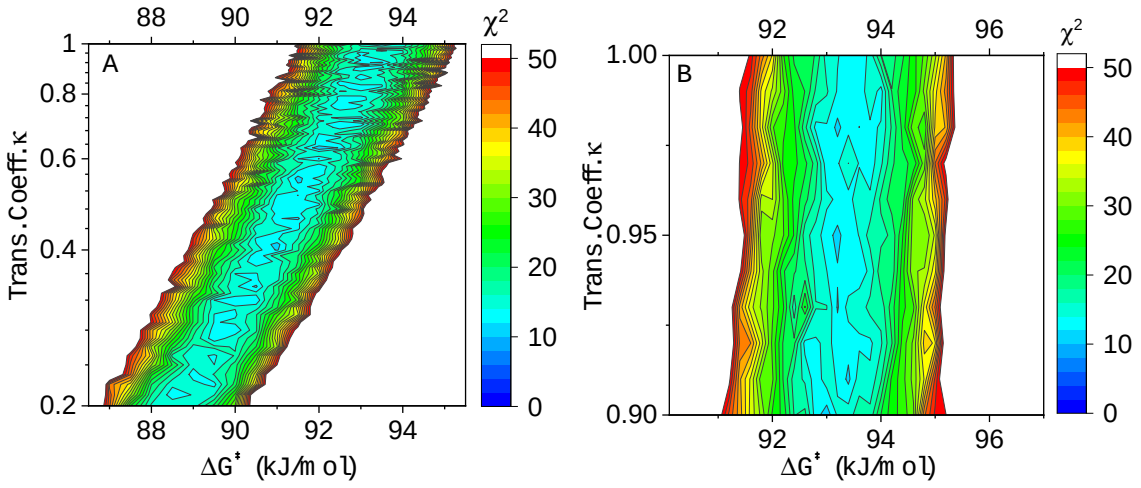

Figure 38: **A** Heat map showing the chi-squared minimization for optimized parameters $\Delta G^{\ddagger}$ and κ for HgSe formation using the Eyring-Polanyi equation. Even over a wide range of κ, $\Delta G^{\ddagger}$ does not change by more than 10%. **B** Higher resolution search, as κ is generally taken between 0.9 - 1.

Even over a wide range of κ, there is little influence on the resulting Gibbs free energy (within $\pm$ 10 %). Ultimately the search was constricted to $0.9 \leq \kappa \leq 1$ as this range showed the lowest deviation from experimental data and is also commonly cited as an appropriate value [15]. The experiment was repeated four times (Table 5). For the formation of HgSe a $\Delta G^{\ddagger} = 95 \pm 12$ kJ/mol[9] with $\kappa = 0.95 \pm 0.04$ was discovered. It is noteworthy that in this system $\Delta G^{\ddagger}$(HgSe) = 95 kJ/mol > $-\Delta H_{ads}^{t-Se}$(Hg) = 60 kJ/mol, meaning that the system with sufficient energy to react always has sufficient energy to desorb; only as the temperature increases, the reaction becomes sufficiently fast to surpass the rate of desorption.

Table 5: $\Delta G^{\ddagger}$ and κ values determined with a summary (95% confidence interval).

Experiment	$\Delta G^{\ddagger}$ (kJ/mol)	κ
1	94	0.95
2	90	0.91
3	94	0.91
4	104	0.92
Overall	95 $\pm$ 12	0.95$\pm$ 0.04

3.4.2 Application in Chromatographic Columns of Cylindrical Geometry

When changing the geometry of a chromatographic channel, the number of surface interactions can vary [19]. This is particularly true when comparing a one-sided rectangular chromatographic channel to a cylindrical one. To test the accuracy of the established Gibbs free energy, we repeated the thermochromatography in a cylindrical column with a round cross section (Figure 39).

[9] 95% confidence interval.

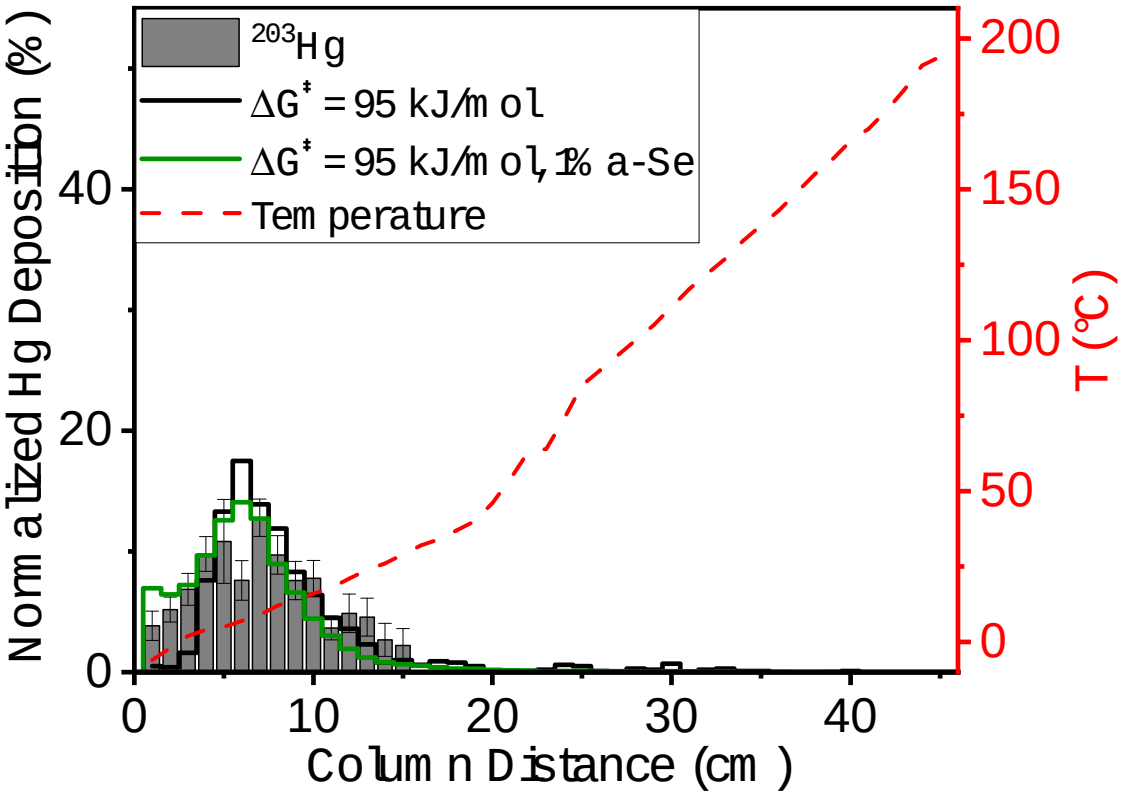

Figure 39: Inverse TC on cylindrical *t*-Se column showing the temperature gradient (red line) and ^{203}Hg deposition measured with γ-ray spectrometry. MCS with $\Delta G^{\ddagger}$ = 95 kJ/mol, $\kappa = 0.95$ (black line), and MCS with identical conditions, but a 1% coverage of reactive *a*-Se sites on the surface (green line). 25 ml/min He flow, -ΔH_{ads}^{t-Se}(Hg) = 60 kJ/mol, -ΔH_{ads}^{a-Se}(Hg) = 85 kJ/mol. $\varnothing_{inner} = 4$ mm.

Figure 39 shows at the established value of $\Delta G^{\ddagger}$(HgSe) = 95 kJ/mol, there is a very good agreement with the ^{203}Hg deposition measured by γ-ray spectrometry. The deposition temperature of the peak observed in the cylindrical columns is lower than that of the rectangular single-sided channel ($T_{round} \approx 10$°C, $T_{rectangular} \approx 80$°C). The likely reason for this is due to the geometry of the column; a tracer in a one-sided rectangular chromatographic column will encounter a *t*-Se surface much less likely than in a round column. Therefore, a tracer in a round column has significantly more opportunities to react with the column surface. It was previously established, that in *t*-Se a small amount of more reactive sites are often present, depending on the degree of crystallization (see previous chapter). Figure 39 also shows the

deposition pattern with a 1% *a*-Se coverage of the chromatographic surface as is common in *t*-Se GC columns. In both cases, the simulation gives good agreement with the experimentally determined internal chromatogram.

3.4.3 The Arrhenius Activation Energy of Mercury Selenide

The thermochromatography experiments above were also evaluated using the Arrhenius equation equation within the MCS.

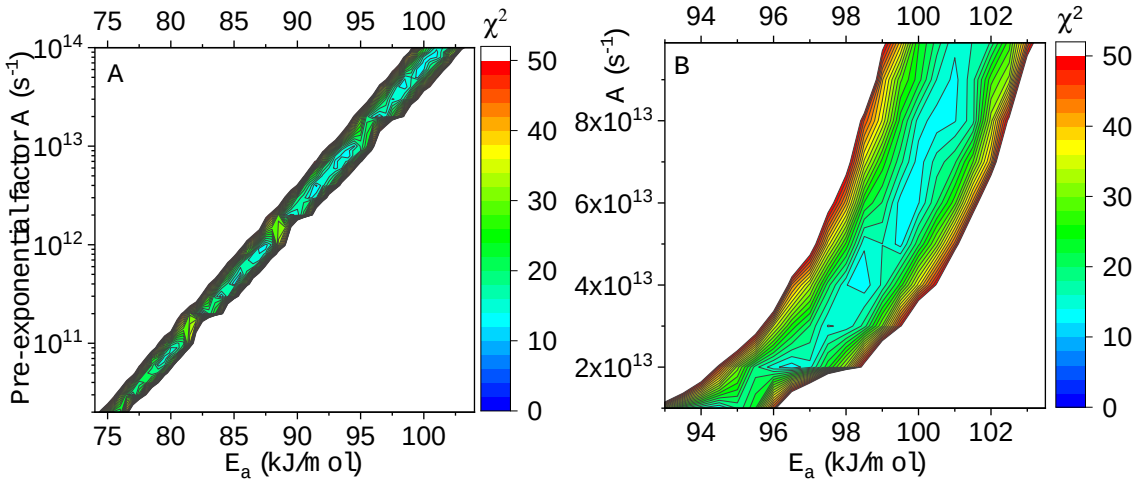

Figure 40: **A** Heat map showing the chi-squared test reaching a minimum above pre-exponential factor value of $A \approx 10^{13}\ s^{-1}$. **B** Heat map magnified in the low-error region showing the optimized parameters for E_a and A in the Arrhenius equation.

The parameters for the best fit were found to be $E_a = 100 \pm 10$ kJ/mol and $A = 4.3 \pm 2.6 \cdot 10^{13}$ s^{-1}. Figure 40 shows the optimal fit approaches a minimum with respect to the pre-exponential factor A in the 10^{13} s^{-1} range as is expected for a monomolecular reaction.

Table 6: E_a and A values determined with a summary. (*a*) 95% confidence interval. (*b*) 68% confidence interval.

Experiment	E_a (kJ/mol)	A ($\cdot 10^{13}$, s^{-1})
1	101	7
2	96	6
3	97	2
4	107	2
Overall	100 ± 10^a	4.3 ± 2.6^b

3.4.4 Extrapolation to Copernicium

The scope of this work was the determination of the reaction kinetics for the Hg-Se system as a preliminary study for the element copernicium. SHEs are chemically investigated in context of their lighter homologs and trends in the periodic system. The trend is made by correlating the activation energy to the sublimation enthalpy $\Delta H_f^{298}(M_{(g)})$, where M = Zn, Cd and Hg. The sublimation enthalpy is commonly used as a basis for such trends, as it is affected by relativistic effects on electron shells and therefore accounts for them. The determination of E_a for the reaction between Hg and Se thus allowed us to extrapolate the value for Cn (Figure 41).

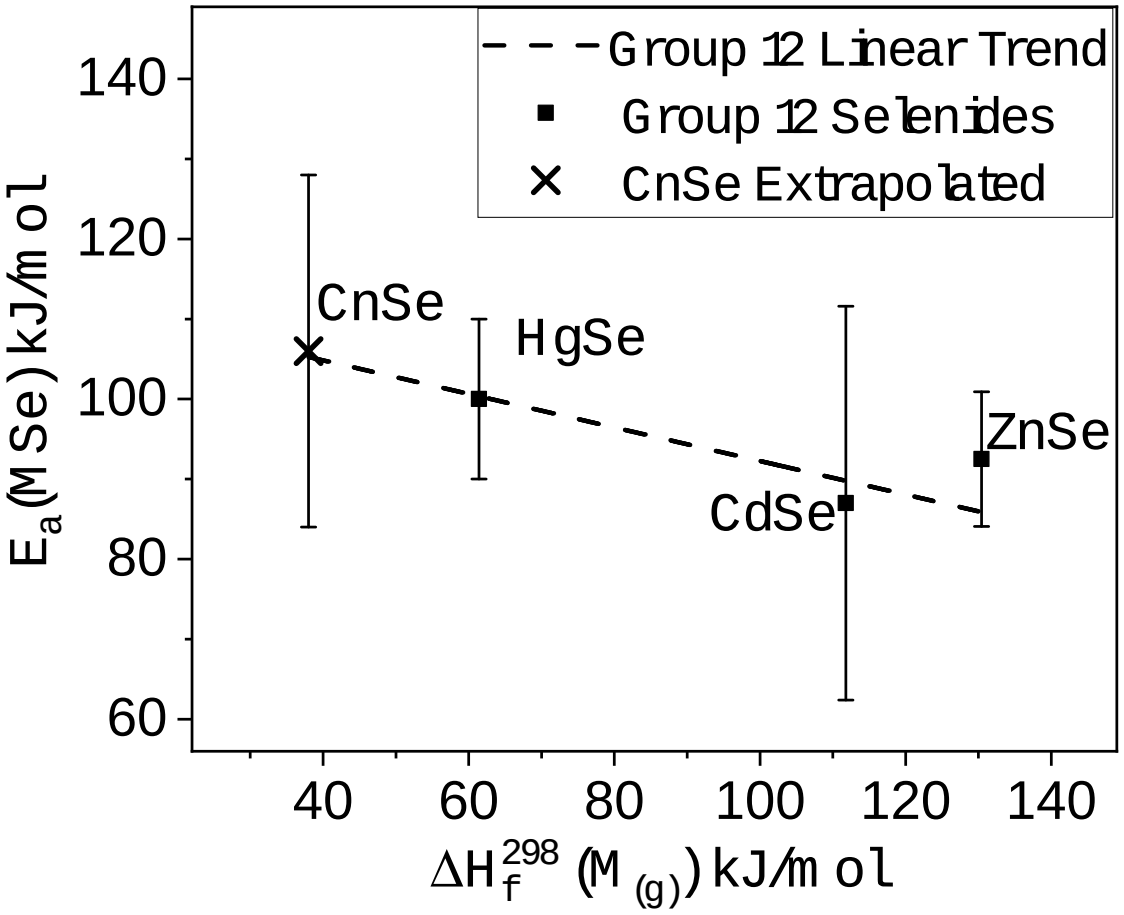

Figure 41: Activation energy trend in group 12 selenide formation correlated to the metal's sublimation enthalpy extrapolated to Cn (Z = 112). The error bars for Cn are the standard error of the linear extrapolation. Data for ZnSe from [20], CdSe from [21].

The empirically extrapolated value for the reaction between Cn and Se is $E_a \approx 106 \pm 22$ kJ/mol, making $E_a(CnSe) > E_a(HgSe)$. This assumption is speculative, however it can have significant consequences for future GC investigations of the Cn-Se system; copernicium has shown increased noble gas-like character in previous experiments [5, 6], and the trend presented in Figure 41 continues to support that hypothesis. It has, however, also been suggested that for the selenium interaction, there is a reverse trend where the strong destabilization of the 6*d* orbitals as a consequence of relativistic effects makes copernicium more reactive than mercury [22, 23]. This extrapolation does not support an increased reactivity of copernicium. Despite these findings, past copernicium experiments have shown an unexpected deposition of

copernicium atoms on *t*-Se, requiring further investigation.

3.5 Conclusions

We have performed inverse thermochromatography experiments using single-atom Hg radioisotopes as a tracer on a *t*-Se stationary phase. Against a positive temperature gradient, the increasing reaction rate begins to favour $HgSe_{(s)}$ formation over desorption. We modelled the resulting deposition pattern using a microscopic Monte-Carlo simulation implementing the Eyring-Polanyi equation which resulted in a $\Delta G^{\ddagger} = 95 \pm 12$ kJ/mol with $\kappa = 0.95 \pm 0.04$ for the formation of the transition state and successful forward reaction respectively. In similar fashion, the system was also modelled using the Arrhenius equation, which gave $E_a = 100 \pm 10$ kJ/mol and $A = 4.3 \cdot 10^{13} \pm 2.6 \cdot 10^{13}\ s^{-1}$. This value was used to extrapolate an activation energy trend in group 12 elements reacting with selenium using literature data. The trend supports the predicted behaviour that copernicium at $E_a = 106 \pm 22$ kJ/mol shows decreased reactivity to selenium when compared to mercury.

References

1. Pyykko, P. & Desclaux, J. P. Relativity and the Periodic System of Elements. *Accounts of Chemical Research* **12,** 276–281. ISSN: 15204898 (1979).
2. Fricke, B. in *Struct. Bonding* J. D. Duni, 89–144 (Springer, Berlin, 1975).
3. Pitzer, K. S. Are elements 112, 114, and 118 relatively inert gases? *The Journal of Chemical Physics* **63,** 1032–1033. ISSN: 00219606 (1975).
4. Mewes, J. M., Smits, O. R., Kresse, G. & Schwerdtfeger, P. Copernicium: A Relativistic Noble Liquid. *Angewandte Chemie - International Edition* **58,** 17964–17968. ISSN: 15213773 (2019).
5. Eichler, R. *et al.* Thermochemical and physical properties of element 112. *Angewandte Chemie - International Edition* **47,** 3262–3266. ISSN: 14337851 (2008).

6. Eichler, R. *et al.* Chemical characterization of element 112. *Nature* **447,** 72–75. ISSN: 0028-0836. http://www.nature.com/doifinder/10.1038/nature05761 (2007).

7. Chiera, N. M. *Towards the Selenides of the Superheavy Elements Copernicium and Flerovium* PhD thesis (University of Bern, 2016).

8. Steudel, R. & Eckert, B. in *Topics in Current Chemistry* 1–80 (Springer, Berlin, Heidelberg, 2003).

9. Olin, Å., Noläng, B., Öhman, L., Osadchii, E. & Rosén, E. Chemical Thermodynamics Volume 7: Chemical thermodynamics of selenium. *Chemical Thermodynamics* **7,** 851. http://www.diva-portal.org/smash/record.jsf?pid=diva2:154431 (2005).

10. Chiera, N. M. *et al.* Interaction of elemental mercury with selenium surfaces: model experiments for investigations of superheavy elements copernicium and flerovium. *Journal of Radioanalytical and Nuclear Chemistry* **311,** 99–108. ISSN: 15882780 (2017).

11. Cabral, A. R. *et al.* Clausthalite (PbSe) and tiemannite (HgSe) from the type locality: New observations and implications for metallogenesis in the Harz Mountains, Germany. *Ore Geology Reviews* **102,** 728–739. ISSN: 01691368. https://doi.org/10.1016/j.oregeorev.2018.09.027 (2018).

12. Kerl, B. Ueber ein neues Vorkommen von Selen- quecksilber. *J. Prakt. Chem.* **57,** 470–476 (1852).

13. Zvára, I. Simulation of Thermochromatographic Processes by the Monte Carlo Method. *Radiochimica Acta* **38,** 95–102. ISSN: 21933405 (1985).

14. Eyring, H. The Activated Complex in Chemical Reactions. *Journal of Chemical Physics* **3,** 107–115 (1935).

15. Ašperger, S. *Chemical Kinetics and Reaction Mechanisms* 2nd, 14–25. ISBN: 9781461348719 (Croatian Academy of Sciences and Arts, Zagreb, 2003).

16. Hollemann, A., Wiberg, E. & Wiberg, N. *Lehrbuch der Anorganischen Chemie* 102nd ed., 188–189 (Walter de Gruyter, Berlin, 2007).

17. Zhdanov, V. P. Arrhenius parameters for rate processes on solid surfaces. *Surface Science Reports* **12,** 185–242. ISSN: 01675729 (1991).

18. Preexponential factors in surface reactions. *Journal of Catalysis* **45,** 94–105. ISSN: 10902694 (1976).

19. Poppe, H. Mass transfer in rectangular chromatographic channels. *Journal of Chromatography A* **948,** 3–17. ISSN: 00219673 (2002).

20. Mitsuhashi, H., Mitsuishi, I. & Kukimoto, H. Growth kinetics in the MOVPE of ZnSe on GaAs using zinc and selenium alkyls. *Journal of Crystal Growth* **77,** 219–222. ISSN: 00220248 (1986).

21. Synthesis kinetics of CdSe quantum dots in trioctylphosphine oxide and in stearic acid. *Applied Physics Letters* **86,** 1–3. ISSN: 00036951 (2005).

22. Chiera, N. M. *Towards the Selenides of the Superheavy Elements Copernicium and Flerovium* PhD thesis (University of Bern, 2016), 170–174.

23. Pershina, V., Bastug, T., Jacob, T., Fricke, B. & Varga, S. Intermetallic compounds of the heaviest elements: The electronic structure and bonding of dimers of element 112 and its homolog Hg. *Chemical Physics Letters* **365,** 176–183. ISSN: 00092614 (2002).

4 Evidence of a Reaction between Copernicium and Selenium

4.1 Introduction

The study of man-made Superheavy Element (SHE) is particularly rewarding in the discovery of fundamental properties of the elements at the very limit of stability against spontaneous fission. The Island of Stability predicted in 1966 [1] set a target for SHE synthesis with the promise of longer half-lives. These increased lifetimes can make SHE more accessible for chemistry experiments, with the lower limit currently being $\approx$ 1 s [2]. Relativistic effects on the electron shells of atoms is an area of high interest and the heaviest elements due to their high nuclear charge are most affected, which is why they are typically studied in comparison to their lighter homologs [3]. Relativistic effects on electron shells become much more pronounced as they scale with the atomic number, but already affect even commonly known elements such as mercury and gold [4–11]. Generally speaking, relativity directly affects the s- and $p_{1/2}$-orbitals by stabilizing them. The secondary, indirect effect is a consequence of this stabilization causing the destabilization of $p_{3/2}$-, d- and f-electrons [5, 12]. Valence electron binding energies are affected and thus symmetry of the atomic orbitals which defines the chemical behaviour of an element. Familiar trends in the periodic table such as periodicity can become perturbed when relativity begins to affect chemistry. It has been shown for example that SHEs seaborgium, bohrium and hassium behave typically for their respective groups [12–16].

In contrast, copernicium (Z = 112) as a member of group 12 in the periodic table has a postulated closed-shell ground-state electron configuration of [Rn]$5f^{14}6d^{10}7s^2$ [17]. This electronic configuration under the influence of relativistic effects causing a contraction of the spherical $7s$- valence orbital was the basis for the prediction of Cn to be inert and volatile [18]. Therefore, Cn was thought to resemble a noble gas more closely rather than its lighter group 12 metal homologs. The first series of chemistry experiments with Cn investigated the predicted inert chemical behaviour by using the Cryo On-Line Detector (COLD) array gas Thermochro-

matography (TC) to comparatively determine the adsorption interaction with a gold stationary surface between Cn, its homolog Hg and the noble gas Rn [19]. The adsorption enthalpy on gold $-\Delta H_{ads}^{Au}$ compared between these elements revealed the trend Hg > Cn > Rn. Cn was confirmed to be, as predicted [20, 21], considerably more inert compared to its lighter homolog Hg [22, 23].

Building on this discovery, a second generation experimental campaign was launched, designed to compare the heaviest of the group 12 homologs on an isothermal trigonal selenium (*t*-Se) covered detector array at room temperature [24–26]. Hg is known to occur as the mineral tiemannite (HgSe) in nature [27, 28], and the element has been shown to readily adsorb to a stationary phase made up of the amorphous *a*-Se allotrope in previous studies [24], as well as in Chapter 3. The experiments were based on previous thermochromatographic investigations of a gold stationary phase. Cn was expected to show considerably less affinity to *a*-Se, based on experimental and theoretical findings further confirming its postulated noble gas-like behaviour. First experimental results were ambiguous due to inherent instability of the *a*-Se allotrope which spontaneously transformed to the more stable trigonal *t*-Se allotrope during the several weeks-long experimental campaign [24, 29–31]. The heterogeneous nature of the stationary phase made interpretation of observed ^{283}Cn decays ambiguous and it was concluded that the SHE encountered a largely (>97%) *t*-Se stationary phase. However, contrary to expectation, both decays were observed on the selenium surface. Independent of the selenium allotrope the ^{283}Cn encountered, its predicted inert nature implied there should be no significant interaction. The results strongly implied the previously established adsorption enthalpy trend -ΔH_{ads}^{Au} for the series Hg > Cn > Rn to be incorrect.

This experimental campaign was deliberately operated with a *t*-Se stationary phase to rule out a chemically unstable surface for a continuously running experiment that requires stable conditions for multiple weeks. A Monte-Carlo Simulation (MCS) based on the model by Zvára [32] modified to best describe this experimental setup was used to model and interpret experimental results. The aim was to critically investigate the copernicium-selenium interaction first reported in 2015 [25]. A series of preliminary experiments with the lighter homolog Hg were

performed in preparation to cement our understanding of the selenium stationary phase (see previous chapters 2 and 3). Additionally, as a result of the nuclear fusion evaporation reaction products recoiling directly into a recoil chamber, there are many reaction byproducts of which the volatile (at room temperature) ones can also reach the COLD array. ^{219}Rn is such a byproduct and is used along with its chain of decay products for calibrating the detector array, and as a reference for the adsorption of a volatile noble gas in the thermochromatography. Another such byproduct is ^{211}At, which due to its similar adsorption characteristics to Hg can also be evaluated to provide useful information about the state of the gas chromatography.

4.2 Experimental

4.2.1 The Cryo-Online Detector (COLD) Gas Chromatographic Loop

The TC loop was closely based on the setup described in previous experiments [19, 22, 23, 33]. A simplified schematic of the loop is shown in Figure 42.

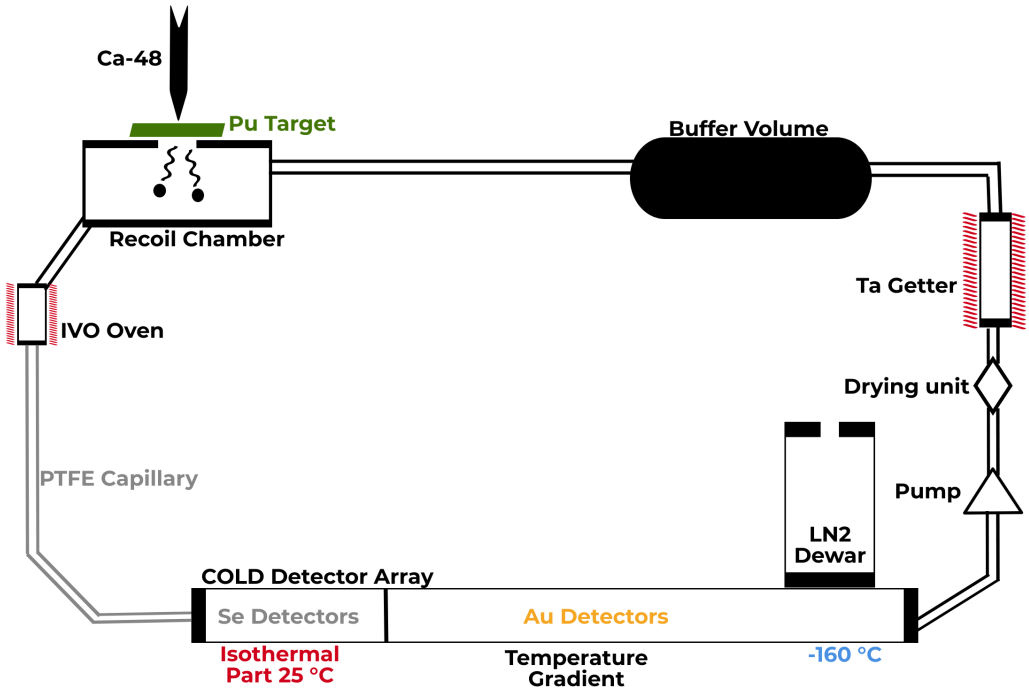

Figure 42: The COLD loop. Nuclear fusion reaction products are thermalized in a recoil chamber and transported by an inert carrier gas mixture (Ar/He 3:7) through an In-situ Volatilization Oven (IVO) acting as an aerosol filter. The volatile reaction products are transported via a PFTE capillary to the COLD array, with 8 *t*-Se covered PIN detector pairs in an isothermal section at 25°C, followed by 16 gold covered PIN detector pairs on a temperature gradient to ≈-160°C. The remainder of the loop is designed to purify the circulating carrier gas from contaminants.

A grid-supported (85% grid transmission) stationary $^{242}PuO_2$ and $^{nat}Nd_2O_3$ target admixture (1.4 ± 0.1 mg/cm^2 ^{242}Pu + 14 ± 1 μg/cm^2 ^{nat}Nd) was irradiated with a ^{48}Ca ion beam (233 - 244 MeV projectile energy in target[10]) at the U-400 cyclotron, at Flerov Laboratory of Nuclear Reactions (FLNR). An integral beam dose of $3.34 \cdot 10^{18}$ ^{48}Ca ions was accumulated on the target over a period of 26 days. The Nd was added to the target to co-produce $^{182-185}$Hg as a short-lived tracer. As a radionuclide whose chemical properties in this experimental setup is well-studied, $^{182-185}$Hg allows us to monitor the gas chromatography performance in real-time by observing changes in the internal chromatogram (deposition pattern), thus revealing the status of the stationary surface. The nuclear reaction products recoiled out of the target material and were thermalized in a recoil chamber connected to the gas chromatographic loop. The mobile phase inert gas mixture (He/Ar 7:3, 1.8 L/min) transported the reaction products through an In-situ Volatilization Oven (IVO) (850°C) with a quartz wool filter for removal of aerosols. The volatile reaction products then travelled through a 4 m long PFA capillary ($\varnothing_{inner}$ 1.6 mm, transport time = [x]) to the COLD array for chromatographic separation and detection. The carrier gas mixture was looped to achieve best possible purification from contaminants over a SICAPENT drying cartridge, a Ta getter (950°C) and a commercial gas purifying cartridge (SAES Microtorr 902F). The gas composition of the loop was constantly monitored using an atmospheric mass spectrometer (mks Cirrus 2) and a dew point meter (Mitchell Easydew).

[10]calculated with TargetSE

4.2.2 The Cryo-Online Detector array

The method used to coat Positive Implanted N-type (PIN) diodes for use as $\alpha-$ and SF detectors with thin *t*-Se films (80% coverage) is described in detail in chapter 3. The individual *t*-Se coated PIN diodes (8 x 8 mm^2 covered area, 250 nm thickness) were soldered facing each other forming a 'sandwich' two-sided rectangular gas chromatographic channel of 1.2 x 12 mm cross-section (Figure 43).

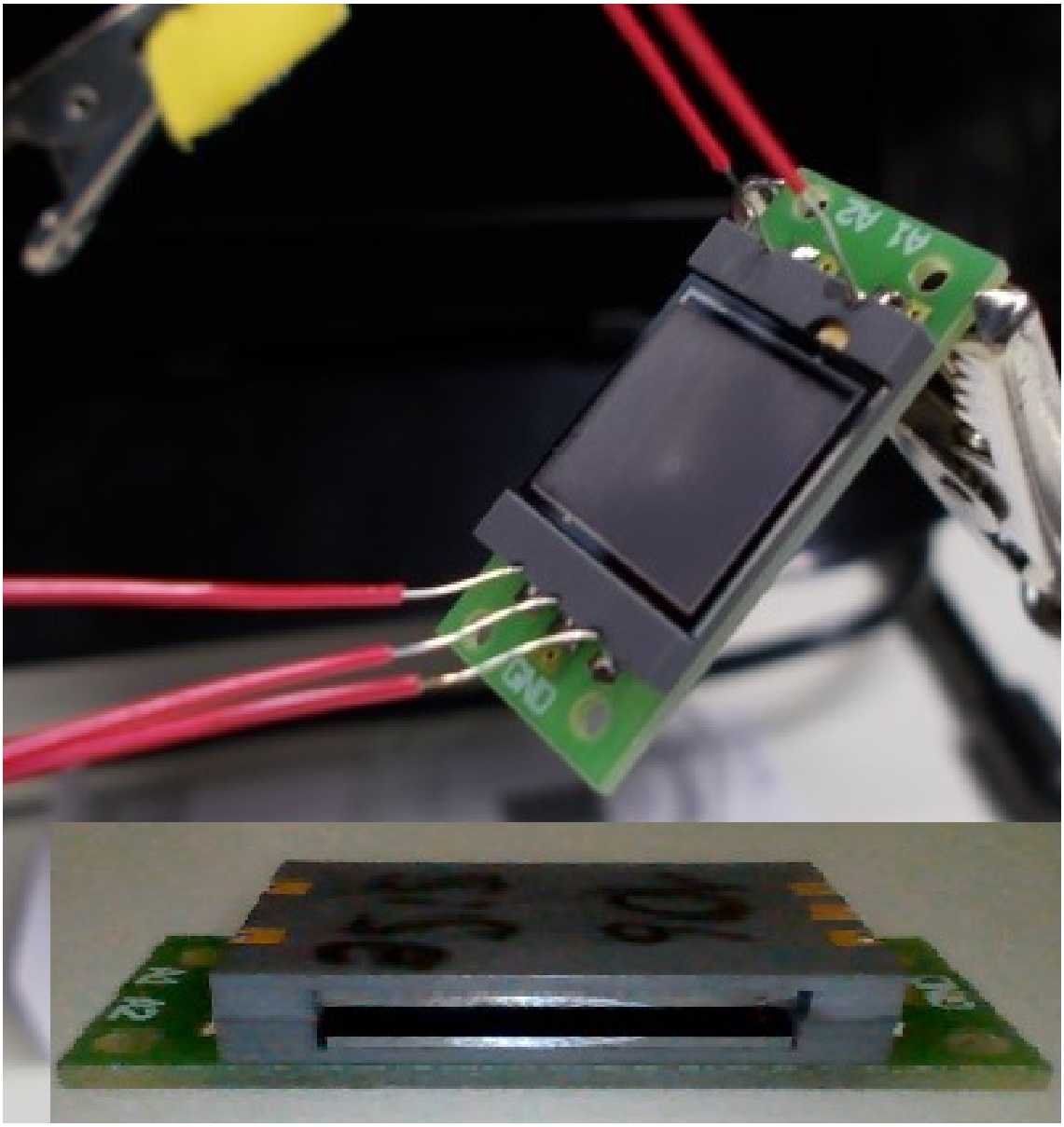

Figure 43: A *t*-Se covered PIN diode being soldered and the resulting detector 'sandwich'.

The length of the 32 cm long COLD array chromatographic channel was composed of 8 *t*-Se coated PIN diodes kept isothermal at 25°C, followed by 22 Au-coated PIN diodes (Au thickness 50 nm) with a negative temperature gradient to ≈ -160°C to adsorb and detect any radioisotopes which did not deposit on the *t*-Se surface (See also Figure 44). The Se- and Au-covered portions were separated by two quartz-covered detectors to prevent cross-signaling between the functionalized detectors. The *t*-Se detectors were preceded by a single quartz-covered detector to avoid turbulence at the channel entrance and ensure laminar flow over the chromatography column. Care was taken to remove any H_2O from the gas loop, and the H_2O dew point was kept below the detection limit of ≤ -100°C (Mitchell Easydew). Due to this limitation, it was assumed that the last Au-covered detectors below -100°C likely froze any remaining water in the carrier gas and formed an ice layer. The detection efficiency of single atoms deposited on the PIN detector surface is about 100% for SF decay and 86% for α-decay. Periodic washing (every ≈ 2 days) of the gold-covered PIN detectors was done with a series of solvents to restore their adsorption properties which were observed to change due to contamination over time. The washing procedure was solvents (ethanol, acetone, then diethyl ether) followed by thorough drying with a heat gun.

4.3 Results and Discussion

4.3.1 Analysis of Mono-atomic Tracers and Contamination

A typical deposition pattern in the COLD for the tracer $^{182-185}$Hg is shown in figure 44.

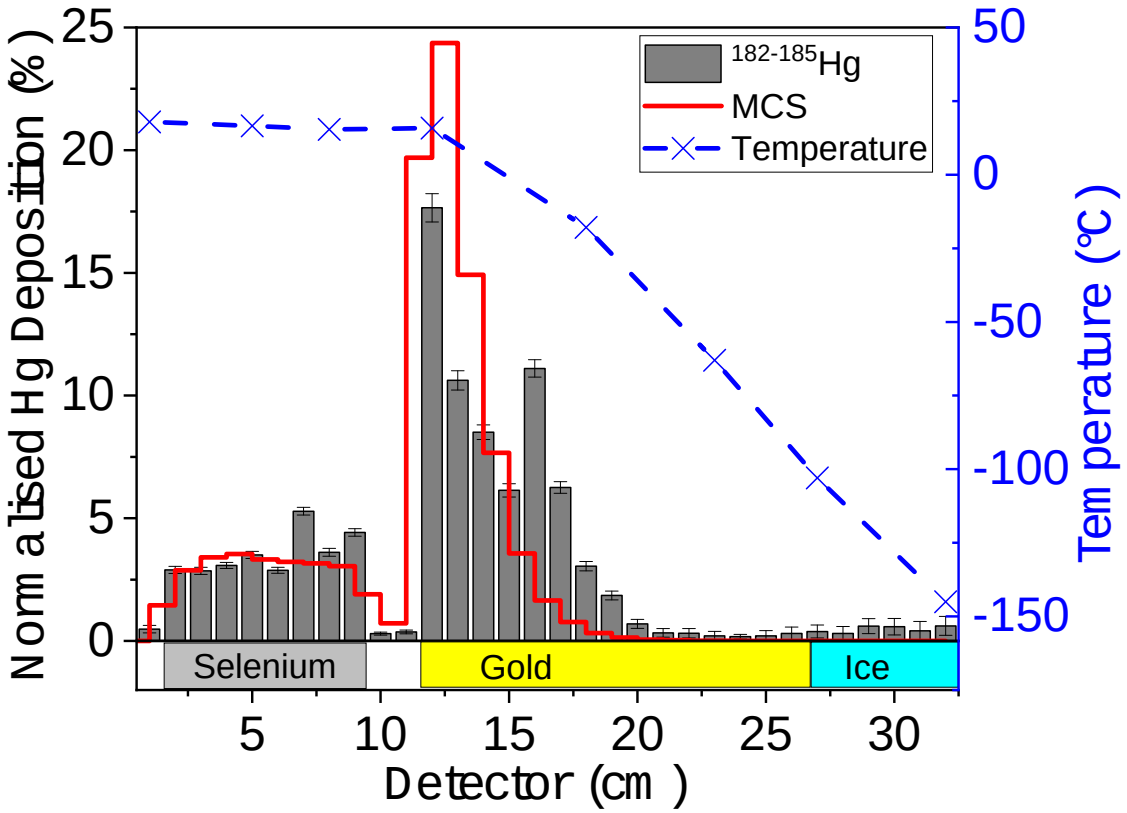

Figure 44: The relative radionuclide detection yield of $^{182-185}$Hg in the COLD during the 2018 experimental campaign measured by α-spectrometry. Red line represents a MCS deposition pattern of $^{182-185}$Hg programmed with the experimental conditions, dotted blue line shows the negative temperature gradient. The $^{182-185}$Hg deposition pattern shows a low affinity for the beginning of the GC column with Se coating, while it deposited diffusion-controlled on the gold-covered PIN detectors. MCS parameters used ΔH_{ads}^{t-Se}(Hg) = -60 kJ/mol, ΔH_{ads}^{a-Se} = -85 kJ/mol (3% coverage), ΔH_{ads}^{Au} = -98 kJ/mol, E_a(HgSe) = 82 kJ/mol, and pre-exponential factor $A = 5.0 \cdot 10^{13}$.

As expected, the $^{182-185}$Hg did not adsorb or react readily on the *t*-Se surface, and was transported to the Au detectors at the back of the array. In concordance with off-line experiments, the *t*-Se surface was modelled as heterogeneous using a microscopic MCS due to more reactive open ended polymeric Se_n chains (2% *a*-Se, see chapter 3) and the implementation of the Arrhenius equation (chapter 4). On the gold stationary phase, mercury deposited in a diffusion-controlled deposition pattern starting at room temperature, due to its high adsorption enthalpy

-ΔH_{ads}^{Au}(Hg) = 98 kJ/mol. It can be seen in figure 44, that on the gold surface the $^{182-185}$Hg deposition deviated from the MCS with a decreased- followed by an increased count. This was a repeatedly observed behaviour and the deviation from the simulated pattern became more prominent after longer experiment times, accompanied with an overall decrease in $^{182-185}$Hg detection in the COLD. Periodic washing of the detector surfaces was shown to recover both the total $^{182-185}$Hg yield, and restore the diffusion-controlled peak shape (Figure 45). Washing was done using a series of solvents then the PINs were thoroughly dried using a heat gun.

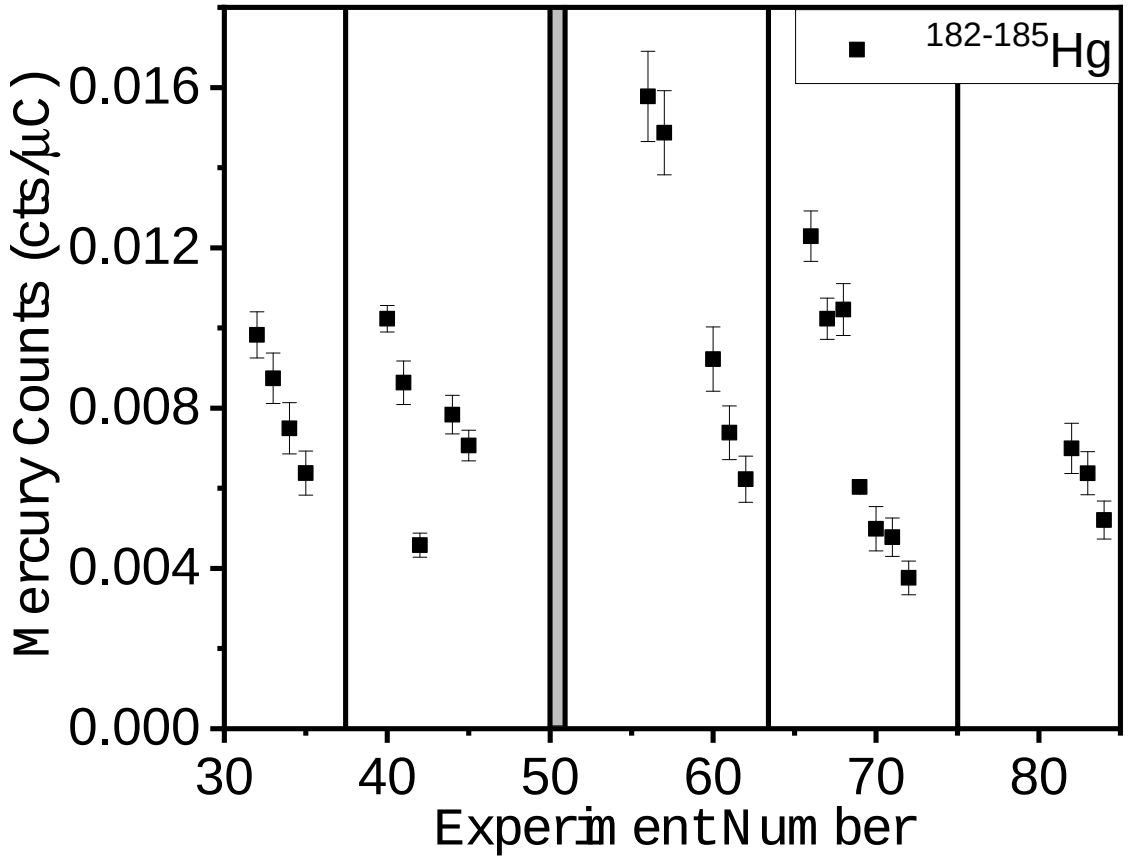

Figure 45: $^{182-185}$Hg detection yield fluctuation normalized to the collected beam integral between experimental runs. The black vertical bars indicate washing of the PIN detector surfaces. Double black bars with shading indicates detector wash and the change of $^{242}PuO_2/^{nat}Nd_2O_3$ target. Note that after every wash, there was a clearly reproducible increase of total $^{182-185}$Hg counts.

The combination of $^{182-185}$Hg detection yield loss accompanied with the characteristic de-

position peak shape distortion both pointed towards a gradual contamination of the PIN diodes. As the contamination covers the gold surface, there are less available adsorption sites for the tracer, forcing it to adsorb later in the column or even escape the column if the contamination is excessive. By comparing the expected deposition pattern of our MCS with a series of experiments in succession, the increasing trend of the contamination can be made visible (Figure 46).

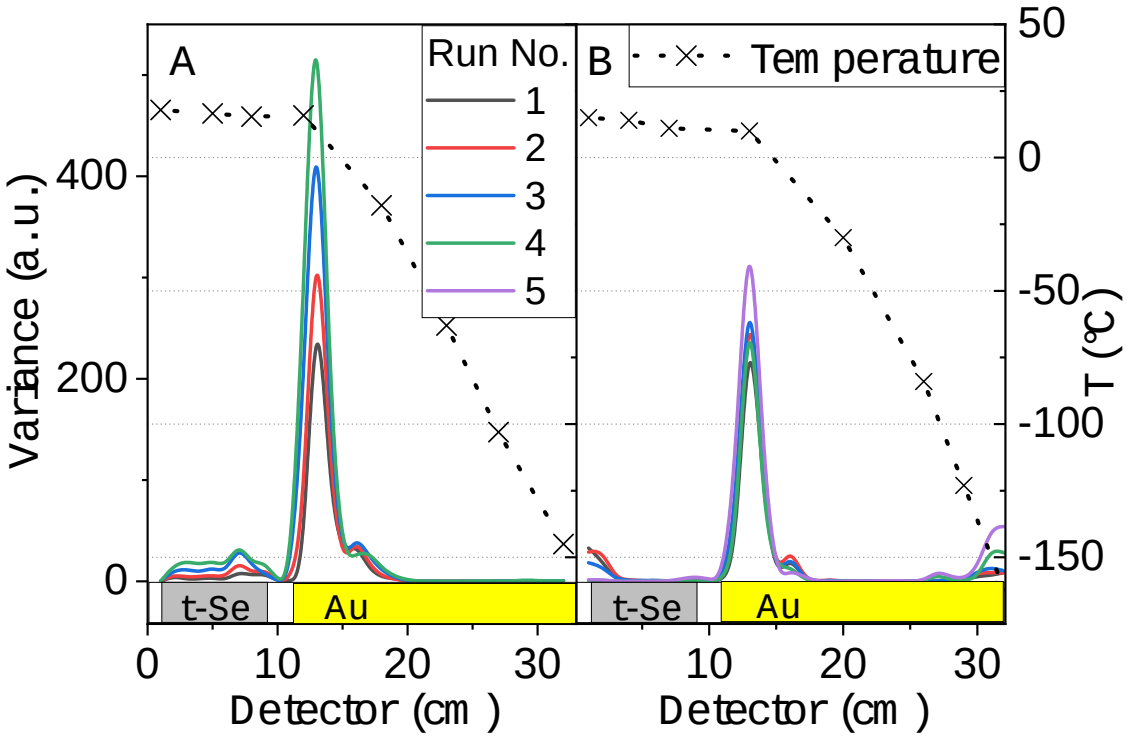

Figure 46: The variance of $^{182-185}$Hg deposition per detector from our MCS. While the *t*-Se covered detectors were largely unaffected, there is a clearly growing contamination deposited sharply on the early Au detectors, just as the temperature begins to decrease. The secondary small peak indicates the $^{182-185}$Hg depositing on later detectors as the adsorption sites on early PIN detectors become occupied. **B** Run 4 was done after a prolonged interruption of the experiment which showed to somewhat restore detector adsorption properties. **B** also shows the tracer escape at the back of the COLD due to contamination, despite the better cooling.

As the overall $^{182-185}$Hg count decreases in successive runs, but is restored by the cleaning

of PIN detector surfaces, it is a clear indication that the loss stems from the contamination buildup within the COLD. Furthermore, it becomes apparent from figure 46 **B**, that if contamination is sufficiently advanced, Hg is not recovered on later portions of the array, but rather deposits at the coldest portion of the chromatographic column or escapes the column entirely. Additionally, after a lengthy operating pause due to cyclotron failure before run **B** 4 (green line) it can be seen that the deposition recovered significantly before worsening again for the subsequent run. When compared to figure 46 **A**, where the temperature at the cooled end was not sufficiently low, it is likely that some of the tracer escapes the column therefore decreasing the overall yield. The identity or source of contamination could not be pinpointed; it deposited on the chromatographic column preferentially as the temperature dropped below $\approx 20°C$ and was found only on the gold surfaces. It was observed to accumulate over time but could easily be removed by washing of the detectors. For the purpose of the copernicium experiment, it is important to note that there was no indication of the *t*-Se surface affected by this contamination.

As was mentioned before, the overall yield of $^{182-185}$Hg fluctuated significantly between experiments. While loss of yield was observed in successive experiments, a significant overall yield fluctuation was also found *independent* of the contamination buildup. Additionally, a fusion reaction byproduct ^{211}At was also observed to fluctuate in yield similar to mercury. The detector contamination could not account entirely for this effect and an additional source was identified. As seen in figure 42, the tantalum getter in the GC loop is a component dedicated to the removal of O_2 from the gas. As it operates, Ta is oxidised while purifying the carrier gas of O_2. This component was operated at different temperatures and the gas composition was monitored using an atmospheric mass spectrometer (Table 7).

Table 7: The mean partial pressure (arbitrary units) of residual gases in the GC with respect to operation of the tantalum getter at different temperatures. The mass spectrometer was not calibrated so measurements are relative.

Getter T (°C)	O_2 (mbar)	H_2 (mbar)	H_2O (mbar)
25	$1.5 \pm 0.3 \cdot 10^{-3}$	$3.5 \pm 0.4 \cdot 10^{-6}$	$2.0 \pm 0.5 \cdot 10^{-6}$
400	$1.1 \pm 0.3 \cdot 10^{-3}$	$4.0 \pm 2.2 \cdot 10^{-6}$	$2.2 \pm 1.2 \cdot 10^{-6}$
950	$1.7 \pm 2.0 \cdot 10^{-6}$	$1.5 \pm 1.3 \cdot 10^{-5}$	$1.4 \pm 1.2 \cdot 10^{-5}$

The Ta only removed O_2 at higher temperatures, but in parallel increased the detectable H_2O and H_2 levels. I correlated these fluctuating residual gases between experiments to the absolute yields of the tracer $^{182-185}$Hg and reaction byproduct ^{211}At (Figure 47).

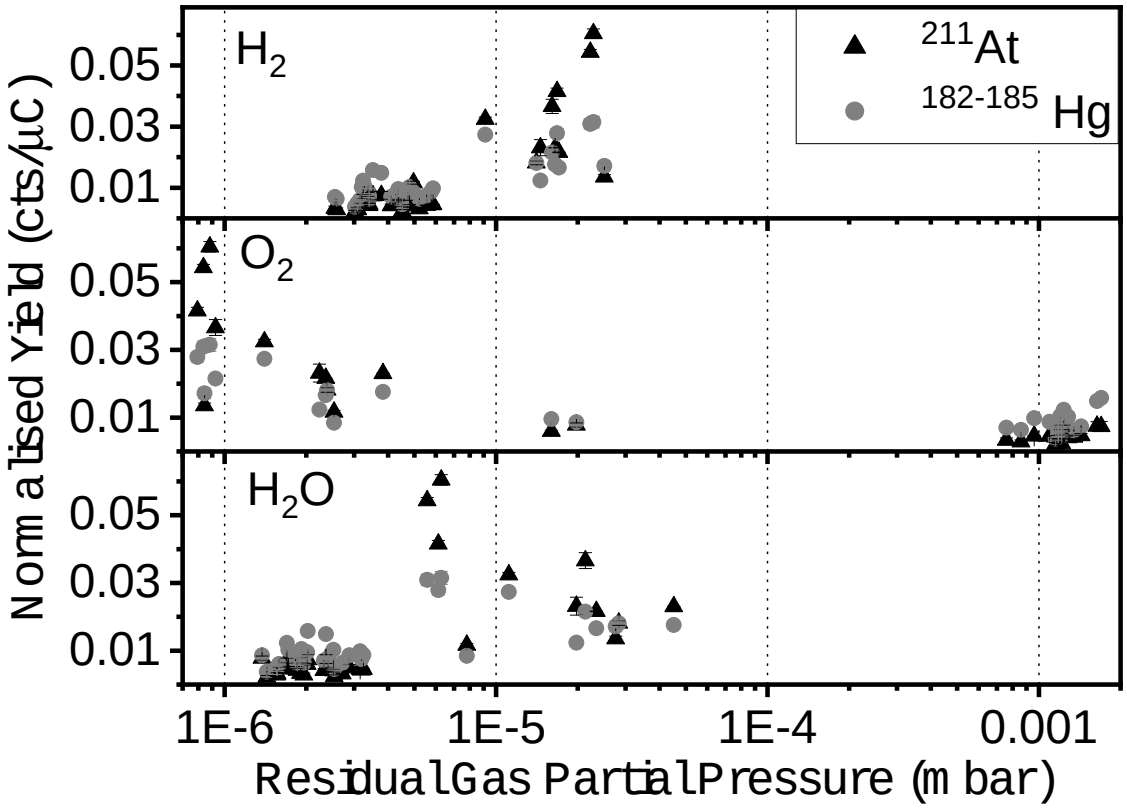

Figure 47: The total radionuclide detection yields normalized with respect to the collected beam integral for ^{211}At and $^{182-185}$Hg measured by α-spectrometry with respect to the partial pressure of trace gases H_2 (top), O_2 (middle), and H_2O (bottom). The yield is higher by up to a factor of 6 when H_2 is present in trace amounts, and when O_2 is at minimal levels. H_2O did not show a direct effect on the yield. Partial pressure values are relative.

The loss of $^{182-185}$Hg yield by a factor of ≈ 3 in the presence of trace O_2 is a strong indication that the tracer is oxidised between the recoil chamber and detector array, forming non-volatile HgO. It is known that under the conditions of a plasma, such as those created by the heavy ion beam inside the recoil chamber, mercury can be oxidised [34, 35]. As only volatile species are transported to the COLD array, a significant portion of the tracer is lost, decreasing the detection yield. The presence of H_2 is not believed to have an effect, as Hg is not known to form a hydride. H_2O did not indicate a trend.

The ^{211}At yield showed a similar trend in response to oxygen and hydrogen as mercury. As a member of the halogens however, the formation of AtH is not ruled out [36]. Furthermore, a clear change of speciation of astatine in the gas chromatography indicated by the presence of two distinct peaks in the GC under different conditions was observed (Figure 48).

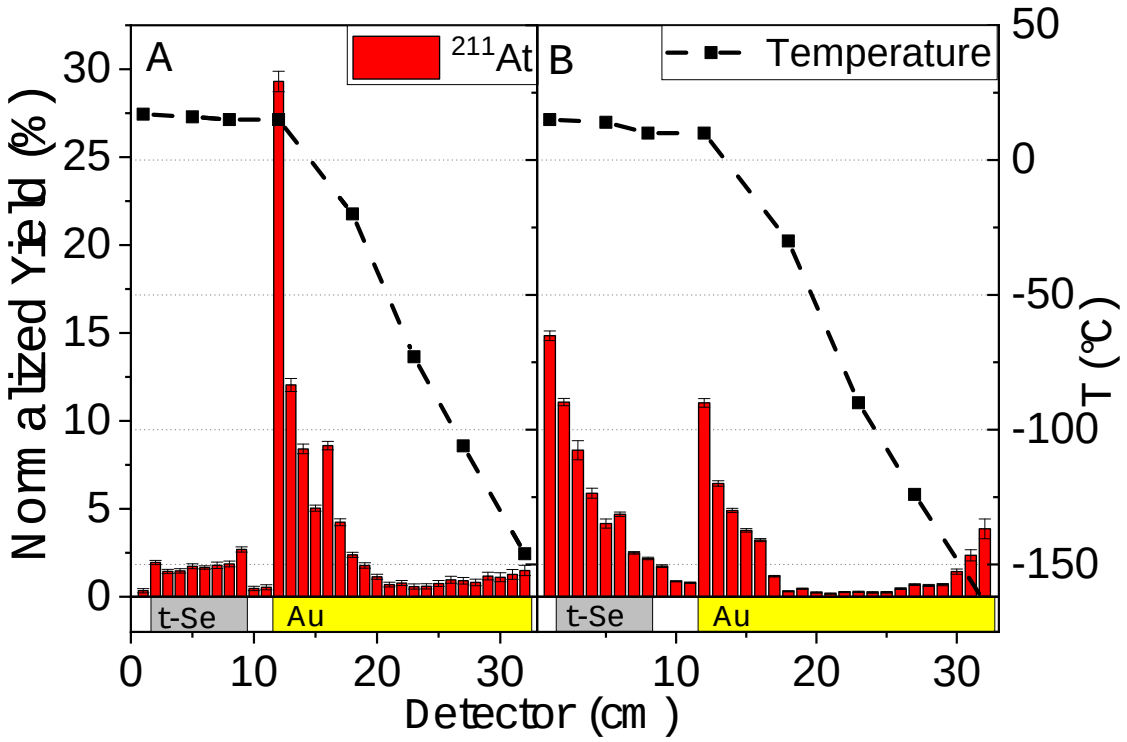

Figure 48: **A**: ^{211}At deposition pattern measured using α-spectrometry with high O_2 residual gas content (Ta getter at 400°C). The astatine also showed peak broadening due to increasing contamination on the gold covered PIN detectors. **B:** ^{211}At deposition patter with low O_2 content (Ta getter at 950°C). Three distinct peaks are visible, one on the quartz and *t*-Se covered PIN diodes, a secondary peak on the gold-covered PIN diodes. One peak in **B** is visible on the final detectors due to sufficient cooling on the PIN diodes assumed to be covered in ice due to the -100°C dew point.

In Figure 48 **B** a third peak was also forming due to better cooling at the rear of the COLD, which due to the -100°C dew point is assumed to be covered in ice. The speciation of ^{211}At, along with the fluctuation in detection yield for both $^{182-185}$Hg and ^{211}At is clear evidence that even trace amounts of residual gas contaminants in the purified carrier gas can interfere with these types of experiments on the atom-at-a-time scale. Despite the nuclear fusion product ^{287}Fl and its daughter ^{283}Cn having been postulated to be inert, they are still members of group 14 and 12 respectively, and likely susceptible to oxide formation (especially under the violent conditions of a beam plasma). Should these SHEs oxidize after production, the SHE oxide could no longer be volatile, resulting in a transport loss. Furthermore, even if the oxide is volatile, the SHE is no longer in its elemental state, thereby changing its adsorption enthalpy and resulting in unexpected deposition peaks in the internal chromatogram. The Given the low production rates, it is therefore paramount to minimize the amount of O_2 in the gas chromatography.

4.3.2 Detection of Copernicium Decay

During the five week experimental campaign, six decays attributable to SHE decays were detected. Taking into consideration the efficiencies affecting detection, $\approx$ 16 atoms should have been detected. This large loss can stem from a number of sources, such as reduced cross sections due to target degradation or increased transport losses. From the significant $^{182-185}$Hg and ^{211}At detection yield fluctuations due to contaminants observed, it is likely that ^{283}Cn was also

affected. The detected atoms were combined with the existing two events from the preceding experiments in 2015.

Four α-SF decay chains could be unambiguously linked to ^{283}Cn due to the characteristic high-energy α-particle and time-correlated SF signature (Figure 49). In all cases, no decay of a ^{287}Fl atom was registered.

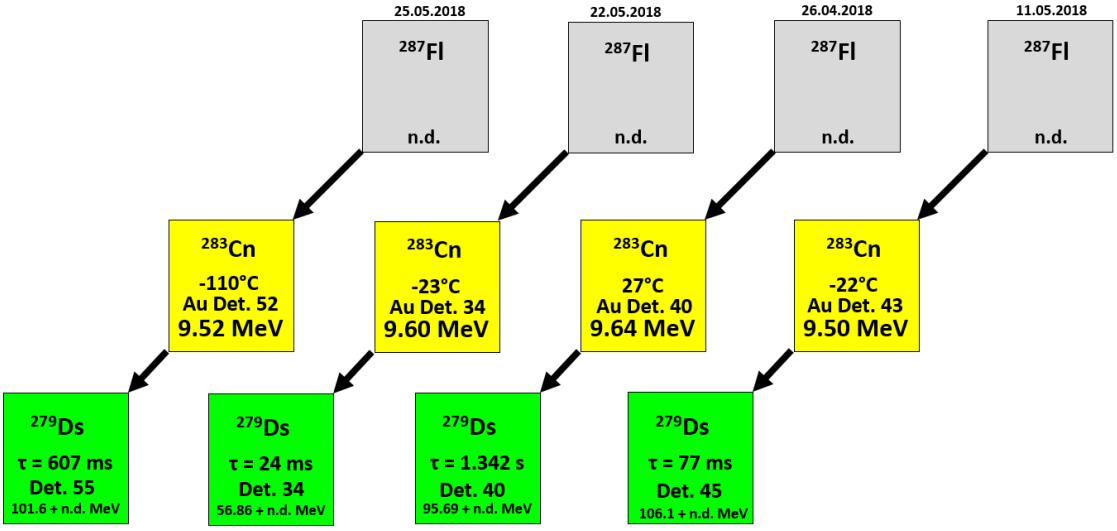

Figure 49: Detected α-SF decay chains assigned to the decay of ^{283}Cn. n.d. = not determined.

Additionally, two SFs were also assigned to the decay of ^{283}Cn or a daughter (Figure 50). While the α decay of these two was not recorded and no time correlation to a parent nuclide could be established, both signals were near-simultaneously occurring coincidence fissions detected in geometrically opposing PIN diodes. Due to this, both events were assigned to a SHE decay.

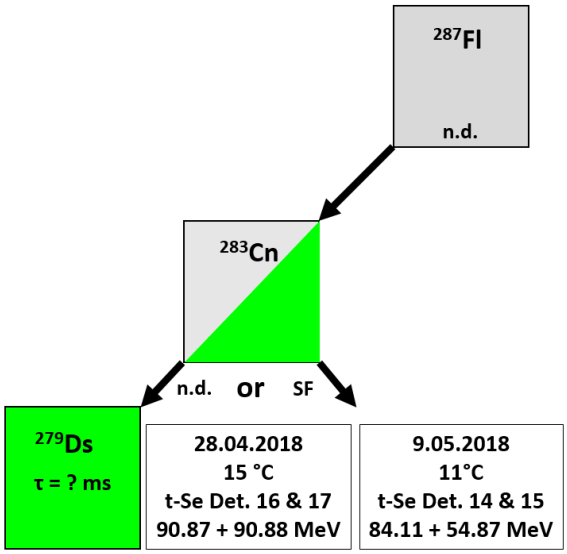

Figure 50: Two detected coincident SF fragment pairs, both in geometrically opposing *t*-Se covered detectors.

4.3.3 The Copernicium-Selenium Interaction

The primary aim of this experiment was to generate additional data for the interaction between Cn and Se so that a conclusion for the reactivity of copernicium towards selenium can be drawn. In chapter 2 it was shown from extrapolated predictions that CnSe formation is thermodynamically unfavourable compared to the formation of HgSe. However, due to all of the copernicium decays being observed on a selenium surface in 2015, a surprising trend reversal for group 12 was suspected, in which Cn showed increased reactivity towards *t*-Se compared to its lighter homolog Hg. In Chapter 4 an extrapolation of the activation energy trend in group 12 elements indicated a possible higher activation energy barrier for the CnSe formation, as would be expected for an inert element. Since 2015, a total of 8 decays linked to ^{283}Cn have been detected in an isothermal *t*-Se chromatography (Table 8).

Table 8: All events attributed to SHE decay recorded during a Cn-Se experiment. Values marked with ‡ from 2015 experimental campaign [25]. Gold contamination levels are estimated from the peak broadening and $^{182-185}$Hg and ^{211}At detection yield in the internal chromatogram.

Detected	Surface	Temperature (°C)	Gold Contamination level
SF	Se	15	low
SF	Se	11	low
α-SF	Au	27	low
α- SF	Au	-22	low
α-SF	Au	-23	high
α-SF	Au	-110	high
α-SF‡	Se	25	
α-SF‡	Se	25	

Half of the atoms recorded to this date have therefore been observed on the *t*-Se surface. While this data does not categorically define the reactivity of copernicium, a significant portion of atoms has been observed on the *t*-Se surface. The probability of observing a ^{283}Cn decay event on selenium by in-flight decay can be estimated by using a MCS and lies at $5 \cdot 10^{-4}$ (Figure 51).

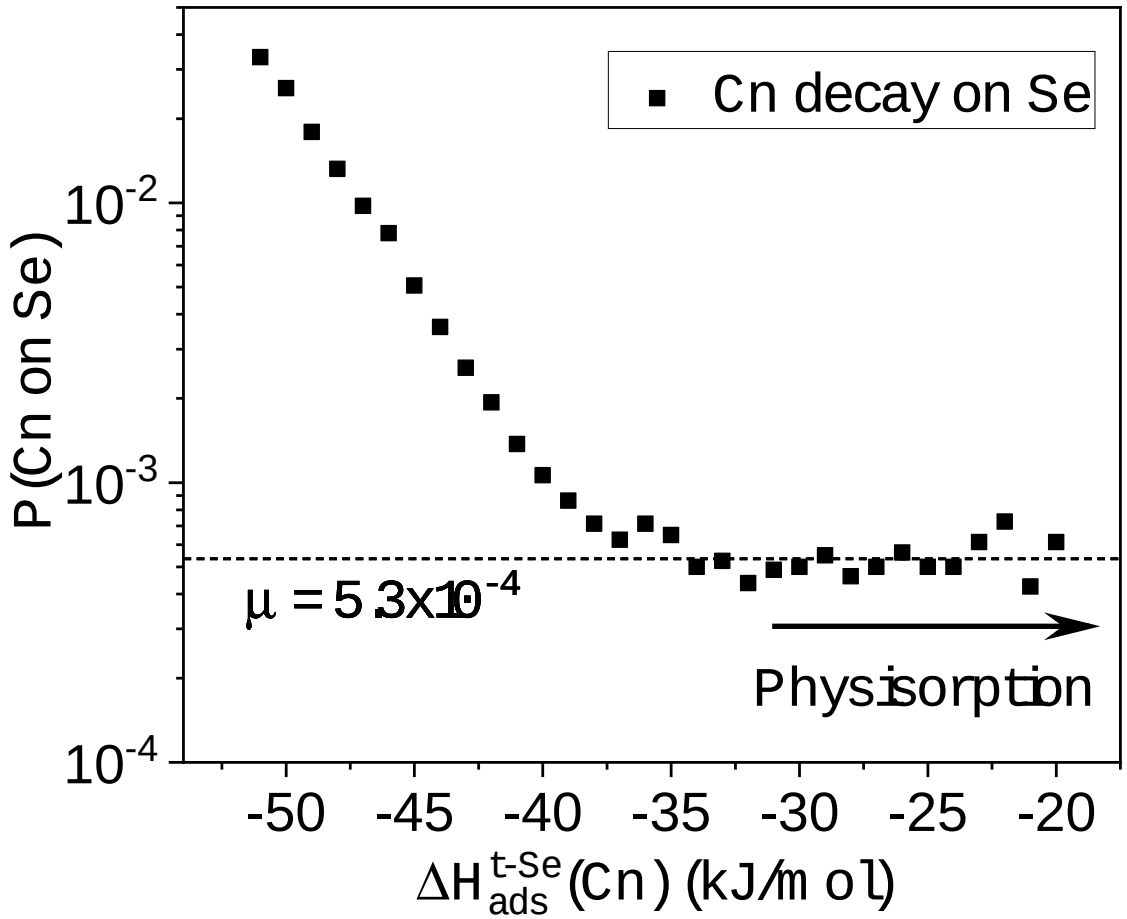

Figure 51: MCS showing the probability of ^{283}Cn atoms decaying in the COLD array on the *t*-Se covered portion with respect to adsorption enthalpy. As ΔH_{ads} > -30 kJ/mol represents an interaction solely due to physisorption, decays observed in this region are generally due to the short half-life of the ^{283}Cn atom decaying before it can travel further down the chromatographic column. The mean probability of in-flight decay events is therefore $5 \cdot 10^{-4}$. $8 \cdot 10^{4}$ atoms were simulated.

Observing half the atoms on selenium is therefore extremely unlikely and it must be concluded that the adsorption interaction of copernicium on selenium plays a significant role. It follows that copernicium likely does not exhibit noble gas-like properties to the extent that has previously been postulated. The observation can be explained with one of the following scenarios:

I. The effect is entirely due to the adsorption enthalpy: $-\Delta H_{ads}^{t-Se}$(Cn) >> $-\Delta H_{ads}^{t-Se}$(Hg)

II. The adsorption enthalpy for Cn on Se is lower than Hg, following the trend observed on Au: $-\Delta H_{ads}^{t-Se}$(Cn) < $-\Delta H_{ads}^{t-Se}$(Hg). However, the formation of a selenide is more likely due to a significantly lowered activation energy: E_a (CnSe) << E_a (HgSe).

III. The adsorption enthalpies are similar: $-\Delta H_{ads}^{t-Se}$(Cn) ≈ $-\Delta H_{ads}^{t-Se}$(Hg). The activation energy for selenide formation is lower for copernicium: E_a (CnSe) < E_a (HgSe).

Case I: The increased adsorption enthalpy on *t*-Se of copernicium when compared to mercury is the primary cause of the observed deposition pattern. It follows that copernicium adsorbs more strongly than its lighter homolog. A MCS to determine the most likely ΔH_{ads}^{t-Se} was adapted to simulate 8 atoms distributing in 10,000 experiments over the COLD array (Figure 52).

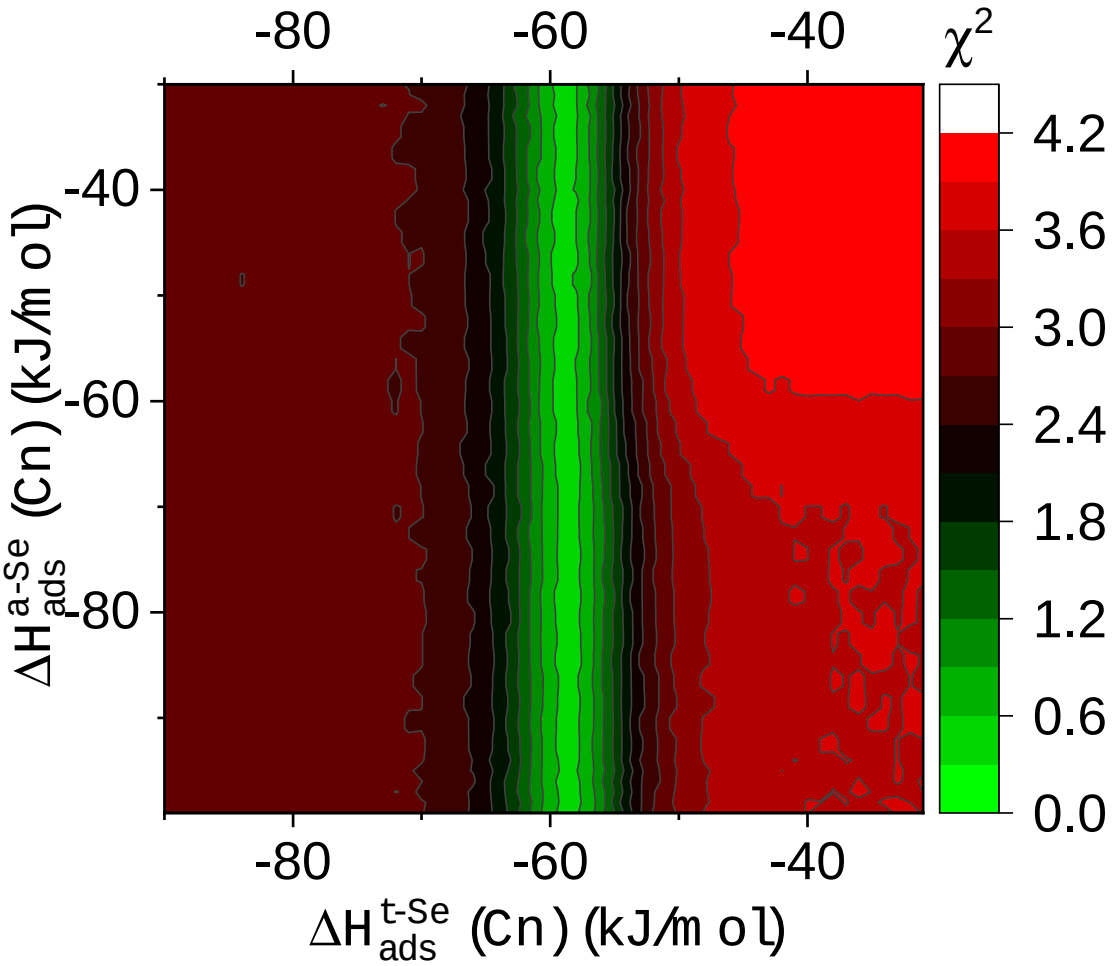

Figure 52: MCS χ^2 test varying the ΔH_{ads}(Cn) for a *t*-Se with a 1% *a*-Se surface coverage. The *a*-Se surface becomes negligible at such low coverage. Minimum at -ΔH_{ads}^{t-Se}(Cn) = 59 ±9 kJ/mol. χ^2 determined from 4 out of 8 atoms depositing on the *t*-Se in 10^4 experiments.

An adsorption enthalpy of -ΔH_{ads}^{t-Se}(Cn) = 59 ±9 kJ/mol was established (Figure 53). This result is close to the 2015 experimental campaign, where a limit of -ΔH_{ads}^{t-Se}(Cn) > 63 kJ/mol was established from two observed atoms [25]. It is apparent from the simulation, that even with an excessively high adsorption enthalpy value for *a*-Se there is no significant effect on the deposition pattern due to the high degree of surface conversion. This means that -ΔH_{ads}^{t-Se}(Cn) > -ΔH_{ads}^{Au}(Cn). At such a high adsorption value, the Cn-Se interaction can be considered a **chemisorption**, meaning that there is a chemical bond formation and the adsorption interaction

is not solely due to Van der Waals forces. If chemical bond formation must be considered, Case I is not the most likely of the three scenarios.

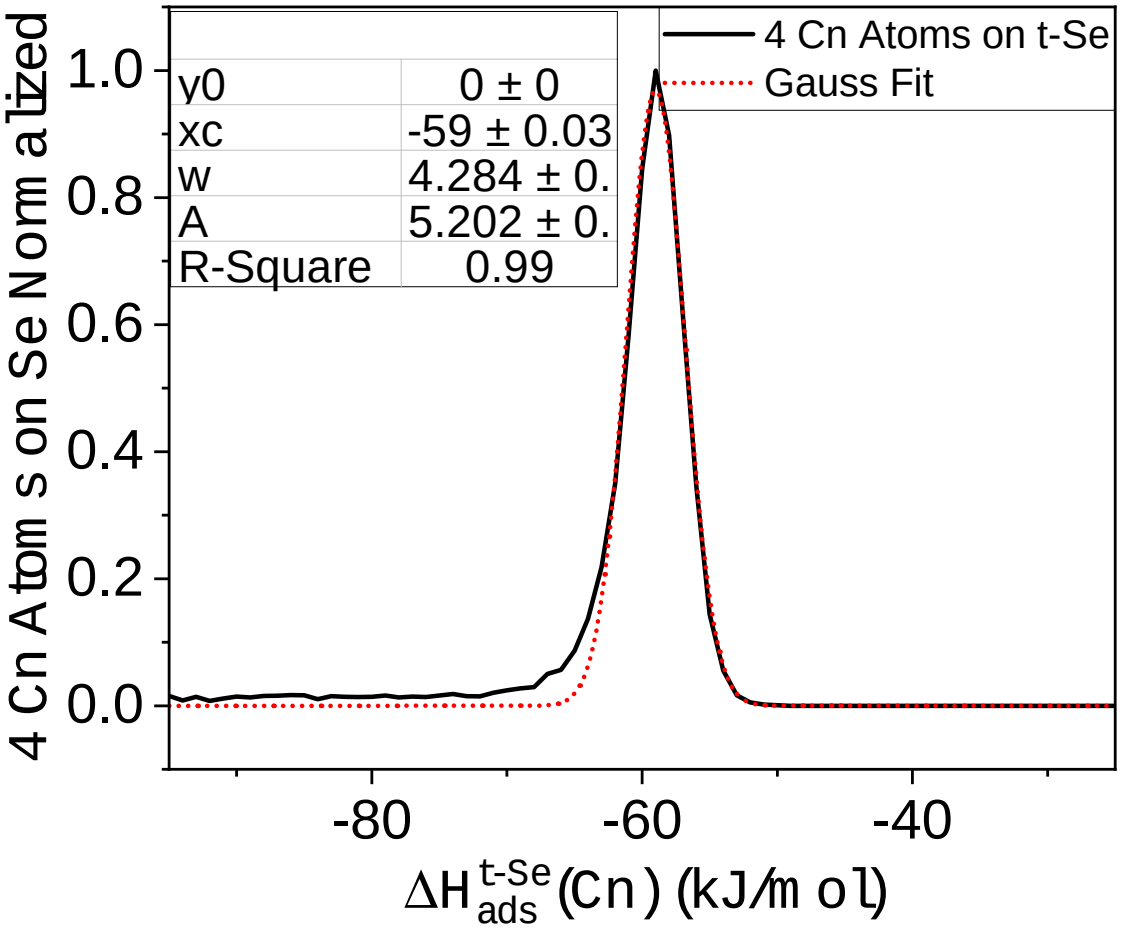

Figure 53: Normalized distribution of 4 out of 8 Cn atoms depositing on the *t*-Se covered portion of the COLD array, with a Gauss fit. The 95% confidence interval lies at -ΔH_{ads}^{t-Se}(Cn) = 59 ±9 kJ/mol.

Case II & III: Since the analysis in Case I points to chemisorption, the observed deposition pattern is likely due to a combination of adsorption enthalpy and chemical bond formation. Using a MCS with the Arrhenius equation implemented to simulate a reaction between Cn and Se as was done in Chapter 4, an activation energy can be estimated for the reaction (Figure 54).

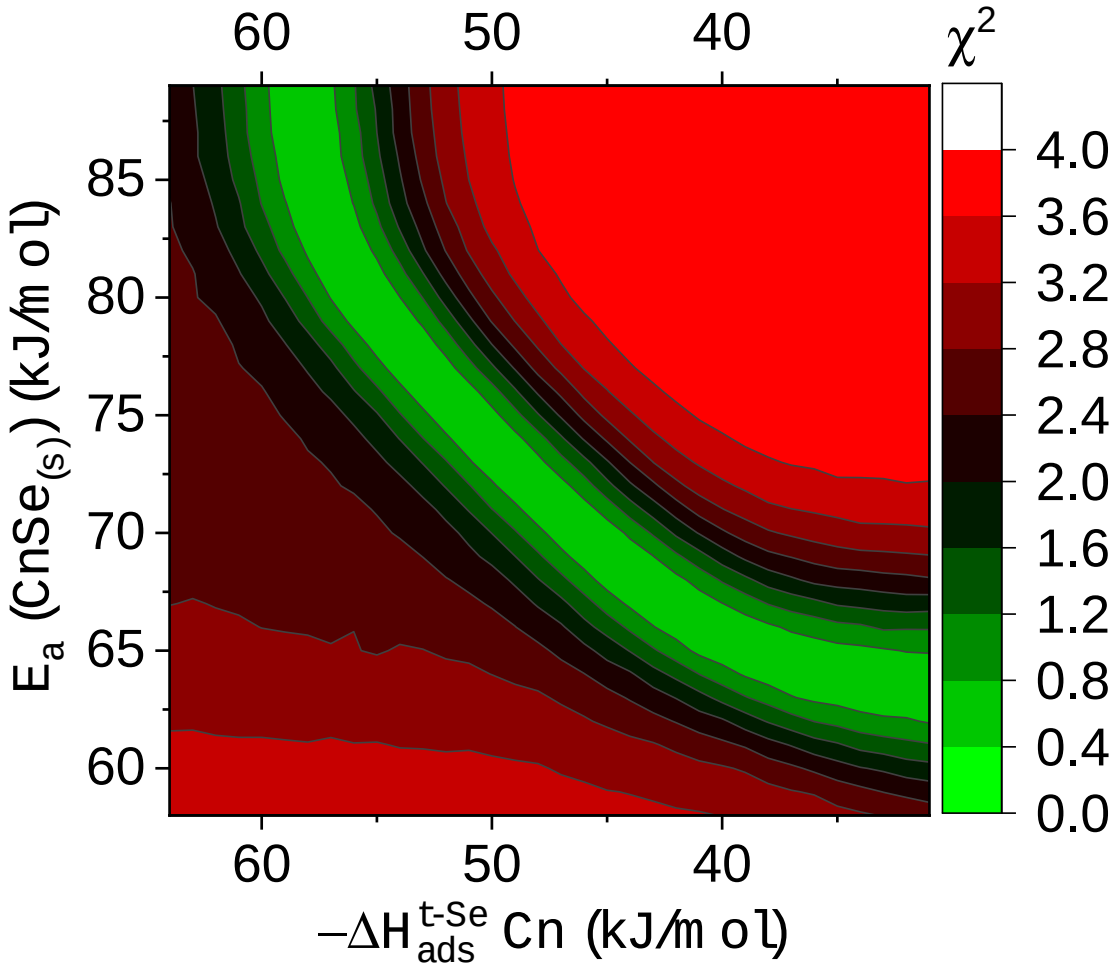

Figure 54: χ^2 test of 4 out of 8 Cn atoms detected on the *t*-Se covered portion of the COLD array. MCS of 8 atoms in 10,000 experiments respectively. The search was restricted to 59 kJ/mol > -ΔH_{ads}^{t-Se}(Cn) > 20 kJ/mol, as the deposition solely due to adsorption ΔH_{ads}^{t-Se} value was 59 kJ/mol (determined in Figure 52). The lower limit of 20 kJ/mol was chosen as it is in the range of adsorption enthalpy values of typical inert tracer-surface combinations such as radon on quartz (-ΔH_{ads}^{Quartz}(Rn)= 20 kJ/mol) [37]. Arrhenius pre-exponential factor used $5 \cdot 10^{13}$ s^{-1}.

It is evident that the upper limit of the result approaches -ΔH_{ads}^{t-Se}(Cn) = 59 kJ/mol. At this value, the deposition pattern observed in the COLD is mostly governed by the adsorption enthalpy, and the activation energy has no effect. Similarly, the curve also approaches a lower limit value for $E_a \approx 62$ kJ/mol. Below this value, the deposition pattern in the COLD is entirely

governed by the low activation energy. It is reasonable to assume that the adsorption enthalpy of copernicium on *t*-Se should be well above that of an inert noble gas Rn tracer - quartz surface combination -$\Delta H_{ads}^{SiO_2}$(Rn) = 20 kJ/mol [37]. As a result, a lower limit for the E_a(CnSe) > 62 kJ/mol can be set. As chemisorption involves chemical bond formation, it is also reasonable to assume that an activation energy is involved in the observed deposition pattern, setting the upper limit for E_a(CnSe) < 85 kJ/mol.

In Chapter 4, the extrapolated activation energy for the reaction to form CnSe was extrapolated to be $E_a = 106 \pm 22$ kJ/mol. Figure 54 shows that the value of the activation energy of the CnSe system is likely in the range E_a(CnSe) = 62 − 85 kJ/mol. This range is low compared to the range of the extrapolated 106±22 kJ/mol, but most notably lower than the activation energy for the formation of mercury selenide (E_a(HgSe) = 100 ± 10 kJ/mol). This further strengthens the previously drawn conclusion that copernicium is more reactive towards trigonal selenium than its lighter homolog mercury.

A likely reason for the increased reactivity of copernicium towards trigonal selenium is due to lower steric hindrance when compared to mercury. Trigonal selenium consists of many parallel Se_n chains with considerable inter-chain bonding as is reflected by its melting point (221°C). The high melting point can be attributed to the polymer-like nature of the Se_n chains interacting by van der Waals forces. Additionally, the distance between *t*-Se chains (min. 3.467 Å) is small [38, 39] (Figure 55).

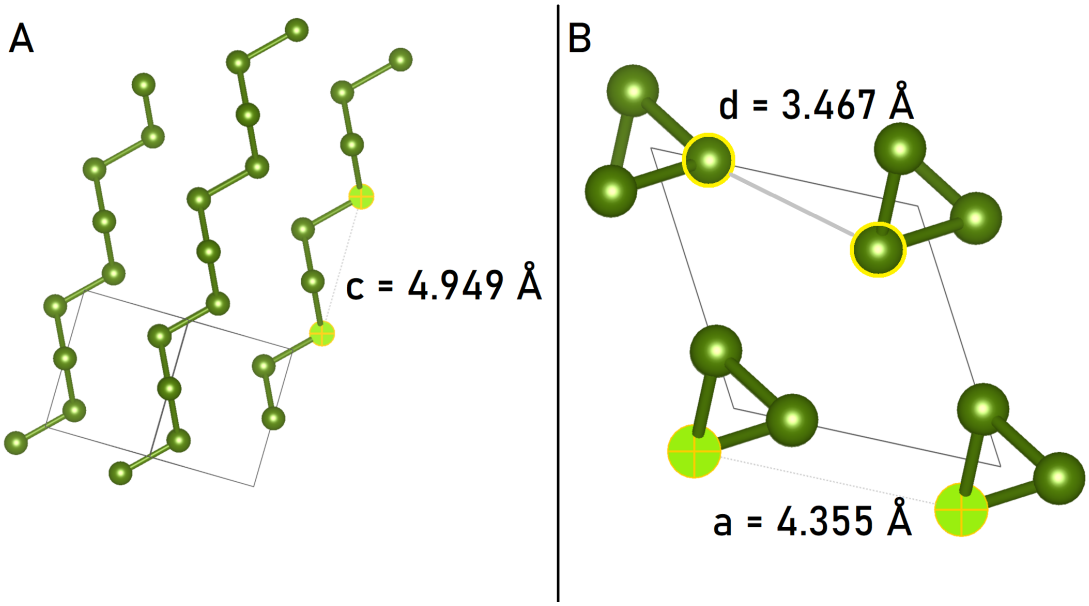

Figure 55: **A** *t*-Se showing the lattice parameter *c* along the chains. **B** View along the trigonal chains showing the lattice parameter *a*, and the shortest distance between two chains *d*. Image taken with VESTA [40].

With its calculated radius, Cn (1.71 Å) [41] can easily penetrate the *t*-Se lattice even at the narrowest point, whereas Hg at (2.23 Å) has difficulty in penetrating at all. However, heating the system as was done in Chapter 4 causes thermal expansion and increased lattice vibrations in the *t*-Se and thus allows Hg to also react with the trigonal selenium [42]. Grosse shows that interestingly, *t*-Se is atypical in that it thermally expands by increasing the distance between individual chains along lattice parameter *a*, but contracts along *c*, the length of an chain. *a* expands according to equation 43 [42].

$$a(T) = 4.277 + (3.215 \cdot 10^{-4})T \tag{43}$$

where T is the temperature (K), and a the lattice parameter. From this equation, to reach an expansion that allows mercury to enter the lattice at a, one would have to heat the selenium well above the melting point.

4.4 Conclusions

More data is required to draw a stronger conclusion; with the completion of the new Superheavy Element Factory DC-280 Cyclotron facility in Dubna, FLNR higher SHE production rates will significantly facilitate such experiments. An isothermal chromatography with a *t*-Se column at several different temperatures could provide valuable information on both the adsorption and reaction behaviour of copernicium on a selenium stationary phase.

The reactivity of Cn is likely the product of the competition between the direct relativistic effects of *s*-shell stabilization and the consequent indirect effects of *d*-shell destabilization. From this experimental campaign the conclusion can be drawn that the previously established adsorption series ΔH_{ads}^{Au} of Hg > Cn > Rn is preserved. However, in terms of group 12 reactivity for the formation of the selenide, the postulated inertness of Cn is challenged; E_a(MSe) of Cn < Hg < Rn , therefore favouring the selenide formation for copernicium. It was also shown that with the current amount of data indicating E_a(CnSe) = 62 − 85 kJ/mol, the previously extrapolated E_a(CnSe) = 106 ± 22 kJ/mol could be an overestimation, making the CnSe formation even more likely. Since Cn does have some noble gas-like character as has been shown, but is able to penetrate the trigonal selenium lattice the most likely reason for the lowered activation energy observed is due to sterics.

We also found that there were two major sources of contamination which affected the radionuclide yield in the gas chromatography loop. The most significant fluctuation was likely caused by residual oxygen content in the loop during experiments with low Ta getter temperature, which caused a decrease of $^{182-185}$Hg yield by a factor of ≈ 3. This is a find of extreme importance, as the SHEs investigated here may be susceptible to oxide formation as members of groups 12 and 14. Other residual gases like H_2 and H_2O were also observed in the system, but did not appear to have a direct effect on the $^{182-185}$Hg yield.

Additionally it was discovered that an unknown volatile contamination was building up on the COLD surface exclusively on the Au covered PIN detectors over the entire section of the array that was cooled. The source of the contamination could not be identified, but points

to compounds volatile at room temperature which deposit readily on a gold surface as the temperature drops. One such source could be volatile carbon compounds leftover in the ^{242}Pu target material from the manufacturing process. During irradiation the target heats up and could be a potential source for such volatile carbon compounds. As only a monolayer covering the chromatographic surface is required to reduce the adsorption effectiveness of the PIN diodes, a small amount is sufficient to interfere with the experiment. Assuming an atomic monolayer covering all gold detectors in the COLD entirely, only ≈ 70 nmol of a substance is needed (less as it is likely molecular). Periodic washing of the detectors however removed the contamination buildup.

Superheavy element experiments push current technologies in both production and detection to the limit. Their production as single-atom requires an extreme degree of control over the ambient conditions of the experiment so that reliable results can be produced. It was shown that despite best efforts to maintain stable and clean experimental conditions over long periods of time, contamination effects were clearly observable. Future experimental campaigns must be aware of these issues and dedicated experiments to optimize the cleanliness and stability of superheavy element experiments will be an unavoidable part of this field in the future. This dire need has given rise to the development of the Trace-gas Reaction Analyzer for Chemistry (TRACY) gas chromatography loop, designed as a more compact modular iteration of the COLD loop in the following Chapter 6.

References

1. Myers, W. D. & Swiatecki, W. J. Nuclear masses and deformations. *Nuclear Physics* **81,** 1–60. ISSN: 00295582 (1966).
2. Steinegger, P. *et al.* Vacuum Chromatography of Tl on SiO2 at the Single-Atom Level. *Journal of Physical Chemistry C* **120,** 7122–7132. ISSN: 19327455 (2016).
3. Vahle, A. *et al.* Adsorption Studies with Homologs of Superheavy Elements. *Adsorption Journal Of The International Adsorption Society* **09,** 2000–2000 (2000).

4. Hoffman, D. C., Lee, D. M. & Pershina, V. in *The Chemistry of the Actinide and Transactinide Elements* 1652–1752 (Springer, Dordrecht, 2006). ISBN: 1402035985.

5. Fricke, B. in *Struct. Bonding* J. D. Duni, 89–144 (Springer, Berlin, 1975).

6. Hammer, B. & Norskov, J. Why gold is the noblest of all the metals. *Nature* **376,** 238–240 (1995).

7. Eliav, E., Fritzsche, S. & Kaldor, U. Electronic structure theory of the superheavy elements. *Nuclear Physics A* **944,** 518–550. ISSN: 03759474. http://dx.doi.org/10.1016/j.nuclphysa.2015.06.017 (2015).

8. Norrby, L. J. Why is mercury liquid? Or, why do relativistic effects not get into chemistry textbooks? *Journal of Chemical Education* **68,** 110. http://pubs.acs.org/doi/abs/10.1021/ed068p110 (1991).

9. Calvo, F., Pahl, E., Wormit, M. & Schwerdtfeger, P. Evidence for low-temperature melting of mercury owing to relativity. *Angewandte Chemie - International Edition* **52,** 7583–7585. ISSN: 14337851 (2013).

10. Schwerdtfeger, P., Dolg, M., Schwarz, W. H. E., Bowmaker, G. A. & Boyd, P. D. W. Relativistic effects in gold chemistry. I. Diatomic gold compounds. *The Journal of Chemical Physics* **91,** 1762–1774. ISSN: 0021-9606. http://aip.scitation.org/doi/10.1063/1.457082 (1989).

11. Pitzer, K. S. Relativistic Effects on Chemical Properties. *Accounts of Chemical Research* **12,** 271–276. ISSN: 15204898 (1979).

12. Pershina, V. G. Electronic structure and properties of the transactinides and their compounds. *Chemical Reviews* **96,** 1977–2010. ISSN: 00092665 (1996).

13. Eichler, R. *et al.* Chemical characterization of bohrium. *Nature* **407,** 106–108 (2000).

14. Düllmann, C. E. *et al.* Chemical investigation of hassium (element 108). *Nature* **418,** 859–862. ISSN: 00280836 (2002).

15. Schädel, M. *et al.* First aqueous chemistry with seaborgium (element 106). *Radiochimica Acta* **77,** 149–159. ISSN: 00338230 (1997).

16. Türler, A. *et al.* First measurement of a thermochemical property of a seaborgium compound. *Angewandte Chemie - International Edition* **38,** 2212–2213. ISSN: 14337851 (1999).

17. Pitzer, K. S. Are elements 112, 114, and 118 relatively inert gases? *The Journal of Chemical Physics* **63,** 1032–1033. ISSN: 00219606 (1975).

18. Mewes, J. M., Smits, O. R., Kresse, G. & Schwerdtfeger, P. Copernicium: A Relativistic Noble Liquid. *Angewandte Chemie - International Edition* **58,** 17964–17968. ISSN: 15213773 (2019).

19. Soverna, S. *et al.* Thermochromatographic studies of mercury and radon on transition metal surfaces. *Radiochimica Acta* **93,** 1–8. ISSN: 00338230 (2005).

20. Eichler, R. & Schädel, M. Adsorption of radon on metal surfaces: A model study for chemical investigations of elements 112 and 114. *Journal of Physical Chemistry B* **106,** 5413–5420. ISSN: 10895647 (2002).

21. Eichler, B. *Volatilization behavior of transactinides from metal surfaces and melts* tech. rep. 03-01 (Paul Scherrer Institute, Villigen, 2002), 1.

22. Eichler, R. *et al.* Chemical characterization of element 112. *Nature* **447,** 72–75. ISSN: 0028-0836. http://www.nature.com/doifinder/10.1038/nature05761 (2007).

23. Eichler, R. *et al.* Thermochemical and physical properties of element 112. *Angewandte Chemie - International Edition* **47,** 3262–3266. ISSN: 14337851 (2008).

24. Chiera, N. M., Eichler, R., Vögele, A. & Türler, A. Vapor deposition coating of fused silica tubes with amorphous selenium. *Thin Solid Films* **592,** 8–13. ISSN: 00406090. arXiv: 9809069v1 [arXiv:gr-qc]. http://dx.doi.org/10.1016/j.tsf.2015.08.043 (2015).

25. Chiera, N. M. *Towards the Selenides of the Superheavy Elements Copernicium and Flerovium* PhD thesis (University of Bern, 2016).

26. Chiera, N. M. *et al.* Interaction of elemental mercury with selenium surfaces: model experiments for investigations of superheavy elements copernicium and flerovium. *Journal of Radioanalytical and Nuclear Chemistry* **311,** 99–108. ISSN: 15882780 (2017).

27. Cabral, A. R. *et al.* Clausthalite (PbSe) and tiemannite (HgSe) from the type locality: New observations and implications for metallogenesis in the Harz Mountains, Germany. *Ore Geology Reviews* **102,** 728–739. ISSN: 01691368. https://doi.org/10.1016/j.oregeorev.2018.09.027 (2018).

28. Kerl, B. Ueber ein neues Vorkommen von Selen- quecksilber. *J. Prakt. Chem.* **57,** 470–476 (1852).

29. Minaev, V. S., Timoshenkov, S. P. & Kalugin, V. V. Structural and Phase Transformations in Condensed Selenium. *Journal of Optoelectronics and Advanced Materials* **7,** 1717–1741. ISSN: 09544119 (2005).

30. Kim, K. S. & Turnbull, D. Crystallization of amorphous selenium films. I. Morphology and kinetics. *Journal of Applied Physics* **44,** 5237–5244. ISSN: 00218979 (1973).

31. Kim, K. S. & Turnbull, D. Crystallization of amorphous selenium films. II. Photo and impurity effects. *J. Appl. Phys.* **45,** 3447–3452. http://ieeexplore.ieee.org/xpls/abs_all.jsp?arnumber=5100908 (1974).

32. Zvára, I. Simulation of Thermochromatographic Processes by the Monte Carlo Method. *Radiochimica Acta* **38,** 95–102. ISSN: 21933405 (1985).

33. Eichler, R. *et al.* Attempts to chemically investigate element 112. *Radiochimica Acta* **94,** 181–191. ISSN: 2193-3405. http://www.degruyter.com/view/j/ract.2006.94.issue-4/ract.2006.94.4.181/ract.2006.94.4.181.xml (2006).

34. Mones, C. & Virginia, W. REMOVAL OF ELEMENTAL MERCURY FROM A GAS STREAM FACILITATED BY A NON-THERMAL PLASMA DEVICE (2006).

35. Wang, Z. H. *et al.* Investigation on elemental mercury oxidation mechanism by non-thermal plasma treatment. *Fuel Processing Technology* **91,** 1395–1400. ISSN: 03783820 (2010).

36. Leimbach, D. *et al.* The electron affinity of astatine. *Nature Communications* **11,** 1–9. ISSN: 20411723. arXiv: 2002.11418 (2020).

37. Eichler, R. & Schädel, M. Adsorption of radon on metal surfaces: A model study for chemical investigations of elements 112 and 114. *Journal of Physical Chemistry B* **106,** 5413–5420. ISSN: 10895647 (2002).

38. Cherin, P. & Unger, P. The Crystal Structuer of Trigonal Selenium. **6,** 1589–1591 (1967).

39. Effect of pressure on the atom positions in Se and Te. *Physical Review B* **16,** 4404–4412. ISSN: 01631829 (1977).

40. Momma, K. *Visualization for Electronic and Structural Analysis* http://www.jp-minerals.org/vesta/en/.

41. Pershina, V., Borschevsky, A., Eliav, E. & Kaldor, U. Prediction of the adsorption behavior of elements 112 and 114 on inert surfaces from ab initio Dirac-Coulomb atomic calculations. *Journal of Chemical Physics* **128.** ISSN: 00219606 (2008).

42. Grosse, R., Swoboda, H. & Tausend, A. Lattice constants a and c of trigonal selenium between 85 and 380K. *Journal of Physics C: Solid State Physics* **8,** 33–35. ISSN: 00223719 (1975).

5 Development of the Trace-gas Reaction Analyzer for Chemistry TRACY

5.1 Introduction

The study of transactinide elements ($Z \geq 104$) marks the frontier of fundamental chemistry with the exciting possibility of discovering and classifying new elements. These exotic Superheavy Elements (SHEs) challenge familiar trends of the periodic table due to the relativistic effects on their electron shells known to scale with the atomic number [1, 2]. Given that the heaviest elements are most affected by relativity, they provide an excellent basis for the study of relativistic effects in atoms. Not yet known to exist in nature, SHEs can only be studied through heavy-ion accelerator based nuclear fusion evaporation reactions at rates as low as one single atom per day - or even weeks[3, 4]. Even then, their half-lives are often in the second to subsecond range. As a result, SHEs are only available for study as single atoms. Given these challenging experimental conditions, the primary method of investigation at present is Gas Chromatography (GC) which provides the required transport speed for short-lived elements as well as sensitivity for single-atom chemistry.

Several SHEs have been successfully characterized using gas chromatographic techniques [5, 6], including some of the heaviest elements studied to date; copernicium ($Z = 112$) and flerovium ($Z = 114$) [7–9]. These elements are also central to this study. Since these SHEs are produced as single atoms over multiple weeks or months, experiments require extremely clean, controlled and stable conditions for their entire duration. The carrier gas employed is usually a mixture of noble gases, argon and helium in this case. From basic molecular kinetic theory, an atom of 200 pm radius[11] at standard temperature and pressure can collide with a 1 ppb impurity such as oxygen ≈ 7 times per second. A reaction with such an impurity could cause unexpected speciation of the SHE and therefore interfere with experimental results. The reaction product could even be non-volatile in a GC, thereby causing a transport loss and consequent low de-

[11] A typical value.

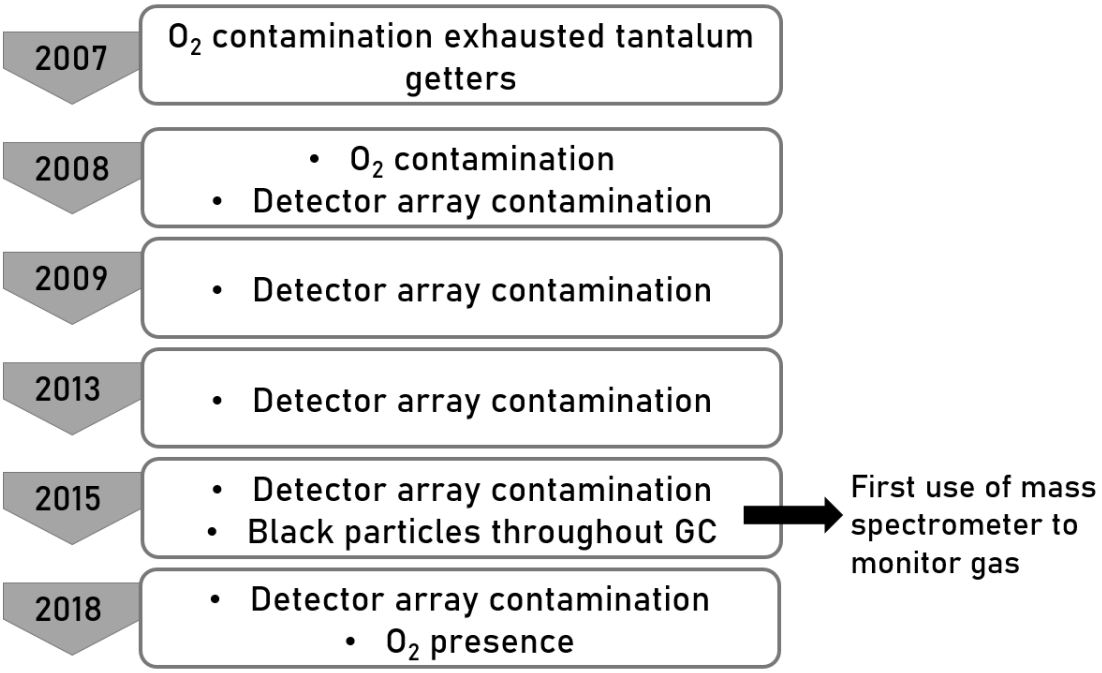

Figure 56: A timeline of copernicium gas chromatography and the observed effects of contaminants as discovered from historical laboratory journals.

tection yield. Both scenarios can be detrimental to experimental campaigns and therefore the ambient conditions of the GC are of fundamental importance to researchers. Contemporary research projects with seaborgium hexacarbonyl have explored trace gas components as the source of yield fluctuations in detail [10]. In early copernicium chemistry research, two successive publications from 2008 and 2009 mentioned detectors losing the ability to retain tracers and the chromatographic deposition pattern broadening as a result [8, 11]. Even though rarely explored in detail, contaminations have interfered with copernicium experiments many times in the past to varying degree (Figure 56).

In the previous chapter,the gradual contamination buildup on Au covered detectors and the factor 3 fluctuation of yield in the $^{182-185}$Hg tracer during the experimental campaign was reported. As a member of group 12, copernicium stands at the risk of forming a non-volatile oxide, which could cause a loss in transport yield. Additionally, it was also shown that the reaction byproduct ^{211}At showed clear evidence of speciation. Astatine is a scarcely studied

member of the halogens owing to its short half-life (longest lived isotope 8.1 hours). Astatine has high potential for use in medicine [12–15], but is also of high interest for fundamental studies of the element [16–19]. As a homolog of tennessine ($Z = 117$), it is also a valuable resource for preliminary SHE study once longer-lived Ts isotopes will become available.

Given the findings in Chapter 5, a dire need for better understanding and controlling the quality of the carrier gas has become evident to ensure reliable experimental results and high SHE yield. With the dawn of next-generation accelerators and separators such as the newly-inaugurated DC-280 cyclotron at the Factory for SHEs in Dubna, Russian Federation [20, 21], chromatographic experimental techniques must maintain a high standard to harness the new potential of increased production rates to the fullest degree. Here, the new Trace-gas Reaction Analyzer for Chemistry (TRACY) setup has been designed and tested preliminarily. TRACY is a gas chromatography loop designed for on-line use with SHE homologs (Hg and At) with the aim to closely monitor ambient experimental conditions with the possibility to functionalize the mobile phase with contaminants to observe speciation effects as well as transport yield fluctuations. TRACY is however a versatile GC loop and could easily be adapted for the study of other volatile species.

5.2 Experimental

5.2.1 The TRACY Gas Chromatographic Loop

The TRACY GC setup was modelled after the tried and tested Cryo On-Line Detector COLD setup used in the first chemical characterization of Cn [7]. The schematics of TRACY are depicted in figure 57. Typically, nuclear fusion Evaporation Residues (ER) are thermalized in an Ar/He mixture (ratio 3:7) as the mobile phase. The pressure in the GC is 1.2 bar to ensure any leaks do not allow atmosphere to ingress. H_2, O_2 and H_2O can be selectively dosed into the mixture to vary the carrier gas contamination affecting the yield and species transported. The ER are transported from the recoil chamber via an in-situ volatilization oven [22] followed by a

Perfluoroalkoxy PFA capillary ($\varnothing_{inner}$ 4 mm) at room temperature to a 2×4 Positive Implanted N-type (PIN) diode-detector array. Thus, ER only come into contact with quartz and PFA surfaces before exposed to the gold-plated detectors. The PIN detectors operate isothermally at room temperature with an almost 100% detection efficiency for spontaneous fission and 86% for α-particles from any nuclides deposited on their surface. The gas composition is monitored in real-time using an atmospheric mass spectrometer (mks Cirrus®2). The gas flows reached in the loop ranged from 800 ml/min to 2.2 l/min.

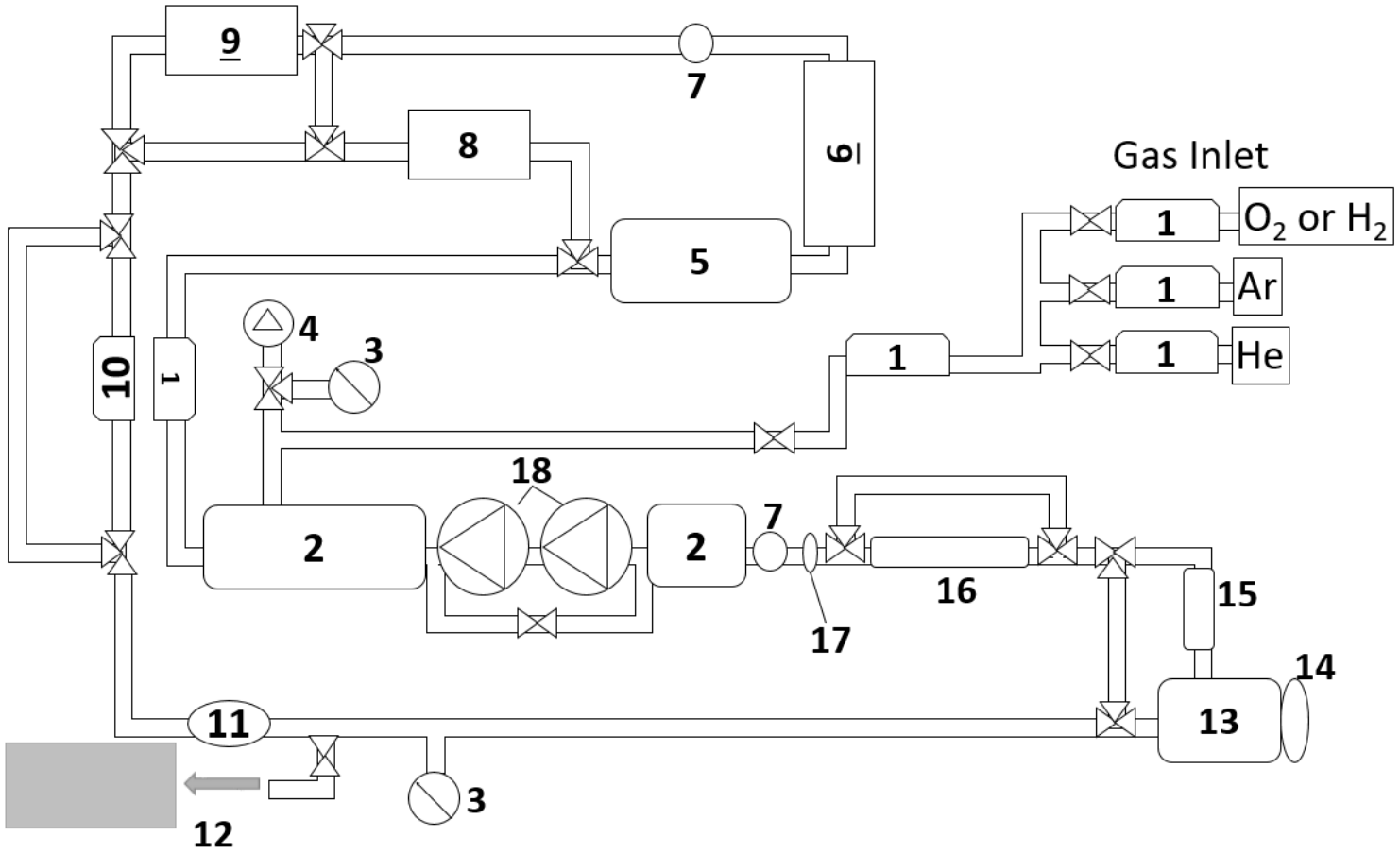

Figure 57: The Trace-gas Reaction Apparatus for Chemistry TRACY. **1** Mass flow controller, **2** Buffer volume, **3** Pressure gage, **4** Vacuum pump, **5** MnO_2 oven, **6** SICAPENT®, **7** 0.5 micron particle filter, **8** Humidifier, **9** Ta getter, **10** SAES MicroTorr 902, **11** Mitchell Easydew Hygrometer, **12** Mass Spectrometer, **13** Recoil chamber, **14** ^{nat}Er/Eu Target, **15** IVO Oven, **16** TRACY detector array, **17** Charcoal Trap, **18** Rotary pump

5.2.2 Mercury and Astatine Radionuclide Production

A research grant has been approved for a future experimental campaign at the JAEA tandem accelerator. The tracer nuclides $^{198-200}$At will be produced in the heavy ion induced nuclear fusion reaction ^{nat}Er(^{35}Cl, xn)$^{198-200}$At, $x = 1 - 5$. Similarly the $^{183-185}$Hg nuclides will be produced via ^{nat}Eu(^{35}Cl, xn)$^{183-185}$Hg, $x = 2-5$. A mixed target was prepared for experiments with both elements present. A 180 MeV ^{35}Cl beam (center of target) will be used. The cross-section was estimated to be in the range of 2 mbarn for $^{198-200}$At and 10-20 mbarn for $^{183-185}$Hg [23] (Figure 58). The decay schemes for the primarily produced isotopes are presented in figure 58. Short- lived isotopes were chosen for production in order to show changes in the experimental conditions such as gas composition in real time, while also simulating short-lived SHEs.

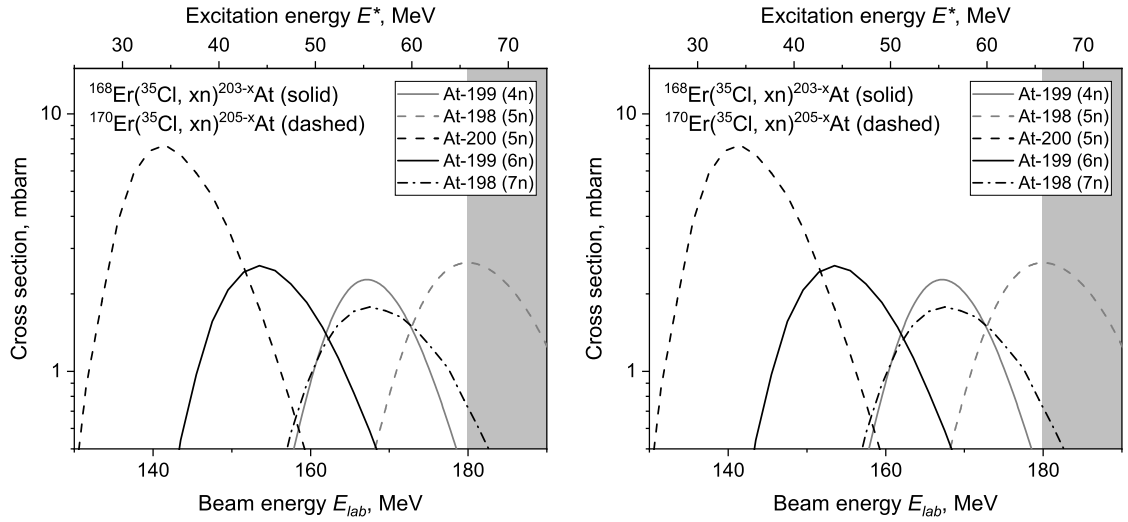

Figure 58: Calculated production cross sections for $^{183-185}$Hg and $^{198-200}$At radionuclides [24]. $^{35}Cl^{10+}$ ion beam energies that can be reached at the JAEA Tandem Accelerator are in the unshaded area.

5.3 Preliminary Off-line Testing

5.3.1 Oxygen Dosing and Hg Yield

The TRACY gas chromatography loop was connected to a quartz tube with an irradiated Au foil as a source for ^{197m}Hg (t_{1_2} = 23.8 h, main γ-ray 33% 133.99 keV, see Chapter 3). An activated charcoal trap was used to capture radioisotopes and determine their transport yield. The activated charcoal trap was heated in a nitrogen gas stream prior to use to ensure any retained water was removed. In the GC, the Au containing quartz tube and charcoal trap effectively simulated the recoil chamber and detector array (Components **13, 15, 16** Figure 57). The TRACY was evacuated ($\leq 10^{-5}$ hPa) and filled with the inert gas mixture doped with a series of known O_2 volumes measured by a mass-flow controller (Brooks Instruments Series 5851E, i). For experimental runs, the Au foil was heated to 1000°C to release the carrier-free ^{197m}Hg to be transported via a 2 m PFA capillary to an activated charcoal trap connected again to the loop, serving as the detector. The charcoal trap was then measured using a high-purity germanium (HPGe) γ-ray detector (Ortec GEM-23185) to quantify the ^{197m}Hg transport yield. The Au foil was measured before and after the experiment to ensure all the ^{197m}Hg had been released. Due to equipment constraints, the γ-ray measurements are relative, as the measurement geometry and conditions changed when measuring the charcoal trap inside a steel casing compared to the Au foil inside a quartz tube. The ^{197m}Hg transport yield was relatively quantified at three O_2 levels; below detection limit ($\approx$ 100 ppb) while operating a Ta getter for trace O_2 removal, at a low addition of 2500 ppm, and finally at gross excess of O_2 with 50% of the gas being oxygen.

5.3.2 Water Dosing

The TRACY gas chromatography loop is fitted with a humidifier based on a Peltier device (Figure 57 component **8**) with a 20 ml water reservoir which can cool to -46°C. When connected to the TRACY, the carrier gas is diverted over the frozen H_2O, which affects the humidity in

the loop. During operation of the humidifier, the SICAPENT® is not included in the loop. The TRACY was operated with a series of temperatures while monitoring the humidity with the hygrometer and mass spectrometer to test the stability and saturation speed of moisture in the system. No measurements specific to hydrogen gas content were done in the TRACY.

5.4 Results and Discussion

5.4.1 Oxygen Contamination Calibration

A series of known volumes of O_2 were dosed into the 6.0 L total volume of the TRACY (Figure 59).

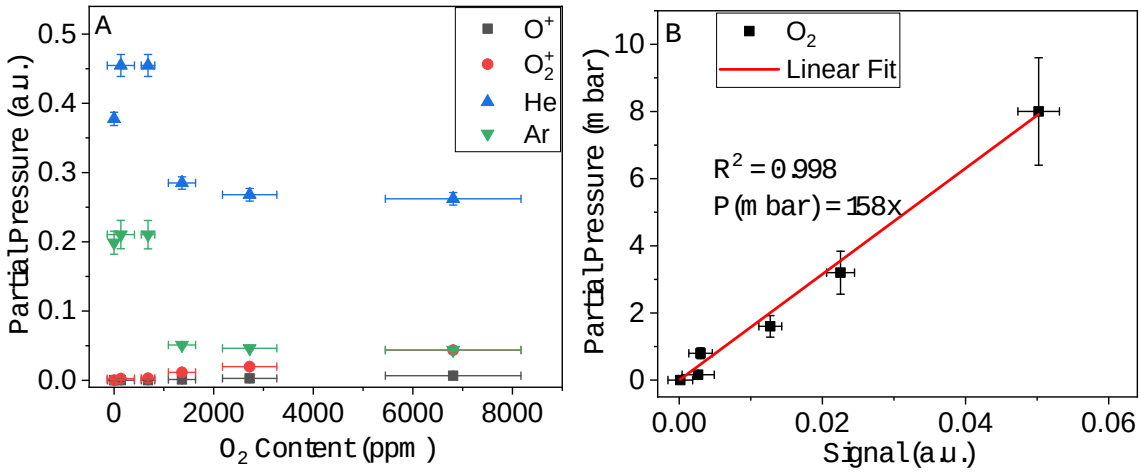

Figure 59: Calibration of the mass spectrometer using the TRACY doped with a series of O_2 admixtures. **A** As O_2 is introduced into the system, strong quenching affects Ar and He, decreasing their apparent signal. **B** Mass spectrometer calibration curve generated from dosing known O_2 quantities into the system.

Even at the lowest oxygen addition of 130 ppm, the mass spectrometer was able to detect the trace gas and the partial pressure followed a linear increase. This allowed us to generate a calibration curve which could be used in on-line experiments to determine the real amount of contamination present in the GC loop. Addition of oxygen also strongly affected the signal for

the noble gases helium and argon. Both signals dropped significantly at higher oxygen contents due to quenching effects. Such quenching effects are a known occurrence and therefore the mass spectrometer should be calibrated before an on-line experiment to give most accurate results.

As an additional preliminary test, the ^{197m}Hg transport yield was measured under three different oxygen levels in the gas loop (Table 9).

Table 9: Amount of O_2 dosed into the 6L carrier gas of TRACY and the respective ^{197m}Hg transport yield from the gold foil to the activated charcoal trap as measured by γ-ray spectrometry.

O_2 Content (ppm)	^{197m}Hg Transport Yield
< 0.1	100%
2720 ± 540	56%
$5 \cdot 10^5 \pm 0.15 \cdot 10^5$	1%

It is apparent that with the addition of oxygen, the transport yield drops significantly to the point where almost all ^{197m}Hg can be lost. The ^{197m}Hg tracer which was not transported to the charcoal trap was found deposited primarily in the quartz tube after the starter oven. This means that the tracer was likely volatilized and in the heat of the oven reacted with oxygen in the carrier gas, forming non-volatile HgO [25, 26]. From the previous chapter it can be estimated that in some experiments in the COLD which had a transport yield loss of factor 3, the oxygen content therefore likely exceeded 3000 ppm.

5.4.2 Water Contamination Calibration

The humidifier function was also tested by varying its water addition to the GC (Figure 60).

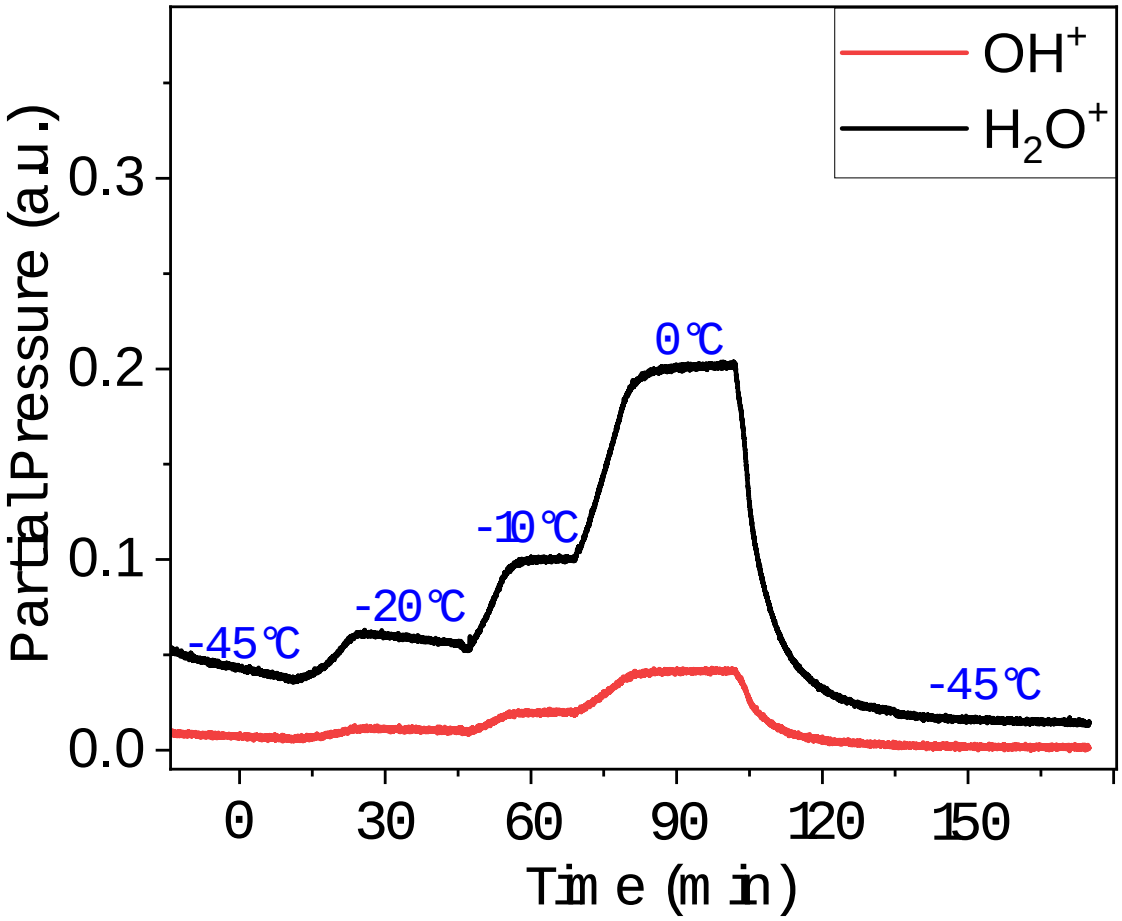

Figure 60: Mass spectrometry measurement of (arbitrary) partial pressure of OH^+ and H_2O^+ ions in the carrier gas while varying the humidifier temperature (Blue numbers). The humidity is shown to repeatedly reach stable levels after 30 minutes. The effect is reversible when decreasing the temperature of the humidifier again. Note that due to the mass spectrometer removing gas from the loop, the total pressure in the system lowers, making the final humidity appear lower than initial.

It was shown that the effect of the humidifier repeatedly reached stable levels after 30 minutes of adjusting the temperature, making it a fast-reacting component. Furthermore, it was shown that the humidity level was reversible by decreasing the humidifier temperature again, thus

likely freezing the H_2O in the carrier gas back into the reservoir. Unlike the addition of oxygen to the carrier gas, no quenching effects were observed on the noble gases He and Ar. In addition to the mass spectrometry measurement, a hygrometer also monitored the dew point of the carrier gas (Table 10).

Table 10: The temperature setting of the humidifier and the corresponding dew point matched to their respective water contents in the carrier gas. ‡ zero value using the drying cartridge to remove moisture from system, no humidifier in loop. [1]Values for H_2O content from [27].

Humidifier Temperature (°C)	Dew Point (± 2°C)	$[H_2O]^1$ (ppm, ± 3%)
N/A‡	-85	0.6
-45	-75	1.0
-20	-71	2.2
-10	-67	4.0
0	-58	9.1
-43	-73	1.6

By using the dew point with corresponding established vapor pressure [27], a calibration curve for both the humidifier and the mass spectrometer was generated (Figure 61).

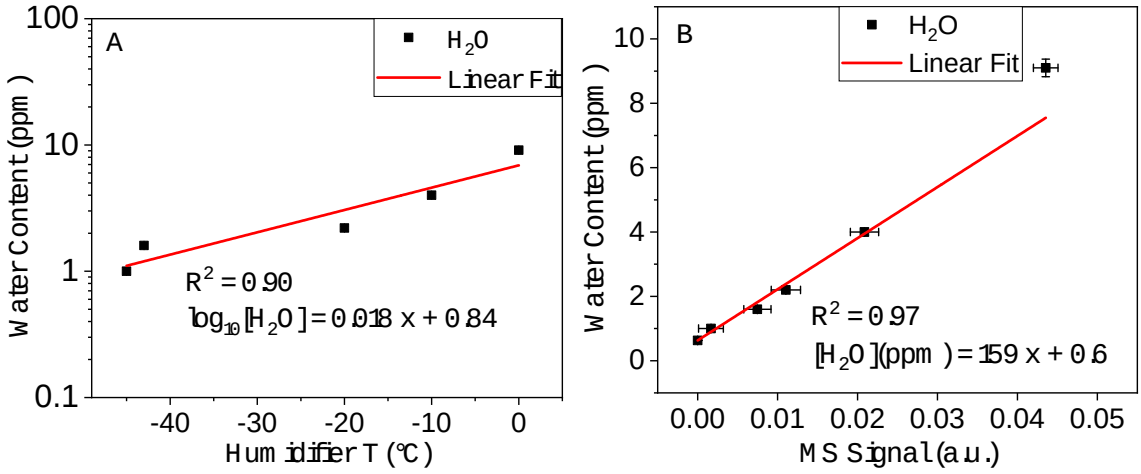

Figure 61: **A** Calibration of the humidifier temperature setting to allow precise dosing of water to the carrier gas. **B**Calibration of the mass spectrometer so carrier gas water levels can be quantified.

Using the established relation in figure 61 **A**, it was shown that the humidifier is be able to dose precise amount of water into the carrier gas depending on the programmed temperature. In addition, the mass spectrometer was calibrated, so that in future experimental campaigns this method can be used to estimate the actual water content in a GC.

We have thus shown that the humidifier is effective in adding moisture to the system while maintaining stable levels, which is a necessity for SHE experiments. The effects can be directly measured in the carrier gas using a dew point sensor, however the temperature does not directly correspond to the Peltier device. This is since the dew point represents the live temperature at which the carrier gas is saturated with water vapour, while the humidifier merely maintains its programmed temperature. No effect of carrier gas water content on the mercury transport yield was yet measured.

5.5 Conclusions

The new TRACY loop was designed to perform and monitor on-line gas chromatographic experiments in real-time for the purpose of identifying sources of contamination, yield loss and speciation in SHE and homolog experiments. Experiments on oxygen as a trace gas contamination revealed that it is possible to use the mass spectrometer for the quantification of O_2 content, however results are not very accurate below $\approx$ 1000 ppm, with an uncertainty of $\approx$ 45%. At these levels, the mass spectrometer functions better as a triage device to test for oxygen presence (0.1 - 1000 ppm) or absence ($<$ 0.1 ppm). It was also shown that the presence of oxygen drastically affects the yield of transported mercury in the carrier gas, which can mean high transport yield losses for SHEs that can a form non-volatile oxide as is likely for copernicium, a group 12 element, despite its proposed increased inertness.

The controlled addition of water to the carrier gas using the humidifier was also analyzed and it was found that it is capable of quickly altering the water content of the carrier gas resulting in stable conditions. The effects are reversible and thus the humidifier can also act as a drying unit for a GC with elevated moisture levels. Both the humidifier and the mass spectrometer were calibrated using our system, so that in upcoming experimental campaigns experiments with controlled ambient environments will be possible given re-calibration. It is worthy of note that in typical experiments using the COLD chromatography loop, dew points below the detection limit of -100°C are typically reached, which was not possible in the present experiment. The reason is likely the cooling of the loop using liquid nitrogen at -160°C, thus freezing any residual water. This commonly occurs on the latter part of the COLD array, covering the detectors in ice, a phenomenon previously observed [8].

No experiments using the addition of hydrogen gas were yet performed. The results of the preliminary testing show that the TRACY is ready to be used in future experimental campaigns with the ability to intentionally dope carrier gases with contaminants so as to explore speciation and transport yield effects on radionuclides produced on-line in nuclear fusion evaporation reactions. By calibrating a mass spectrometer connected to the carrier gas, it is also possible to quantify these side-reactions. The complete setup is significantly more compact compared to the existing COLD loop making international experimental campaigns accessible. It is particularly suited for SHE homolog studies, but could even be modified for the on-line investigation of SHEs. Components in the loop are modular and therefore easily replaceable or interchangeable so that the TRACY can be easily adapted to different gas chromatographic investigations. It was also shown that while it was designed for use with an α-particle and spontaneous fission detector array, this could be simply replaced with a starter oven-activated charcoal trap combination for easy off-line experimentation. Future SHE experiments will no doubt benefit from the revelations of this experiment.

References

1. Pyykko, P. & Desclaux, J. P. Relativity and the Periodic System of Elements. *Accounts of Chemical Research* **12,** 276–281. ISSN: 15204898 (1979).
2. Fricke, B. in *Struct. Bonding* J. D. Duni, 89–144 (Springer, Berlin, 1975).
3. Oganessian, Y. T. *et al.* Synthesis of a New Element with Atomic Number $Z = 117$. *Phys. Rev. Lett.* **104,** 142502. https://link.aps.org/doi/10.1103/PhysRevLett.104.142502 (14 Apr. 2010).
4. Smits, O. R., Mewes, J. M., Jerabek, P. & Schwerdtfeger, P. Oganesson: A Noble Gas Element That Is Neither Noble Nor a Gas. *Angewandte Chemie - International Edition* **59,** 23636–23640. ISSN: 15213773 (2020).
5. Greenwood, N. N. Recent developments concerning the discovery of elements 101-111. *Pure and Applied Chemistry* **69,** 179–184. ISSN: 00334545 (1997).
6. Schädel, M. *Chemistry of superheavy elements* 2nd (eds Schädel, M. & Saughnessy, D.) 2. ISBN: 9783642374654 (Springer, Berlin, Heidelberg, 2014).
7. Eichler, R. *et al.* Chemical characterization of element 112. *Nature* **447,** 72–75. ISSN: 0028-0836. http://www.nature.com/doifinder/10.1038/nature05761 (2007).
8. Eichler, R. *et al.* Thermochemical and physical properties of element 112. *Angewandte Chemie - International Edition* **47,** 3262–3266. ISSN: 14337851 (2008).
9. Eichler, R. First foot prints of chemistry on the shore of the Island of Superheavy Elements. *Journal of Physics: Conference Series* **420,** 012003. ISSN: 1742-6588. http://stacks.iop.org/1742-6596/420/i=1/a=012003?key=crossref.a4877d08c84891076123d03ba7a38c36 (2013).
10. Wittwer, Y. *Optimization of Formation and Transport Yields for Metal Carbonyl Complexes under Single-Atom Chemistry Conditions* PhD thesis (University of Bern, 2020).

11. Wittwer, D. *et al.* Gas phase chemical studies of superheavy elements using the Dubna gas-filled recoil separator - Stopping range determination. *Nuclear Instruments and Methods in Physics Research, Section B: Beam Interactions with Materials and Atoms* **268,** 28–35. ISSN: 0168583X. http://dx.doi.org/10.1016/j.nimb.2009.09.062 (2010).

12. Wilbur, D. S. Enigmatic astatine. *Nature Chemistry* **5,** 246. ISSN: 17554330. http://dx.doi.org/10.1038/nchem.1580 (2013).

13. Robinson, M. K. *et al.* Effective treatment of established human breast tumor xenografts in immunodeficient mice with a single dose of the α-emitting radioisotope astatine-211 conjugated to anti-HER2/neu diabodies. *Clinical Cancer Research* **14,** 875–882. ISSN: 10780432 (2008).

14. Liu, W. *et al.* Astatine-211 labelled a small molecule peptide: Specific cell killing in vitro and targeted therapy in a nude-mouse model. *Radiochimica Acta* **109,** 119–126. ISSN: 00338230 (2021).

15. Wilbur, S. Chemical and Radiochemical Considerations in Radiolabeling with alpha-Emitting Radionuclides. *Current Radiopharmaceuticals* **4,** 214–247 (2011).

16. Serov, A. *et al.* Adsorption interaction of astatine species with quartz and gold surfaces. *Radiochimica Acta* **99,** 593–599. ISSN: 00338230 (2011).

17. Rothe, S. *et al.* Measurement of the first ionization potential of astatine by laser ionization spectroscopy. *Nature Communications* **4,** 1835. ISSN: 2041-1723. http://www.nature.com/doifinder/10.1038/ncomms2819 (2013).

18. Condensed astatine: Monatomic and metallic. *Physical Review Letters* **111,** 1–5. ISSN: 00319007 (2013).

19. Appelman, E. H., Sloth, E. N. & Studier, M. H. Observation of Astatine Compounds by Time-of-Flight Mass Spectrometry. *Inorganic Chemistry* **5,** 766–769. ISSN: 1520510X (1966).

20. Gulbekian, G. G. *et al.* Start-Up of the DC-280 Cyclotron, the Basic Facility of the Factory of Superheavy Elements of the Laboratory of Nuclear Reactions at the Joint Institute for Nuclear Research. *Physics of Particles and Nuclei Letters* **16,** 866–875. ISSN: 15318567 (2019).

21. Popeko, A. G. On-line separators for the Dubna Superheavy Element Factory. *Nuclear Instruments and Methods in Physics Research, Section B: Beam Interactions with Materials and Atoms* **376,** 144–149. ISSN: 0168583X. http://dx.doi.org/10.1016/j.nimb.2016.02.025 (2016).

22. Düllmann, C. E. *et al.* Chemical investigation of hassium (element 108). *Nature* **418,** 859–862. ISSN: 00280836 (2002).

23. Karpov, A. V., Rachkov, V. A. & Saiko, V. V. Formation of Neutron-Enriched Heavy and Superheavy Nuclei in Fusion Reactions. **15,** 247–256 (2018).

24. Karpov, A. V., Denikin, A. S. & Naumenko, M. A. No Title. *Nucl. Instrum. Methods Phys. Res.* **859,** 112–124. http://nrv.jinr.ru/nrv/ (2017).

25. Mones, C. & Virginia, W. REMOVAL OF ELEMENTAL MERCURY FROM A GAS STREAM FACILITATED BY A NON-THERMAL PLASMA DEVICE (2006).

26. Wang, Z. H. *et al.* Investigation on elemental mercury oxidation mechanism by non-thermal plasma treatment. *Fuel Processing Technology* **91,** 1395–1400. ISSN: 03783820 (2010).

27. Wagner, W., Riethmann, T., Feistel, R. & Harvey, A. H. New Equations for the Sublimation Pressure and Melting Pressure of H2O Ice Ih. *Journal of Physical and Chemical Reference Data* **40.** ISSN: 00472689 (2011).

6 Conclusions and Outlook

This work developed new chromatographic selenium surfaces for the use in α- and spontaneous fission spectrometry. Much emphasis was given to the long-term stability and homogeneity of the chromatographic surfaces. The allotropy of selenium revealed as a complex behaviour, and controlling the crystallization could potentially minimize reactive sites in the fully converted trigonal selenium allotrope. The outlined methods provide optimized chromatographic surfaces for the demanding experimental conditions during superheavy element investigations. Future experimental campaigns will therefore have a more reliable component. These selenium chromatographic surfaces could however be adapted for use in a broader field. Due to the inherent Se stability and insolubility, it would even be suitable for use in liquid chromatographic investigations, should longer-lived isotopes of superheavy elements become more available. The knowledge gained here could also be used as a foundation for the next chalcogen in the series, tellurium. With increased metallic character, but still a member of the chalcogens it could provide new insights into the comparative chemistry of Hg, Cn and Rn.

Unfortunately, no Fl (Z = 114) atoms have been observed in a Se experiment to date. As Cn is indirectly synthesized via Fl, there is high potential for exploring its chemistry in parallel given the opportunity. As a member of group 14, Fl is a likely candidate for chemical reactions with chalcogens, as is commonly observed in its lighter homolog which readily forms PbO, PbS, PbSe and PbTe. The development of the stable *t*-Se detectors however will ensure that future experimental campaigns will not encounter uncertainty due to an unstable chromatographic surface.

The new inverse thermochromatography experimental method is extremely promising, with enormous potential for use in many fundamental chemical reactions. It provides a basis of understanding previously unexplained behaviour, where tracers in chromatographies have an affinity for a chromatographic surface at relatively high and low temperatures, with little interaction in between. The inverse thermochromatography provides an explanation for this behaviour, with tracer deposition at high temperatures due to reaction with the chromatographic

surface, and at low temperatures due to adsorption to the surface. Furthermore, it allows for the determination of reaction kinetics in a novel way. It was possible to extrapolate for the first time an estimated activation energy for the CnSe formation. Additionally, from the limited data available, it became apparent that the extrapolation was an overestimation. Such reaction kinetics are crucial fundamental findings that can support or contradict standing theories on superheavy elements. It was shown here that while Cn has long been seen as exceptionally inert, it can also exhibit reactive behaviour. The inverse thermochromatographic methods developed here will also be useful in the future, determining the reaction kinetics of Fl.

With the newly operational Superheavy Element Factory in Dubna, Russian Federation, much higher detection rates of transactinides are to be expected. One of the most serious challenges encountered during superheavy element research was undoubtedly maintaining stable, clean gas chromatography conditions for multiple weeks. To truly exploit the new high superheavy element production rates, the possibility of transport losses and speciation due to contaminants in the carrier gas must be minimized. The design and development of the Trace-gas Reaction Analyzer for Chemistry (TRACY) is a first step toward the quantification of such effects, with high adaptability to many similar types of experiments. The successful proof of concept of the TRACY has already been approved for an on-line chemical investigation of the chemistry of astatine in the collaboration with the Japanese Atomic Energy Agency at Tokai, Japan. One further possible use of the TRACY is the future introduction of *protective* gases into the carrier gas; It was observed that oxygen has a negative effect on the Hg transport, but hydrogen gas does not react with Hg. Therefore, deliberate addition of trace hydrogen may in fact remove excess oxygen from the gas by forming water, while not interfering with the tracers of interest.

7 Appendix A - Monte-Carlo Simulation Code

```
%Paul's adaptation for COLD square channels of a Monte-
Carlo simulation
%Activation Energy Determination
%intended for Hg
%22.02.2021
clear all
clc

A = 10000;                % total number of atoms
R = 8.31447;              % {gas const J/molK}
pSiO2 = 4.5067E12;        % phonon oscillation frequency s-1
pSe = 4.8546E12;          % Lindeman's eq. osc. Freq. s-1
pAu = 4.2E12;             %phonon oscillation Au s-1
pIce = 4.04192E12;        % Lindeman's Eq

%%%%%%%%%%%%%%%%%% GAS MIXTURE %%%%%%%%%%%%%%%%%%%%%%%%%%%%
Mg1 = 4.002602; % molecular weight carrier gas - He (g/mol)
Mg2 = 39.984;   %molecular weight Ar (g/mol)
dg1 = 0.145;    % density carrier gas at melting point He
(g/cm3)
dg2 = 1.42;     % Carrier gas density Ar
dg = 1*dg1+0*dg2;   % Carrier gas density mixture
Mg = 1*Mg1+0*Mg2;   % Carrier gas molar mass g/mol mixture
%%%%%%%%%%%%%%%%%%%%%%%%%%%%%%%%%%%%%%%%%%%%%%%%%%%%%%%%%%%

%%%%%%%%%%%%%%%%%% Copernicium Adsorption %%%%%%%%%%%%%%%%
% dHa2 = -62000;          % Adsorption with t-Se, J/mol
% dHa3 = -40000;          % Adsorption with quartz, J/mol
% dHa4 = -52000;                    % Cn on Au, J/mol
% dHa5 = -25000;                  %Cn on ice (guess)
% Mv = 283;           % Molar mass of Tracer, Cn g/mol
% dv = 11;            % Density of solid Tracer Cn g/cm3
% Thl = 3.8;          % half-life of the nuclide, s
%%%%%%%%%%%%%%%%%%%%%%%%%%%%%%%%%%%%%%%%%%%%%%%%%%%%%%%%%%%

%%%%%%%%%%%%%%%% Mercury Adsorption %%%%%%%%%%%%%%%%%%%%%%
dHa1 = -85000;        % Ads. with a-Se, J/mol
dHa2 = -60000;        % Ads. with t-Se, J/mol
dHa3 = -40000;        % Ads. with quartz, J/mol
dHa4 = -98000;        % Ads. Hg on Au, J/mol
Mv = 197;             % Molar mass of Tracer, g/mol
dv = 13.594;          % Density of solid Tracer g/cm3
Thl = 64*60*60;       % half-life of the nuclide, s
%%%%%%%%%%%%%%%%%%%%%%%%%%%%%%%%%%%%%%%%%%%%%%%%%%%%%%%%%%%
```

```
%%%%%%%%%%%%%%%  SELENIUM SURFACE %%%%%%%%%%%%%%%%%%%%%%%%
aSe = 0;                % a-Se coverage, min 0 max 1
tSe = 1;                % coverage of t-Se, min 0 max 1
SiO2 = 1 - (aSe + tSe); % uncovered portion
%%%%%%%%%%%%%%%%%%%%%%%%%%%%%%%%%%%%%%%%%%%%%%%%%%%%%%%%%%%

%%%%%%%%%%%%%%%  Constants  %%%%%%%%%%%%%%%%%%%%%%%%
p  = 1*101325;     % Pressure in the column Pa
l = 0.204;         % length of the column, (m)
a1 = 2e-3;         % height of channel (m)
b1 = 8.3e-3;       % width of channel (m)
Q = 50/60000000;   % gas flow m3/s
trun = 1*60*60;    % experiment duration, s
vv = Mv/dv;        % Molar Volume for tracer (Hg)
vg = Mg/dg;        % Molar colume for carrier (He)
kb = 1.38e-23;      %Boltzmann constant m^2kg/s^2K
hp = 6.63e-34;      %Planck's Constant m^2kg/s

column = [1:240];
col_array = [];     %generate matrix for storing results

%%%%%%%%%%%%%%%%%%%%%%%%%%%%%%%%%%%%%%%%%%%%%%%%%%%%%%%%%%%

k1 = 0;  %Eyring Trans. Coeff. 0.9-1 OR Arrhenius pre-
exponential factor A

%%%%%%%%%%%%%%%%%%%%%%%%%%%%%%%%%%%%%%%%%%%%%%%%%%%%%%%%%%%
%experimental Values for TCs. Note Detectors are 12mm wide,
the results are binned to the 12mm in the simulation.
Experiments had a Quartz detector at position 1 which is
ignored here. Comment in/out the desired experiment

%Isothermal
% IT1 = [1.502 1.502 0.721 0.721 1.335 1.335 0.8011 0.8011
3.004 3.004... %collength 228
%    2.056 2.056 2.443 2.443 2.563 2.563 3.451 3.451 1.694
0 0 62.65];
%  IT2 = [7.61 7.61 4.214 4.214 3.7 3.7 3.863 3.863 4.065
4.065...
%      2.605 2.605 3.777 3.777 0 0 0 0 0 12.88];
% ltemp = 25*ones(1,260);
```

```
%TC5 note that Se evaporated after detector 8 (= 12mm x 8
det)
% TC5 = [86.49 0.9046 0.5292 0.5215 0.1089 0.0531 0.0531
0.02947 0.2947 0.0102...
%     0.0102 0.04485 0.04485 0.00769 0.00769 0.0545 0.0454
0 0 11.44];
% TC-05 Temperature °C
% ltemp = [148:0.385:225];
% ltemp = [ltemp 225*ones(1,19)];

TC6 = [9.208 17.08 18.69 15.21 10.93 6.524 5.683 3.391
3.007 2.752...
    1.606 1.293 0.8178 0.1907 0.1011 0.1057 0.03676 0 0
3.372];
% % %TC-06 Temperature °C
ltemp = [71.82:0.485:163];
ltemp = [ltemp 163*ones(1,19)];

% TC7 = [ 0.6812 0.2428 0.4384 0.1957 0.5 0.5508 0.2536
0.7927 0.5798 1.725...
%     2.504 6.747 2.272 1.384 2.877 3.544 2.33 0 0 72.38];
% ltemp = [39.84:0.5358:147];
% ltemp = [ltemp 147*ones(1,19)];

% IT1 = IT1'; %l for this is 228
% %  IT2 = IT2';
% TC5 = TC5';
TC6 = TC6'; %these are experimental values
% TC7 = TC7';   %l for these is 204
%%%%%%%%%%%%%%%%%%%%%%%%%%%%%%%%%%%%%%%%%%%%%%%%%%%%%%%%%%%

ltemp=ltemp+273;    %convert °C to Kelvin
G1 = Q * max(ltemp)/298.15*101325/p;

%%%%%%%%%%%%%% start MC for each atom %%%%%%%%%%%%%%%%
for o = 1:11
    k1 = k1 + 1e13; %Iterate Trans. Coeff. / A
    Ea = 170e3;   % dG for Eyring, Ea for Arrhenius J/mol

for j = 1:40
    tic
Ea = Ea + 1e3;  %Iterate Ea by increment
nuc_detected = zeros(1,240);
for atom=1:A
```

```
%     Initiate initial particle parameters for each atom
    t_exp = 0.0;
    y_pos = 0.0;
    lt = ( -Thl / log(2)) * log(1 - rand(1));

%     keep running as long as particle hasn't decayed or
left column
    while y_pos <= l && t_exp <= lt && t_exp <= trun

%         this assigns the local temperature
        i = fix(y_pos * 1000);
        if i>0
              Temp_Adjust = ltemp(i) + ((ltemp(i + 1) -
ltemp(i)) * ((y_pos * 1000) - i));
        end
        if i==0
                  Temp_Adjust = ltemp(i+1) + ((ltemp(i +
2) - ltemp(i+1)) * ((y_pos * 1000) - i));
        end


D298=0.0043*(298.15*sqrt(298.15))*sqrt(1/(Mg)+1/(Mv))/((((v
g^(1/3))+(vv^(1/3)))^2)/(p/101325));
    D=D298*exp(1.5*log(Temp_Adjust/298.15))/10000;

%     gas flow adjustment accorting to temperature
     G2 = Q * Temp_Adjust/298.15*101325/p;
     G=(G1+G2)/2;
     Ui = G1/(a1*b1);    %Gas velocity m/s

%%%%%%%%%%%%%%%%%%%%%%%%%%%%%%%%%%%%%%%%%%%%%%%%%%%%%%%%%%%%
% Surface Assignment for dHa if needed
%%%%%%%%%%%%%%%%%%%%%%%%%%%%%%%%%%%%%%%%%%%%%%%%%%%%%%%%%%%%
%      if y_pos <= l %& y_pos > 12
% % %       dH for randomised surface, red or grey Se
%         surface = rand(1);
%          if surface <= aSe
%           dHa = dHa1;
%           lpf = pSe;
%          end
%          if surface > aSe && surface <= (1 - SiO2)
%            dHa = dHa2;
%             lpf = pSe;
```

```
%           end
%           if surface > (1 - SiO2)
%              dHa = dHa3;
%               lpf = pSiO2;
%           end
%       end
dHa = dHa2;
lpf = pSe;
%%%%%%%%%%%%%%%%%%%%%%%%%%%%%%%%%%%%%%%%%%%%%%%%%%%%%%%%%%%%%%%%%%%%%%%%

%%%%%%%%%%%%%%%%%%%%%%%%%%%%%%%%%%%%%%%%%%%%%%%%%%%%%%%%%%%%%%%%%%%%%%%%
     %JUMP
%%%%%%%%%%%%%%%%%%%%%%%%%%%%%%%%%%%%%%%%%%%%%%%%%%%%%%%%%%%%%%%%%%%%%%%%
    tm = 1/lpf * exp(-dHa/(R*Temp_Adjust))%time adsorbed s
    vi = ((a1+b1)/G1) * sqrt(2 * R * Temp_Adjust /(pi*
Mv/1000));%Collision number 1/m
     Ri = (1/Ui)/((1/Ui)+(vi*tm));

%     Poppe's paper, adjusted for copper column one-sided
     Nm1 =
2*D*a1*b1/G1+(5.36+17.74*Ri+82.4*Ri*Ri)*G1*a1/(105*(1+Ri)*(
1+Ri)*D*b1); %Nm = avg jump distance for one-sided channel
(m)
     Ni = -Nm1 * (log(1-rand(1)));  %Ni = actual jump
distance, rectangular column, (m)
     y_pos = y_pos + Ni; %add jump to current distance
travelled (m)
     fz = Ni / Ui;          %flight time when not adsorbed
     t_exp = t_exp + fz;    %time elapsed for atom


     if y_pos >= l       % Testing Time and Space
        nuc_detected(240) = nuc_detected(240) + 1; %add to
exit of channel
     end

     if y_pos <= l & y_pos > 0  %if run ends before atom
decayed
        if (t_exp > trun)
            xya = fix(y_pos * 1000);
            nuc_detected(xya+1) = nuc_detected(xya+1) + 1;
        end
%%%%%%%%%%%%%%%%%%%%%%%%%%%%%%%%%%%%%%%%%%%%%%%%%%%%%%%%%%%%%%%%%%%%%%%%
```

```
%%%%%%%%%%%%%%%%%%%%%%%%%%%%%%%%%%%%%%%%%%%%%%%%%%%%%%%%%%%%%%%%%%%%%%%
%        ADSORPTION
%%%%%%%%%%%%%%%%%%%%%%%%%%%%%%%%%%%%%%%%%%%%%%%%%%%%%%%%%%%%%%%%%%%%%%%
            if ((t_exp <= lt) & (t_exp <= trun))


                G1 = Q * Temp_Adjust/298.15*101325/p;
% { Q according to local temperature m3/s}
                tm = 1/lpf * exp(-dHa/(R*Temp_Adjust));
%{avg. sitting time s}
                vi = ((a1+b1)/G1) * sqrt(2 * R *
Temp_Adjust /(pi* Mv/1000));%collision no. 1/m
                Na = (vi * Nm1)* -log(1-rand(1));
%                 ta = Na * tm  * -log(1-rand(1));  %{Time
adsorbed, only relevant if not using arrhenius/eyring
%                 t_exp = t_exp+ta;
%%%%%%%%%%%%%%%%%%%%%%%%%%%%%%%%%%%%%%%%%%%%%%%%%%%%%%%%%%%%%%%%%%%%%%%

%%%%%%%%%%%%%%%%%%%%%%%%%%%%%%%%%%%%%%%%%%%%%%%%%%%%%%%%%%%%%%%%%%%%%%%
%%%  ARRHENIUS / Eyring portion
%%%%%%%%%%%%%%%%%%%%%%%%%%%%%%%%%%%%%%%%%%%%%%%%%%%%%%%%%%%%%%%%%%%%%%%
k_react = kb * Temp_Adjust / hp;
           k2 = k_react * k1 * exp(-Ea/(R*Temp_Adjust));
%Eyring Equation
%          k2 = k1 * exp(-Ea/(R*Temp_Adjust)); %Arrhenius -
note that as this is unimolecular, the rate is limited to
%     collision frequency between molecules, around 10^13
       t_reac = 1/k2; %time for transition state to react

            for q = 1:fix(Na)
                t_f = t_reac * -log(1-rand(1));
                ta = tm  * -log(1-rand(1));
                if t_f >= ta
                     t_exp = t_exp + ta; %doesn't react
                else
                    t_exp = trun + 1; % reacts
                    break
                end
            end
%%%%%%%%%%%%%%%%%%%%%%%%%%%%%%%%%%%%%%%%%%%%%%%%%%%%%%%%%%%%%%%%%%%%%%%

% % %                  test for decay
                if ((t_exp > lt) | (t_exp > trun))
```

```
                    xya = fix(y_pos * 1000);
                    nuc_detected(xya + 1) =
nuc_detected(xya + 1) + 1;
                end
            end
        end
    end

end
%
% test = [test nuc_detected'];
nuc_detected = sum(reshape(nuc_detected,12,20));    %add up
to the 12mm detector size
norm = nuc_detected/A*100;  %normalise results
Ea_var(:,j) = norm';
toc
end

    col_array = [col_array Ea_var];

end

%%%%%%%%%%%%%%%%%%%%%%%%%%%%%%%%%%%%%%%%%%%%%%%%%%%%%%%%%%%%%%%%%%%%%%%
% COMPARE TO EXPERIMENTAL RESULTS and CHI TEST
%%%%%%%%%%%%%%%%%%%%%%%%%%%%%%%%%%%%%%%%%%%%%%%%%%%%%%%%%%%%%%%%%%%%%%%
chi = (col_array - TC6);
ch2 = chi.^2;
ch3 = ch2./TC6;
ch3(isnan(ch3)) = 0;
ch3(isinf(ch3)) = 0;
chi2 = sum(ch3);
chi2 = reshape(chi2, [40, 11]); %Ea, k
%%%%%%%%%%%%%%%%%%%%%%%%%%%%%%%%%%%%%%%%%%%%%%%%%%%%%%%%%%%%%%%%%%%%%%%
sound(sin(1:3000)); % Beep to tell you it's done
h = heatmap(chi2); % Heatmap of results
```

8 Acknowledgements

To my mother, who always supported me to the fullest extent, and to my father, who ignited the spark of curiosity and science in me, I thank you both from the bottom of my heart.

Prof. Andreas Türler, I thank you for accepting me as your PhD student and supporting me along the way. Although our time war rather brief, we had a good working relationship and a common appreciation for whiskey and cigars.

A special thanks to my co-supervisor and our laboratory head Dr. Robert Eichler, who was a mentor with vast patience and insight into all aspects of life, not only chemistry. You always welcomed an opportunity to take us students to the laboratory for a hands-on lesson. Always the first to enter, and the last to leave the lab like a captain on his ship. I'm still sorry about that contamination. Our near-daily coffee breaks were priceless.

Thank you Dominik, for always finding a creative but practical solution to all technical needs in all fields, no matter how unrelated to each other they were. You never let us get away with vague instructions or requests, which in turn taught me much about hands-on work.

A heartwarming thanks to the superheavy elements group as a whole, both old, inactive, active and new. Rugard, Alex Heinz, Nadine, Yves, Benjamin, Patrick, Georg, and Jennifer. You are a hardy group of scientist with broad knowledge and extreme dedication. It was challenging but fulfilling working with you on international experimental campaigns staffing an experiment around the clock. Exploring the entirety of Dubna's restaurants together was a culinary treat. It was also a privilege to build such an experimental setup with your help, despite never being able to see it in action due to the limitations imposed on us by the politics of the COVID-19 situation. Alex, your work in irradiating and managing samples has been immeasurably helpful.

Thank you also to the extended Lab for Radiochemistry group, Erik, Mario, Ivan, Ivan, Ivan, Paul, Ionut, Emilio, Jörg, Doro, Nick, Pascal, Angela and all those who came and went.

Erik, you were a wonderful friend and helpful colleague. The number of bugs in my simulation would approximate to half or double if it weren't for you. Mario, you are a wonderful co-worker and always wanting to help, it was a pleasure. Thank you Nick for those precious irradiations of gold, and thank you Pascal for managing them.

A general thanks to all those who supported me in this work even in small parts, from simple measurements to advice. Science is a collaborative effort and only such can strides of progress be made. I was lucky to have been part of such a collaborative environment at the Paul Scherrer Institute, and of the University of Bern.

E r k l ä r u ng

gemäss Art. 18 PromR Phil.-nat. 2019

Name/Vorname:

Matrikelnummer:

Studiengang:

Bachelor ☐ Master ☐ Dissertation ☐

Titel der Arbeit:

LeiterIn der Arbeit:

Ich erkläre hiermit, dass ich diese Arbeit selbständig verfasst und keine anderen als die angegebenen Quel-len benutzt habe. Alle Stellen, die wörtlich oder sinn-gemäss aus Quellen entnommen wurden, habe ich als solche gekennzeichnet. Mir ist bekannt, dass andern-falls der Senat gemäss Artikel 36 Absatz 1 Buchstabe r des Gesetzes über die Universität vom 5. September 1996 und Artikel 69 des Universitätssta-tuts vom 7. Juni 2011 zum Entzug des Doktortitels be-rechtigt ist.
Für die Zwecke der Begutachtung und der Überprüfung der Einhaltung der Selbständigkeitserklärung bzw. der Reglemente betreffend Plagiate erteile ich der Univer-sität Bern das Recht, die dazu erforderlichen Perso-nendaten zu bearbeiten und Nutzungshandlungen vor-zunehmen, insbesondere die Doktorarbeit zu vervielfäl-tigen und dauerhaft in einer Datenbank zu speichern sowie diese zur Überprüfung von Arbeiten Dritter zu verwenden oder hierzu zur Verfügung zu stellen.

Ort/Datum

Unterschrift